



**HAL**  
open science

# Synthetic Aperture Radar Multi-Polarization Ocean Characteristics and Ship Detection

Bo Wang

► **To cite this version:**

Bo Wang. Synthetic Aperture Radar Multi-Polarization Ocean Characteristics and Ship Detection. Signal and Image processing. Télécom Bretagne, Université de Bretagne Occidentale, 2013. English. NNT: . tel-00979001

**HAL Id: tel-00979001**

**<https://theses.hal.science/tel-00979001>**

Submitted on 15 Apr 2014

**HAL** is a multi-disciplinary open access archive for the deposit and dissemination of scientific research documents, whether they are published or not. The documents may come from teaching and research institutions in France or abroad, or from public or private research centers.

L'archive ouverte pluridisciplinaire **HAL**, est destinée au dépôt et à la diffusion de documents scientifiques de niveau recherche, publiés ou non, émanant des établissements d'enseignement et de recherche français ou étrangers, des laboratoires publics ou privés.

Sous le sceau de l'Université européenne de Bretagne

## **Télécom Bretagne**

En habilitation conjointe avec l'Université de Bretagne Occidentale

Ecole Doctorale – sicma

---

**Radar à Synthèse d'Ouverture Polarimétrique pour la  
Caractérisation de la Surface de la Mer et la Détection de Navire**

**Synthetic Aperture Radar Multi-Polarization Ocean Surface  
Characteristics and Ship Detection**

---

### **Thèse de Doctorat**

Mention : Sciences et Technologies de l'Information et de la Communication (STIC)

Présentée par Bo WANG

Département : ITI

Laboratoire : Lab-STICC

Directeur de thèse : René GARELLO

Soutenue le 9 Décembre 2013

#### **Jury :**

- M. Jean-Claude Souyris chercheur à CNES (Rapporteur)
- M. Hugh Griffiths professeur à l'University College London (Rapporteur)
- M. René Garello professeur à Télécom Bretagne (Directeur de thèse)
- M. Bertrand Chapron chercheur à L.O.S. IFREMER Brest (Encadrant)
- M. Eric Pottier professeur à l'Université Rennes 1 (Examineur)
- M. Fabrice Collard chercheur à OceanDatalab (Examineur)
- M. Grégoire Mercier professeur à Télécom Bretagne (Invité)
- M. Nicolas Longépé ingénieur de recherche à CLS-Division radar Brest (Invité)

---

# Acknowledgement

I owe my gratitude to all those people who have made this dissertation possible and because of whom my doctorate experience has been one that I will cherish forever.

My deepest gratitude is to my advisor, Prof. René Garello. I have been amazingly fortunate to have an advisor who gave me the freedom to explore on my own, and at the same time the guidance to recover when my steps faltered. His patience and support helped me overcome many crisis situations and finish this dissertation.

My co-advisor, Dr. Bertrand Chapron, taught me how to question thoughts and express ideas. I am deeply grateful to him for the long discussions that corrected my understanding towards the ocean surface waves, helped me sort out the technical details of my work. I hope that one day I would become as good an advisor to my students as René and Bertrand has been to me.

Prof. Grégoire Mercier always give me practical advice. I am thankful to him for commenting on my views and helping me understand and enrich my ideas.

I am grateful to Dr. Fabrice Collard and Dr. Alex Mouche, who helped me during the wind and wave programming.

I am also indebted to the members of the group and the department ITI. Particularly, I would like to acknowledge Mme Corinne Le Lann, for her various forms of support during my stay in department ITI. I am also thankful to Prof. Le Caillec Jean-Marc and M. Gwenaël Brunet who maintained all the machines in the department so efficiently that I never had to worry about simulating satellite data and installing software.

Many friends have helped me stay sane through these years in Telecom Bretagne. Their support and care helped me overcome setbacks and stay focused on my study. I greatly value their friendship and I deeply appreciate their belief in me.

Most importantly, none of this would have been possible without the love and patience of my family. My family to whom this dissertation is dedicated to, has been a constant source of love, concern, support and strength all these years. I would like to express my heart-felt gratitude to my parents, my husband, and my extended family.

Finally, I appreciate the financial support from CSC scholarship and MODENA project that funded parts of the research discussed in this dissertation. The last but not the least, RADARSAT-2 SAR data were acquired within the framework of the VIGISAT project.

---

# Abstract

In our study, sea surface characteristics imaged by multi-polarization space-borne synthetic aperture radar (SAR) have been investigated. For the first time, a decomposition of different scattering mechanisms have been performed for ocean satellite SAR imagery to better understand the non-Bragg (Scalar) contribution to the total radar cross section (RCS) and Doppler measurements. Characteristics retrieval and target classification has been established, using polarimetry and Bayesian detection theories. There are generally three types of surface scattering mechanisms occurring when the sea surface is detected by microwave radar, i.e., Bragg, specular, and Rayleigh. Depolarized Bragg contribution corresponds to sea surface capillary wave, while the other two Scalar contributions correspond respectively to the crest of the longer wave before it breaks and foams formed by wave breaking. Different scattering mechanisms induce different polarimetric scattering coefficients and Doppler spectrum. It had been impossible to separate those scattering mechanisms with single polarization radar imageries. On pixel scale, we decomposed radar scattering matrices physically into Bragg and Scalar contributions. The decomposition is an iteration initiated with the radar incidence angle, and controlled by a local incidence angle which is function of co-polarization and cross-polarization. Based on these developments and testing, a strategy has been refined to analyze the signature of different features, to retrieve wind seas and sea swell parameters, as well as slick areas, ships, oil rigs, such polarized targets that may be buried in the Scalar contribution. With polarimetric scattering matrices estimated both for Bragg and Scalar contributions, a sea clutter model describing almost the real sea surface has been improved statistically. From this point, this improved model could be combined with Bayesian detectors to classify man-made metallic targets, such as ships, oil rigs, etc.

**Keywords:** multi-polarization, Scattering matrix, Sea surface scattering, target detection



---

# Résumé

Ce travail de thèse a été consacré à la caractérisation de la surface de la mer par radar à synthèse d'ouverture (RSO) polarimétrique porté par un satellite. Une décomposition en différents mécanismes de diffusion est mise en oeuvre dans un premier temps, pour une meilleure compréhension de la contribution non-Bragg (Scalaire) sur toutes les surface équivalente radar (SER) et les mesures Doppler par images RSO sur la mer. La restitution des caractérisations et la classification des cibles sont définis par polarimétrie et théorie de la détection. Généralement, il y a trois types des mécanismes de diffusion sur la surface quand la mer a été illuminé par une radar micro-onde, i.e., Bragg, spéculaire, et Rayleigh. La contribution de Bragg dépolarisée correspond à des petites vagues de capillarité-gravité, alors que les autres, contributions scalaires correspondent à la réflexion spéculaire par la crête des vagues qui est instable et déferle et la diffusion de Rayleigh sur la mousse après la vague déferlante. Différents mécanismes de diffusion impliquent des coefficients de diffusion polarimétrique différents et des spectre Doppler différents. On ne peut pas séparer les mécanismes de diffusion avec les images radars en polarisation unique. Dans chaque pixel, la matrice de diffusion est décomposée physiquement en contributions Bragg et Scalaire. Cette décomposition est une itération qui est initiée avec l'angle d'incidence, et est contrôlée par l'angle d'incidence local. Ce dernier est fonction du copolarisée et orthopolarisée. Une stratégie, basée sur ces développements et sur ces tests, a été mise en place pour l'analyse de la signature des cibles, la restitution des vent-vagues et la houle, et également les pollutions pétrolières, les navires, ou les plate-formes pétrolière, car les cibles polarisée présentes dans la contribution scalaire seulement. Les estimateurs des matrices de diffusion Bragg et Scalaire bénéficient à un modèle statistique du fouillis de mer. Enfin, l'amélioration du modèle statistique avec la théorie de la détection est proposée au regard la classification pour des cibles artificielles, comme les navires ou les plate-formes pétrolières.

**Modèles-clés: Polarimétrie, Matrices de diffusion, Diffusion de la surface de la mer, Cible détection**



---

# Contents

<b>Acknowledgement</b>	<b>i</b>
<b>Abstract</b>	<b>iii</b>
<b>Résumé</b>	<b>v</b>
<b>Table of contents</b>	<b>x</b>
<b>List of figures</b>	<b>xi</b>
<b>List of tables</b>	<b>xv</b>
<b>1 Introduction</b>	<b>1</b>
1.1 Polarization of SAR em wave . . . . .	2
1.2 Polarimetric SAR target . . . . .	5
1.3 Polarimetric Sea surface scattering models . . . . .	8
1.4 Polarimetric K distribution . . . . .	11
1.5 Organization of chapters . . . . .	13
<b>2 SAR sea surface characteristics</b>	<b>15</b>
2.1 Theories . . . . .	17
2.1.1 Polarization signature . . . . .	17
2.1.2 CTD Model based decomposition . . . . .	20
2.1.3 Incoherent target decomposition and partially coherent sea surface . .	21
2.2 Simple model . . . . .	22
2.2.1 Sea surface imaging formation . . . . .	22

2.2.2	Simple model as polarization difference . . . . .	28
2.3	Preliminary result and discussion . . . . .	34
2.3.1	Wind and wave data . . . . .	34
2.3.2	Doppler analysis . . . . .	36
2.3.2.1	Azimuthal Doppler centroid and wind sea . . . . .	40
2.3.2.2	Azimuthal cut-off wavelength and wind sea . . . . .	41
2.3.3	Spectral analysis . . . . .	45
2.4	Discussion and conclusion . . . . .	46
<b>3</b>	<b>Statistical analysis</b>	<b>51</b>
3.1	Theories . . . . .	53
3.1.1	Complex circular Gaussian model . . . . .	53
3.1.1.1	Phase and circular Gaussian . . . . .	53
3.1.1.2	Multivariate complex Gaussian distribution . . . . .	55
3.1.1.3	Gamma distribution . . . . .	55
3.1.1.4	Wishart distribution, coherence, and phase difference . . . . .	56
3.1.1.5	Non-Gaussian cases . . . . .	57
3.1.2	<i>K</i> – distribution family . . . . .	58
3.1.2.1	Correlation effect . . . . .	58
3.1.2.2	<i>K</i> – distribution . . . . .	59
3.1.2.3	Generalized- <i>K</i> . . . . .	60
3.2	ENL analysis . . . . .	60
3.2.1	ENL and Chi-square test . . . . .	62
3.2.2	Generalized K motivated by ENL analysis . . . . .	65
3.2.3	Polarization and non-polarization contributions over the sea surface . . . . .	67
3.2.3.1	Polarized- <i>K</i> distribution . . . . .	68
3.2.3.2	Parameterization . . . . .	69
3.3	Availability of <i>Pol</i> – <i>K</i> distribution . . . . .	71
3.3.1	Single look complex data . . . . .	72
3.3.1.1	Second order statistics . . . . .	73
3.3.1.2	Sub-band decomposition . . . . .	74

---

3.3.2	Intensity detected data . . . . .	77
3.3.3	Amplitude detected data . . . . .	78
3.4	Discussion and conclusion . . . . .	78
<b>4</b>	<b>Target detection</b>	<b>81</b>
4.1	Polarimetric Bayesian detectors . . . . .	83
4.1.1	OPD . . . . .	83
4.1.2	PWF . . . . .	83
4.1.3	PGLRTs . . . . .	84
4.1.4	TD-GLRT . . . . .	85
4.1.4.1	Modelling the background . . . . .	86
4.1.4.2	Modelling the target . . . . .	86
4.2	TD-GLRT detection . . . . .	89
4.2.1	ENL estimator . . . . .	89
4.2.2	TD-GLRT test . . . . .	91
4.3	Discussion and conclusion . . . . .	93
<b>5</b>	<b>Conclusion and Perspectives</b>	<b>97</b>
<b>A</b>	<b>Analytical solution of the radar equation</b>	<b>101</b>
A.1	Definitions . . . . .	101
A.1.1	Target Characteristics . . . . .	101
A.1.2	Radar equation . . . . .	102
A.2	Stratton-Chu integral formulation . . . . .	103
<b>B</b>	<b>Scatterometer operation</b>	<b>105</b>
B.1	Wind definition . . . . .	105
B.2	ASCAT . . . . .	106
B.3	CMOD2 . . . . .	106

<b>C Glossary</b>	<b>109</b>
C.1 Abbreviation . . . . .	109
C.2 Notation . . . . .	110
C.3 Terminology . . . . .	110
C.3.1 Oceanography . . . . .	110
C.3.2 RADAR . . . . .	113
C.3.3 Statistics . . . . .	116
<b>D Publications</b>	<b>119</b>

---

# List of Figures

1.1	Electric field of EM wave expressed in the orthogonal polarization basis . . .	3
1.2	Polarization ellipse of em wave . . . . .	4
1.3	FSA for bi-station (left) vs. BSA for bi-station (middle) and BSA for mono-station (right) alignments in [1] . . . . .	6
1.4	Sea clutter and ship target (photo from internet) . . . . .	12
2.1	Bragg scatterer, Specular and Rayleigh foams . . . . .	16
2.2	Co-polarization and cross-polarization signature of a dipole . . . . .	18
2.3	Co-polarization and cross-polarization signature of an orientated dipole ( $45^\circ$ )	19
2.4	Co-polarization and cross-polarization signature of a dihedral . . . . .	19
2.5	Co-polarization Bragglike signature of a roughsurface . . . . .	20
2.6	Sea surface wave effect on SAR imaging . . . . .	23
2.7	Orbital motion of water molecule in the moving waves . . . . .	23
2.8	Right looking geometry of SAR imaging over the sea surface . . . . .	25
2.9	Random walk of Bragg vs scalar, co-pol. Solid line represents the random walk of Bragg scattering and the vector sum has a phase bragg, dashed line represents the random walk of Scalar scattering and result in the vector sum with a phase scalar, and the radar measurements (HH and VV) is the vector sum of Bragg vector and Scalar vector, with a phase of phase pixel. . . . .	31
2.10	Iteration flow chart . . . . .	34
2.11	Validation flow chart . . . . .	36
2.12	Polarization ratio and depolarization HV. . . . .	37
2.13	Polarization ratio of Tilt Bragg. (Iteration 1,2,3,4,5,6) . . . . .	38
2.14	Sigma-naught of co-pol . (Iteration 0,1,6) . . . . .	39

2.15 Doppler centroid predicted by satellite orbit parameters, for one scene of ScanSAR mode, ascending pass . . . . .	41
2.16 Doppler residual estimate by co-pol, Bragg, and scalar . . . . .	42
2.17 Doppler frequency cross- and co-spectra . . . . .	43
2.18 Cut-off estimate by co-pol Bragg and scalar scattering . . . . .	44
2.19 Three Butterworth filters for spectrum splitting . . . . .	46
2.20 Spectra partitions . . . . .	47
2.21 NRCS HH and VV vs. sum of NRCS Bragg and NRCS Scalar, data No.20111205	48
2.22 NRCS HH (square), VV (diamond), and conj(BraggVV)*Scalar (star) . . . .	49
2.23 Location of data set. . . . .	49
2.24 spectra for windseas, top: Scalar (left) vs. VV (right), data No.20110904; bottom: BraggVV (left) vs. VV (right), data No.20120509. . . . .	50
3.1 Random walk on the complex plain of backscatters for isolated single pixel area	54
3.2 ENL of ABCD magnitude vs. sigma nought for HH and HV, averaged in azimuth direction . . . . .	64
3.3 GUI presents the ENL distribution for a sub image, with the rainbow color showing the ENL map from a low value of blue from the slick areas to a high value of red by the homogeneous area. Sub image size of $473 \times 473$ pixels, center : $1.1271450E, 40.058058N$ , centerincidenceangle : $23.7285deg$ .	65
3.4 Test ratio of Gamma over Gaussian as function of ENL, (a) for the magnitude Gamma distribution performs better than Gaussian at the lower value of the ENL, i.e., where has a heavy contaminated area. (b) for sigma nought the advantage of Gamma distribution has not clear advantages over Gaussian distribution. . . . .	67
3.5 Pol-K detection . . . . .	69
3.6 SLC decompositon and their circular Gaussian distribution . . . . .	72
3.7 SLC decompositon and their amplitudes . . . . .	73
3.8 Histogram of real and imaginary parts of BraggHH and Scalar at the 6th iteration	74
3.9 Histogram of amplitude for VV/HH, BraggVV/HH and Scalar, at the 6th iteration . . . . .	75
3.10 SLC subimage (VV) . . . . .	76
3.11 Sublooking process . . . . .	76

---

3.12	2-look processed from Figure 3.10 . . . . .	77
3.13	Comparison of Pol-K vs. K distribution for a 1024*1024 sub image . . . . .	79
4.1	Bragg and Scalar ship subimage, Co-pol, 6th Iteration. The high target-background-ratio of Scalar contribution in comparison with those from Bragg contribution, especially when zoomed in (right column) . . . . .	87
4.2	Amplitude histograms for Bragg and Scalar ship subimage vs. HH, 6th Iteration	89
4.3	ENL histogram with two definitive peaks indicating a good candidate for thresholding . . . . .	90
4.4	Homogeneity shown on the ENL map of the subimage . . . . .	91
4.5	PDF for target ( $H_1$ )andwater( $H_0$ ) . . . . .	92
4.6	Pol-K-modelled target ( $H_1$ )andwater( $H_0$ ) . . . . .	93
4.7	Homogeneity detection by ENL . . . . .	95
4.8	TD-GLRT detection . . . . .	96



---

# List of Tables

1.1	Satellite imaging SAR summary . . . . .	2
2.1	OSMC Wind and Wave . . . . .	35
2.2	Douglas sea state . . . . .	35
3.1	Description of RADARSAT-2 SAR data for the experiment . . . . .	61
3.2	Description of RADARSAT-2 SAR data for the experiment (cont.) . . . . .	61
3.3	Modified Chi-square test . . . . .	66
3.4	Pol-K parameters . . . . .	78
4.1	Radarsat 2 C-band data set . . . . .	94



During world war II, radar was much engaged to detect and track hostile vessels. Soon it was noted that this detection was more and more hampered with increasing wind speed [2]. As one of the main meteorological variables in sea-state forecasting models, wind energy generates sea surface roughness and then longer waves propagating for a long time to a far distance. Radar signal returned from the sea surface could be inevitably modulated by both roughness and the longer waves. After the war, radar has been much developed for civil use with the development of synthetic aperture radar (SAR) in the 60's. Imaging SAR working on X-, C-, L-, or Ku-band provide 2-D information all over the seas on the Earth for every few days, such as the one on-board the first non-military spacecraft Seasat (1978), the one on-board the first European earth observing satellite ERS-1, and polarimetric SAR loaded on the commercial satellite Radarsat-2 (as in Table 1.1). Moreover, dual- and quad-polarization SAR sensors supply information of scattering mechanism as a third dimension measurement, which endows polarimetry an inevitable basic tool for understanding SAR imageries.

It is known that over the ocean surface one can find man-made target such as oil platforms, wind farms, and frequently oil spills as well as daily maritime transports. Sea surface target detection is not a military requirement any more, but a prior problem for interpreting SAR imagery over the real sea. For the natural ocean surface, there are improved electromagnetic (em) scattering models such as the extended two-scale model [3], wherein the sea spikes (very high radar returned signal) may cause the false alarms by being considered as a man-made target, such as ship or oil platforms. The objective of this work is to separate different scattering mechanisms over the sea surface physically, i.e., by the polarimetric scattering matrix, and try to understand the difference (scattering, energy power) in detail. This improved understanding may help to retrieve the sea surface wave characteristics and

**Table 1.1** — Satellite imaging SAR summary

satellite	frequency	duration	polarization
SeaSAT	L	1978	HH
ERS-1	C	1991	VV
JERS-1	L	1992	HH
ENVISAT	C	2002-2012	HH+HV,VV+VH
PALSAR/ALOS	L	2006-2011	HH+VV+HV+VH
TerraSAR-X	X	2007-	HH+VV+HV+VH
RADARSAT-2	C	2007-	HH+VV+HV+VH
COSMO-SkyMed	X	2007-	HH+HV,VV+VH
TanDEM-X	X	2010-	HH+VV+HV+VH
Sentinel-1A	C	2013-	HH+HV,VV+VH

to detect man-made targets.

## 1.1 Polarization of SAR em wave

Polarimetry theory dates back to the foundation of em wave theory by Maxwell [4]. Henri Poincaré formalized many useful concepts in polarisation optics using geometrical approach, followed by R. Clark Jones who used the formal matrix algebra to describe the propagation of vector waves for the first time. Hans Mueller developed a matrix calculus for dealing with partially polarised waves. Until 1952 when Edward Kennaugh [5] applied the matrix algebra to radar scattering, the polarised EM wave had started to be used in the radar community, where the wave polarization concept has been introduced.

Since the earliest dual-polarised side-looking imaging radar, the Ka-band real-aperture system APQ-97 flown by the Westinghouse Corporation for civilian use in the 1960s, the dual-polarised (like- and cross-polarised) paradigm for Earth observing radars, in particular for SAR, has seen very little change over the past 40 years [6]. So far, operational polarization radar is usually designed to transmit monochromatic plane em wave in horizontal polarization and then vertical polarization alternatively. As the first commercial space-borne SAR satellite, RADARSAT-2 (R2) transmitter sends out em wave in horizontal ( $H$ ) and vertical ( $V$ ) polarization alternatively, and the receiver collects backscattered em wave in  $H$  and  $V$  polarization simultaneously, thus obtain like-polarised information in  $HH, VV$ , and cross-polarised information in  $VH$  and  $VV$ . A monochromatic plane em wave having its electronic field  $\vec{E}$  in any polarization can be expressed in an orthogonal polarization basis which

is perpendicular to the line of wave propagation, as in figure 1.1, which shows a common orthogonal basis with the horizontal axis ( $x$ ) parallels to earth's surface [7] while the vertical axis ( $y$ ) is perpendicular to this horizontal axis. The direction of wave propagation ( $z$ ) is perpendicular to the plane of orthogonal basis ( $x - y$ ).

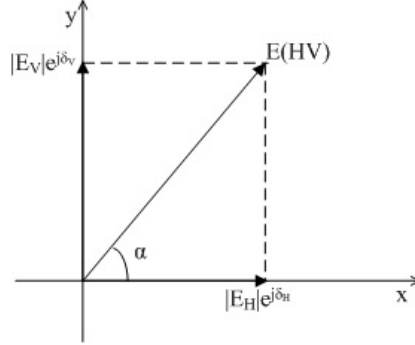


**Figure 1.1** — Electric field of EM wave expressed in the orthogonal polarization basis

In this horizontal-vertical basis, the electric field

$$\vec{E}(HV) = \hat{h}_H |E_h| e^{j\delta_h} + \hat{h}_V |E_v| e^{j\delta_v} \quad (1.1)$$

where  $\hat{h}_H$  and  $\hat{h}_V$  is the unit vector of the orthogonal basis. The complex polarization transformation ratio could be introduced as  $\rho_{HV} = |E_v/E_H| e^{j(\delta_v - \delta_H)} = \tan \alpha e^{j\delta_{HV}}$ , and then the electronic field could be expressed by the ratio  $\rho_{HV}$  and the total power ( $A$ ) as

$$\vec{E}(HV) = A \cos \alpha (\hat{h}_H + \rho_{HV} \hat{h}_V) \quad (1.2)$$

indicating that the phase of each orthogonal components is not definitive for the em wave but the phase difference is.

Viewed towards the em wave's propagation, the trace of the electronic field is normally an ellipticity, since the total power of electronic field is a sinusoid function of time according to the resolution of the Maxwell equation. Because of this, the polarization state of the em wave is called elliptical polarization, as shown in figure 1.2 where the directions  $x$  and  $y$  stands for the horizontal-vertical basis.

It is straightforward from the expression of (1.2) that the phase difference  $\delta_{HV}$  defines the shape of the ellipticity. If  $\delta_{HV} = 0$ , when the two orthogonal components are 'in phase', the electronic field will be along the line with an angle of  $\alpha$  to the horizontal direction; or if  $\delta_{HV} = 180^\circ$ , the electronic field will along the other line which is asymmetric with the former according to the horizontal direction. For these cases, the polarization of the electronic field is linear polarization. Furthermore, if the ratio angle  $\alpha = 0$  or  $\alpha = 90^\circ$ , the electronic field is

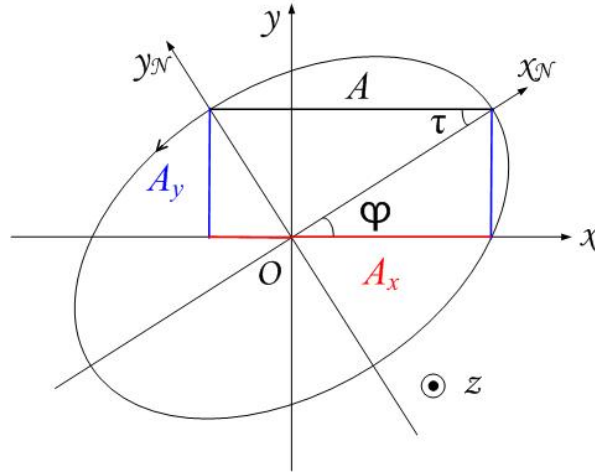


Figure 1.2 — Polarization ellipse of em wave

horizontally polarised or vertically polarised. Another special case is when  $\delta_{HV} = \pm 90^\circ$ , the trace of electric field grows to a circle, and the polarization is circular (left or right).

Figure 1.2 shows a new orthogonal basis of  $(x_N - y_N)$ , with axes along the major axis and minor axis of the polarization ellipse. The angle  $\tau$  denotes the shape of the ellipse and when  $\tau = 0$  the electric field is linearly polarized. The angle  $\phi$  denotes the orientation of the ellipse, and especially for the linear polarization the  $\phi = 0$  or  $\phi = 180^\circ$  indicates a horizontal polarization while the  $\phi = 90^\circ$  or  $\phi = -90^\circ$  indicates the vertical. The angle  $\tau$  is called the polarization elliptical angle, and  $\phi$  the polarization orientation angle. The orientation angle  $\phi$  depends on the choice of horizontal axis, e.g. it is easier to be 0 in the new orthogonal basis  $(x_N - y_N)$ . The distance between intersections of the major and minor axis with the ellipse  $A$  is the amplitude of the electric field. The sign of  $\tau$  determines the rotation, i.e., plus denotes right rotation while minus indicates left rotation. Specially, when  $\tau = 45^\circ$ , the ellipse polarization expands to circular polarization with uncertain orientation angle. For circular polarization, the initial rotation of the electric field decides the left rotation or right rotation. For a general case,  $\alpha_{HV}$  and  $\delta_{HV}$  has the relationship with  $\phi$  and  $\tau$  as [8]

$$\cos 2\alpha_{HV} = \cos 2\phi \cos 2\tau \quad (1.3)$$

$$\tan \delta_{HV} = \tan 2\tau / \sin 2\phi \quad (1.4)$$

EM wave with any polarization could be expressed by 2D vectors such as the complex (amplitude and phase) Jones vector (formula (1.5)) and real (power) Stokes vector (formula (1.6)), wherein the subscripts  $x y$  stands for orthogonal components separately along the horizontal direction and vertical direction. The complex Jones vector could be written as product of unit matrices, which is especially applicable for the transform of elliptical coordinate system  $(\tau - \phi)$ . The power form of Stokes vector is better for radar backscatter

measurements.

$$\mathbf{E} = \begin{bmatrix} E_h = E_{0x}e^{j\delta_x} \\ E_v = E_{0y}e^{j\delta_y} \end{bmatrix} \quad (1.5)$$

$$g_{\mathbf{E}} = \begin{bmatrix} g_0 = |E_x|^2 + |E_y|^2 \\ g_1 = |E_x|^2 - |E_y|^2 \\ g_2 = 2\Re(E_x E_y^*) \\ g_3 = -2\Im(E_x E_y^*) \end{bmatrix} \quad (1.6)$$

The first Stokes vector is the total intensity of electronic field, while the other three parameters describe the polarization state of the em wave.  $g_1$  is the absolute intensity according to the horizontal direction (if  $g_1 > 0$ ) or the vertical direction (if  $g_1 < 0$ ).  $g_2$  indicates the part of linear polarization beyond the axes while  $g_3$  indicates the part of circular polarization. Straightforwardly,  $(g_0)^2 = (g_1)^2 + (g_2)^2 + (g_3)^2$ , and specially,  $g_0 = g_1, g_2 = g_3 = 0$  indicates linearly horizontal or vertical polarization,  $g_0 = g_3, g_1 = g_2 = 0$  indicates circularly polarised wave,  $g_1 = g_2 = g_3 = 0$  indicates unpolarised (that is, randomly polarised) wave [9].

The monochromatic plane em wave interacted with the earth surface, backscattered and received by the radar receiver. If the surface is stationary, backscattered em waves still have the same polarization with each other. On the contrary, if the surface varies with time and position, e.g. due to the sea state, transmitted em waves, in one resolution area, naturally interact with different scatters, thus have different polarizations, the resulted signal resolved for this area is partial polarised. The stationary surface is referred to as stationary target or pure target, while the dynamic surface is called distributed target, also referred to as partial scatter analogously to the partial polarised em wave. The sea surface is typical distributed radar target.

## 1.2 Polarimetric SAR target

The pulse of em wave from the transmitter to the earth surface till the radar receiver travels through three fields, which centered at the transmitter, the scatter, and the receiver, and could be separately described by right hand coordinate system as  $(x_T, y_T, z_T)$ ,  $(x_S, y_S, z_S)$  and  $(x_R, y_R, z_R)$ . Two alignments, the forward scattering alignment (FSA) and backscattering alignment (BSA), are usually used in the definition of the three fields. FSA and BSA have the same definition for  $(x_T, y_T, z_T)$  and  $(x_S, y_S, z_S)$  coordinates, with  $z_T$  from transmitting antenna to the target and  $z_S$  from scatter to the receiver. The difference lies in the  $z_R$  direction. FSA defines  $z_R$  directing toward the em wave propagation direction, so FSA is also called wave oriented alignment and usually used for bi-station radar system; BSA defines  $z_R$  departing the antenna, hence it is also called antenna oriented alignment and usually used

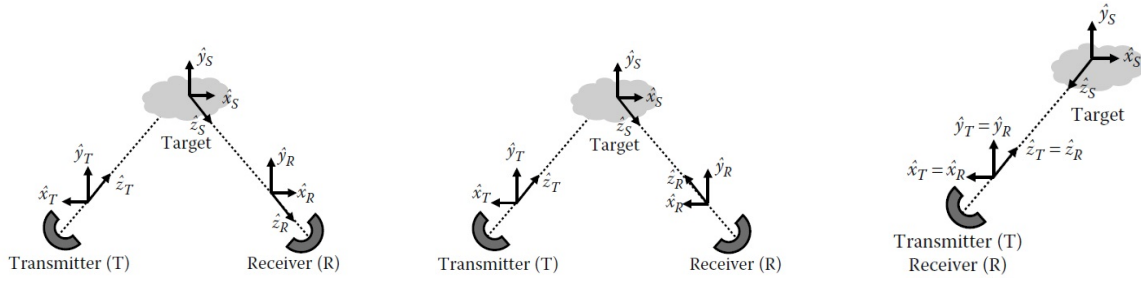


**Figure 1.3** — FSA for bi-station (left) vs. BSA for bi-station (middle) and BSA for mono-station (right) alignments in [1]

for single station radar system. The coordinate geometry introduced in [1] is shown in figure 1.3.

The radar receiver obtains horizontal  $H$  polarization and vertical  $V$  polarization backscattered em waves simultaneously, collecting  $HH$ ,  $HV$ ,  $VH$ , and  $VV$  quad-combination of polarization information, which is usually represented by matrix. The direct measurement of the radar receiver connects with the transmitted em wave as

$$E^s = \frac{1}{\sqrt{4\pi r}} S E^i e^{jkr}$$

by the scattering/backscattering matrix

$$S = \begin{bmatrix} S_{HH} & S_{HV} \\ S_{VH} & S_{VV} \end{bmatrix}$$

where  $S_{pq}$  indicates the received signal of  $p$  polarization from the  $q$  polarized transmitted em wave. The distance  $r$  from the point at which the field is measured to the target where the Sinclair matrix elements are determined,  $E^i$  is the incident electric field which is related to the transmitting antenna effective length by

$$E^i = \frac{jZ_0 I}{2\lambda r} h_t e^{jkr}$$

in which  $Z_0$  is the characteristic impedance of the medium,  $I$  is the transmitting antenna current at some chosen point,  $\lambda$  is the wavelength and  $h_t$  is the effective length of the transmitting antenna.

In the coordinate system obeying FSA for bi-station radar system, the scattering matrix directly measured from Jones vectors also refers to Jones matrix. In BSA coordinate system for single station radar system, the backscattering matrix is called Sinclair matrix [7]. Jones matrix and Sinclair matrix describes the transformation of the Jones vector of the incident beam into the Jones vector of the scattered beam. So far, the satellite SAR imagery is generally single station problem, and the Sinclair matrix will be used.

It is frequently found in literatures [5, 7, 10, 11, 12] indicating that Sinclair matrix is a coherent scattering matrix, while for the incoherent scattering, such as a partially polarized distribution target, only the statistical average is available, wherein the Stokes reflection or Mueller scattering matrix (in FSA) or Kennaugh matrix (in BSA) fit. According to the size of the target, the one has a size smaller than the radar beam width is defined as the point target, while the one larger than the radar beam width is the extent target. Point target could be generally considered as pure target since it would be stationary and coherent during the time of interaction with one single beam, and could be sufficiently characterized by the effective scattering cross section. Extent target is usually also distributed target, which need much more incoherent backscattered radar waves belonging to different beams, and in this case the radar scattering coefficient as the statistical average is applicable. For the coherent scattering target (point target), the received power equation is

$$W_c = \frac{Z_0^2 I^2}{128\pi R_a \lambda^2 r^4} (h_r \otimes h_r^*)^T \kappa_s (h_t \otimes h_t^*)$$

with the definition of Kronecker-product target matrix as

$$\kappa_s = S \otimes S^* = \begin{bmatrix} |S_{xx}|^2 & S_{xx}S_{xy}^* & S_{xy}S_{xx}^* & |S_{xy}|^2 \\ S_{xx}S_{yx}^* & S_{xx}S_{yy}^* & S_{xy}S_{yx}^* & S_{xy}S_{yy}^* \\ S_{yx}S_{xx}^* & S_{yx}S_{xy}^* & S_{yy}S_{xx}^* & S_{yy}S_{xy}^* \\ |S_{yx}|^2 & S_{yx}S_{yy}^* & S_{yy}S_{yx}^* & |S_{yy}|^2 \end{bmatrix} \quad (1.7)$$

and  $R_a$  is the antenna resistance. The Kennaugh matrix of the target is defined as  $K = Q^* \kappa_s Q^{-1}$ . As the development from Sinclair matrix to Kennaugh matrix in BSA, a parallel development from Jones matrix to Mueller matrix could be in FSA convention. For the incoherent target (distributed target), whose scattered wave varies with time, each measurement of the target with a radar pulse yields a Sinclair matrix  $S$ , from which the  $\kappa_s$  can be formed:

$$W_{av} = \frac{Z_0^2 I^2}{128\pi R_a \lambda^2 r^4} (h_r \otimes h_r^*)^T \langle \kappa_s \rangle (h_t \otimes h_t^*)$$

where  $\langle \kappa_s \rangle = \frac{1}{N} \sum_1^N \kappa_{sn}$ , with the angle brackets symbolizes pulse averaging, and the Kennaugh matrix of the target is defined as  $K = Q^* \langle \kappa_s \rangle Q^{-1}$  should be symmetric.

During the early days of radar polarimetry, the statistical average had been the conventional source of data [13, 7, 14], till when the single look complex (SLC) data products available to enable the coherent Sinclair scattering matrix [11]. With the complex components supplied by SLC product, in order to use covariance matrix for power calculation [10], the classical  $2 \times 2$  coherent scattering matrix could be vectorized by a set of complex basis matrices which are orthonormal set under an hermitian inner product, among which are two important, Pauli and Lexicographic.

The set of Pauli basis matrices are

$$\Psi_P = \left( \left[ \begin{array}{cc} 1 & 0 \\ 0 & 1 \end{array} \right], \left[ \begin{array}{cc} 1 & 0 \\ 0 & -1 \end{array} \right], \left[ \begin{array}{cc} 0 & 1 \\ 1 & 0 \end{array} \right], \left[ \begin{array}{cc} 0 & -i \\ i & 0 \end{array} \right] \right) \quad (1.8)$$

and the Lexicographic basis matrices are

$$\Psi_L = \left( \left[ \begin{array}{cc} 1 & 0 \\ 0 & 0 \end{array} \right], \left[ \begin{array}{cc} 0 & 1 \\ 0 & 0 \end{array} \right], \left[ \begin{array}{cc} 0 & 0 \\ 1 & 0 \end{array} \right], \left[ \begin{array}{cc} 0 & 0 \\ 0 & 1 \end{array} \right] \right) \quad (1.9)$$

The target vectors in these bases have the form of

$$k_P = \text{Trace}(S\Psi_P) = [S_{HH} + S_{VV}, S_{HH} - S_{VV}, S_{HV} + S_{VH}, j(S_{HV} - S_{VH})]^T$$

and

$$k_L = \text{Trace}(S\Psi_L) = [S_{HH}, S_{HV}, S_{VH}, S_{VV}]^T.$$

Pauli vector  $k_P$  is more related to physical characteristics of scatters. Specially for distributed radar target which has partially polarization property, the coherency matrix

$$T = \langle k_P \cdot k_P^{*T} \rangle$$

and covariance matrix

$$C = \langle k_L \cdot k_L^{*T} \rangle$$

respectively formed by Pauli and Lexicographer vector, are statistical average, with the  $\langle \rangle$  indicates temporal or spatial ensemble averaging. Partially polarization target could not be characterised by a single coherent scattering matrix, although every scattering matrix  $S$  corresponds to one coherency and covariance matrix.

### 1.3 Polarimetric Sea surface scattering models

The sea surface is well-known distributed target which incoherently scatters the incident polarized em wave into partially polarized backscattering. It has been a problem of history to study the em wave scattering property, especially the depolarization, of the sea surface [15]. EM wave scattered by a small particle or a collection of small particles has different polarization characteristics from those of the incident beam. If the incident beam is unpolarised, i.e. randomly polarized like the sunlight, the em wave passing by a polarizer is polarized according to the polarizer configuration, and this phenomenon is 'polarization'. On the contrary, if the incident beam is fully polarised (linear or circular, which is always the case for space-born polarization radars), the scattered em wave may become partially polarised or even totally unpolarised, and this phenomenon is called 'depolarization' [9]. Thus depolarization of polarization radar scattering is commonly investigated to identify different scattering

mechanisms. Valenzuela [16] investigated sea surface depolarization following Rice's method for slightly rough surface, indicated that polarization ratio of VV over HH increases with the absolute magnitude of the complex dielectric constant of the scattering surface. Since then, depolarization has been investigated widely with the asymptotic modeling improvements. A family of unified models based on local corrections of the tangent plane approximation (KA which has no polarization sensitivity) through higher-order derivatives of the surface have been worked out. For co-polarization components, advanced models such as small slope approximation (SSA, where the first order solution, SSA-1, considers only the SPM kernel to first order  $\mathbf{B}(k, k_0)$  [17]) overestimate the polarization ratio with the increase of the incidence angle; two scale model (TSM) and local curvature approximation (LCA, where the first order solution LCA-1 could be rewritten with the same formulation as TSM [18]) predict sea surface NRCS with reduced ratio of VV over HH, but still overestimated from the moderate incidence angles and even worse at the high incidence angles.

Recently improved resonant curvature approximation (RCA) [18] reduces the polarization correction by replacing the integrated wave number with the resonant Bragg wave number for LCA-1. Besides of the incidence angle modulation of PR, both LCA and RCA are able to reproduce an azimuth modulation of PR, which has already been presented by former experiments and observations [19, 20, 21, 22]. The success of RCA recalled the focus on the Bragg resonant contribution to the sea surface RCS measurements, as PR has been found to be the result of the relative contribution of polarised and non-polarised (scalar) part of the backscattered signal, which respectively correspond to polarised Bragg scattering and non-polarised scattering such as specular, the small-scale breaking, and foam etc. In fact the necessary presence of small ripples to generate upwind-downwind asymmetry (UDA) and upwind-crosswind anisotropy (UCA) has already been indicated by Cox and Munk's measurements [21]. Breaking waves has been included into the description of the scattering process by Kudryavtsev et al. [23]. However, in order to apply Kudryavtsev's method to wind inversion however, one must know a priori how the breaking-wave contribution to the NRCS depends on the local wind vector [24].

As proposed by Quilfen et al. [21], co-polarized radar backscatter returns at higher incidence angle can be well separated into two contributions, one of pure Bragg scattering type and one a non-polarized scattering component. In this model, NRCS measurements can be expressed as the sum of a scalar term and a polarization dependent term,

$$\sigma_0^{pp} = \sigma_{sc} + \sigma_{pol}^{pp} \quad (1.10)$$

where  $\sigma_{pol}^{pp}$  is the Bragg contribution in line with small perturbation theory [25], for which the normalized radar cross-section  $\sigma_{0br}^{pp}$  is proportional to the surface elevation spectrum at

the Bragg wave number [26] with the polarization dependence,

$$\sigma_{0br}^{pp} = 16\pi k_r^4 |G_{pp}(\theta)|^2 F_r(\phi, k_{br}) \quad (1.11)$$

where  $pp$  denotes co-polarization state HH or VV,  $k_{br} = 2k_r \sin\theta$  is the Bragg wave number of surface waves scattering radar wave  $k_r$ ,  $\theta$  is the incidence angle,  $\phi$  is the antenna azimuth,  $F_r(\phi, k)$  is the 2D-wave number variance (folded) spectrum of the sea surface displacement. For pure Bragg process,  $G_{pp}$  is the Bragg scattering geometric coefficient for HH or VV, they are functions of local incidence angle at fixed dielectric permittivity, depending on antenna polarization, for example (equation (29,30) in [27])

$$|G_{vv}(\theta)|^2 = \frac{\cos^4 \theta (1 + \sin^2 \theta)^2}{(\cos \theta + 0.111)^4}, |G_{hh}(\theta)|^2 = \frac{\cos^4 \theta}{(0.111 \cos \theta + 1)^4} \quad (1.12)$$

when the water dielectric permittivity is set to be 81.

In real conditions, wind driven sea surface ripples and fluctuates over the longer gravity waves. A SPM model as pure Bragg wave could not exist alone but always riding on a longer wave, i.e., a series of tilted patches [28]. This approach of modeling was termed by Wright as the composite or the two-scale model [29, 26], to which we will generally refer to as 'tilt Bragg model'. The calculations of the wave scattering problem including the ability to predict quantitatively both the mean radar cross section and mean dynamical quantities can be based upon an extended two-scale model [3]. As well known, tilt enhance depolarization as (equitation 12.122 in [28])

$$E_{vh}^s = \{(\hat{v} \cdot \hat{v}') S_{v'v'}(\hat{v}' \cdot \hat{h}) + (\hat{v} \cdot \hat{h}') S_{h'h'}(\hat{h}' \cdot \hat{h}) + [(\hat{v} \cdot \hat{v}')(\hat{h}' \cdot \hat{h}) + (\hat{v} \cdot \hat{h}')(\hat{v}' \cdot \hat{h})] S_{h'v'}\} E_0 \quad (1.13)$$

in which the first, second, and forth item on the right hand side are introduced by the two-scale tilt, only the third item inherits from the second-order pure Bragg model by SPM, where  $S_{h'v'}$  is equivalent to  $S_{hv}$  replacing  $\theta$  by  $\theta'$ . Similarly, co-polarization has also been introduced with additional  $(\hat{v}' \cdot \hat{h})$  and  $(\hat{v} \cdot \hat{h}')$  items by tilt effect (equitation 12.121 in [28]).

To the first-order approximation, the longer surface wave tilt was considered in the scattering coefficient  $G_{pq}$ , and the normalized radar cross-section  $\sigma_{0br}^{pq}$  is determined by averaging the local scattering coefficients of small patches along the longer surface wave,

$$\sigma_{T.br}^{pq} = 16\pi k_r^4 \overline{|G_{pq}(\theta - \zeta_x, \zeta_y)|^2} F_r(\phi, k'_{br}) \quad (1.14)$$

the bar  $\bar{(\ )}$  denotes an averaging over the long wave,  $\zeta_x$  and  $\zeta_y$  are slopes of the tilting waves along and across the incidence plane. The Bragg wave number  $k'_{br} = 2k_r \sin(\theta - \zeta_x)$ . The scattering coefficient for HH or VV as

$$\begin{aligned} G_{vv}(\theta - \zeta_x, \zeta_y) &= G_{vv}(\theta - \zeta_x) \\ G_{hh}(\theta - \zeta_x, \zeta_y) &= G_{hh}(\theta - \zeta_x) + (\zeta_y / \sin(\theta))^2 G_{vv}(\theta) \end{aligned} \quad (1.15)$$

For tilt Bragg scattering, polarization ratio PR is a function of local incidence angle at fixed dielectric permittivity (for example, when  $\epsilon = 81$ ),

$$PR_{T.br} = \frac{\sigma_{T.br}^{vv}}{\sigma_{T.br}^{hh}} = \frac{\cos^4(\theta - \zeta_x)(1 + \sin^2(\theta - \zeta_x))^2 / (\cos(\theta - \zeta_x) + 0.111)^4}{\frac{\cos^4(\theta - \zeta_x)}{(0.111 \cos(\theta - \zeta_x) + 1)^4} + (\zeta_y / \sin(\theta))^2 \frac{\cos^4 \theta (1 + \sin^2 \theta)^2}{(\cos \theta + 0.111)^4}} \quad (1.16)$$

For the first time, tilt Bragg model considered the important cross-polarized components and connected depolarization with tilt as the first order effect. Other polarimetric model has been studied for sea surface backscattering acquired by multi look complex polarimetric SAR data [30] with a polarimetric coherency matrix, but still no depolarization considered since no tilt was considered in their approach.

## 1.4 Polarimetric K distribution

Another historical problem considering radar scattering from the sea surface deals with the generation of K distribution [31], when pursuing a statistical model for speckle. Speckle has been well-known for all coherent imaging modalities, such as laser imagery [32], optical coherent tomography [33], as well as the speckle-free photoacoustic tomography [34]. Speckle is not really noise but rather contains information on the sensor and observed surface [35], while heretofore, speckle reduction is commonly known as 'filtering', although ill-suited, since speckle appears as a chaotic jumble and fluctuates the backscattered signal with a standard deviation to mean of unity, which is the same property as white noise [35, 32].

Speckle, unlike system noise for SAR imageries, is not really noise but rather contains information on the sensor and observed surface, and is a real em measurement [35, 36]. Once the sea surface structure is resolved by radar imagery pixels, scatterers inside the pixel area are not randomly distributed any more. It was believed that the sea clutter corresponds to sea surface capillary wave. Capillary wave has a periodic structure offering in-phase sum of coherent backscattered signal, then detected by the square law detector as the power of sum. At high sea states, the large number of in-phase signals of sea clutter to sum up may introduce local high, i.e., some level as high as the generic target, e.g. a ship, and this part of sea clutter is called 'sea spike', which may be the principle false alarm for sea surface target detection [37, 38, 31, 39]. Sea spike normally comes from Rayleigh scattering by wave breaking or the wave steep [40], which has high polarization ratio of HH over VV, i.e. higher than that from capillary wave, and large Doppler velocity [37]. At the critical state where the sea surface wave steep has been well established, the interruption of hydrodynamic interaction may generate new capillary wave naturally. During wave breaking, bubbles in the air and foams around the breaking may introduce Rayleigh scattering. As early as 1980s, the limitation of two-scale model has been found when the sea spike appears more easily for HH polarization



Figure 1.4 — Sea clutter and ship target (photo from internet)

than VV [41]. The capillary wave, which contributes as Bragg wave, supply a rough surface, contributing as the variation obeying a circular Gaussian distribution (referred to as a fully developed complex speckle [35]), while breaking waves supply foams and bubbles as a group of Rayleigh scatterers, contributing to the variation obeying a non-Gaussian distribution [42, 35], especially at high incidence angle. See figure 1.4.

The basic assumption of K-distribution is that the scattered electric field can be written as the sum of contributions from  $N$  independent scatterers,

$$\xi(r, t) = e^{j\omega t} \sum_{i=1}^N a_i(r, t) e^{j\varphi_i(r, t)} \quad (1.17)$$

where  $a_i(r, t)$  is a real form factor governing the angular distribution of radiation from the  $i$ th scatterer,  $\varphi_i(r, t)$  is a phase factor depending on its position at time  $t$  with respect to the observation point  $r$ . Defining the RCS  $\sigma(r, t)$  to be equal with the square of the envelope of the field,  $\sigma(r, t) \equiv |\xi(r, t)|^2$ , formula 1.17 describes a 2-D random walk in the complex plane of  $N$  steps of lengths  $\{a_i\}$  which is useful in statistical modelling of the RCS in 2-D plane hence form a 2-D SAR imagery. For single-look polarimetric SAR, the K-distribution can be derived either by assuming that the number of scatterers in a resolution cell has a negative Binomial distribution [43] or by using a product model [44] of a Gaussian distributed complex

vector and a Gamma distributed variable.

Traditional statistical models for sea surface consists of separating the radar target from the backscatter of the real sea surface, however, it is still not a well defined problem to separate the amplitude of the two due to the lack of in-situ measurements of the real sea conditions. Nevertheless, different radar targets, even including the sea surface capillary wave which could be still a kind of radar target, have different polarization properties, it would be another case when using polarimetry data.

## 1.5 Organization of chapters

In our study, sea surface characteristics imaged by RADARSAT-2 multi-polarization SAR have been investigated. For the first time, a decomposition of different scattering mechanisms have been performed for ocean satellite SAR imagery to better understand the non-polarized (Scalar) contribution to the total radar cross section (RCS) and Doppler measurements. Characteristics retrieval and target classification has been established, using polarimetry and Bayesian detection theories. There are generally three types of surface scattering mechanisms occurring when the sea surface is probed by microwave radar, i.e., Bragg, specular, and Rayleigh, which correspond respectively to sea surface capillary wave, the crest of the longer wave before it breaks, and the bubbles and foams formed by wave breaking. Different scattering mechanisms induce different polarimetric scattering coefficients and Doppler spectrum. It had been impossible to split those scattering mechanisms with single polarization radar imageries. At pixel scale, we split radar scattering matrices into Bragg and Scalar contributions. The splitting is an iteration initiated with the radar incidence angle and then controlled by a local incidence angle which is function of co-polarization and cross-polarization.

Based on these developments and testing, a strategy has been refined to analyze the signature of different features, to retrieve wind seas and sea swell parameters, as well as slick areas, ships, oil rigs, such non-polarized targets that may be buried in the Scalar contributions. With polarimetric scattering coefficients estimated both for Bragg and Scalar contributions, a sea clutter model describing almost the real sea surface has been improved, for the first time, according to scattering contributions statistically. On this point, this improved model could be combined with Bayesian detectors to classify man-made metallic targets, such as ships, oil rigs, etc., which had been buried in the Scalar contribution.

Three chapters in the following describe the approach from three viewpoints. From the point of view of an average sea surface approximation, chapter 2 analyses the NRCS (Normalized Radar Cross Section) and Doppler measurement of full polarization RADARSAT 2 SAR data in different polarization channels, as well as the polarization ratio between co-polarization and cross-polarization channels. Chapter 3 analyses from the point of view of

statistical approximation, which is focused on the whole distribution, the ENL(Equivalent Number of Look) characteristic and the separated scattering contributions. In chapter 4 the detection is established by a Bayesian strategy utilising the statistical results from Chapter 3. For the end, chapter 5 concludes the thesis with perspectives.

---

## SAR sea surface characteristics

*It is also the case that direct mathematical inversion is often not the preferred route to solving the Inverse Problem because of its difficulty. Instead, repeated solution of the Forward Problem for different values of the input parameters can be used to achieve consistency with observations. Such methods only become of intrinsic merit when the dimensionality of the observations is sufficient to provide tight constraints on the solution space.*

*Chapter 4 in [36]*

As distributed target, sea surface is measured by SAR as backscattering coefficients. What do these measurements mean over the sea surface, or what kinds of sea surface reconstruct the transmitting chirp signals? For microwave, sea water has a large complex permittivity hence short penetration length. Near vertical incidence angle, specular reflection dominants in the backscattered signal. At moderate incidence angles (typically  $20 - 60^\circ$ ), the theory of radar backscattering is based on the mechanism of resonant microwave scattering from the random rough surface [23, 45]. The em diffraction, usually named as Bragg scattering, breaks up the transmitting em wave and retransmits it by interference. Among the diffracted signals, the one towards the radar will be captured by the mono-static receiver and here comes the backscattered signal. There would be some specular reflections toward the radar from facets happen to be perpendicular to the transmitting em wave, but are normally ignorable. There is still a third kind of possible redirected reflection by the double bounce from a corner like scatterer, which may be formed from breaking waves (where comes the high radar returns

called sea-spikes in chapter 3) or a real corner object from the sea surface target (in chapter 4). When the grazing incident microwave probes the sea surface near the horizontal incidence angle, the backscattered radar signal reduced to around zero [28].

Casual observations have shown that the sea surface is not a random rough surface but a superposition of significant structures. Wind generated ripples transfer their energy into longer waves, till to waves long enough at some point which is ready to break in order to redistribute the wave energy. Wave breaking introduces the sea spike signature on the SAR imagery (what we will discuss in chapter 3 as a source of false alarm). When the wind has been blowing for some time, an equilibrium could be established between the input energy and its dissipation. So far, a wide spectrum of waves propagating on the sea has built up. Moreover, the swell travelling into this area from remote rough weather should also be added to this wave spectrum. All of these waves and breaking events are reflected in the spatial variation of radar backscatter [42]. To interpret SAR imagery, the nature of such variation needs to be characterised.

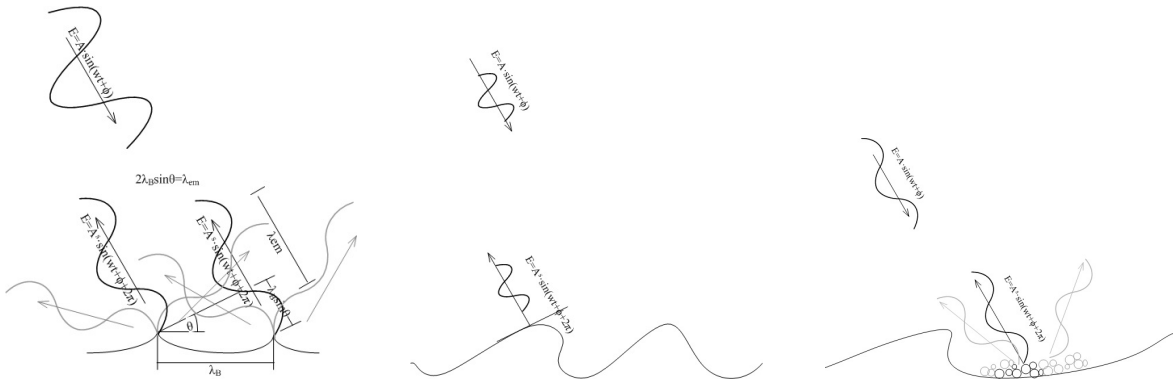


**Figure 2.1** — Bragg scatterer, Specular and Rayleigh foams

The operationally used incidence angle ranges from  $20 - 60^\circ$  for satellite SARs, where the resonant scattering for the medium incidence angle dominates the scattering contribution [28]. According to Bragg's law, the geometric structure (here is the wave peaks) should have a dimension of the wavelength of the em wave to resonate and therefore leading to the interference. The sea surface wave with a wavelength obeying Bragg's law, called Bragg wave which could be sensed by an active radar, normally has a wavelength of centimetres according to the em wave. The surface roughness for radar is in particular the amplitude of the Bragg wave, or up to an order of magnitude longer. Firstly we know that the wind generated short ocean waves contribute as Bragg waves. Take ERS SAR for example, when the wind is between about  $2$  and  $12 \text{ m s}^{-1}$  [46] it optimize the SAR imagery. For wind below this range the backscatter will be close to the SAR noise floor and incapable of revealing modulation. For wind above this range the backscatter will be too high to be modulated

by most ocean phenomena, because the real sea surface has never independent Bragg waves but ones parasitic on the longer waves which should be supplied by swell waves or currents. However, the latter kinds of composed sea surfaces as Bragg waves over longer waves, referred as two scale models, still have discrepancy from radar observations, for the backscattering coefficient of both HH and VV polarizations as well as for the polarization ratio of VV over HH and upwind to downwind ratio [23, 18]. *Ericson et al.*[47] investigated the radar scattering mechanisms associated with wave breaking in laboratory conditions and showed that radar returns near the breaking crest are the results of incoherent backscatters due to the generation and tilting of enhanced surface roughness by breaking waves. They also showed that the Kirchhoff approximation (scalar approximation) reproduces the observations of breaking crest which have a polarization ratio close to unity. Based on their works, we suggest that in addition to specular reflection, wave breaking is also polarization independent, and therefore, Bragg scattering is the only source of depolarization [21, 22].

## 2.1 Theories

### 2.1.1 Polarization signature

To describe the target in real quantities, the electric fields should be described into real elements as the Stokes vector and then the received power equation becomes

$$W_{av} = \frac{Z_0^2 I^2}{256\pi R_a \lambda^2 r^4} (G_{Ar})^T Q^* \langle \kappa_s \rangle Q^{-1} G_{At}$$

in which the Stokes vectors of transmit and received em waves  $G = QJ$  ( $J = E \otimes E^*$  is the complex coherency vector) could be expressed without scalar multiplier of the antenna as

$$G_{Ai} = Q(h_i \otimes h_i^*) = \begin{bmatrix} |h_{ix}|^2 + |h_{iy}|^2 \\ |h_{ix}|^2 - |h_{iy}|^2 \\ 2\text{Re}(h_{ix}^* h_{iy}) \\ 2\text{Im}(h_{ix}^* h_{iy}) \end{bmatrix}, \quad i = t, r \quad (2.1)$$

where

$$Q = \begin{bmatrix} 1 & 0 & 0 & 1 \\ 1 & 0 & 0 & -1 \\ 0 & 1 & 1 & 0 \\ 0 & j & -j & 0 \end{bmatrix}$$

and  $h_i$  is the effective length of the transmitting (i=t) or receiving (i=r) antenna.  $\kappa_s$  is the Kronecker-product target matrix defined in Equation (1.7). According to the relationship between the orthogonal components of the em wave expressed in Equation (1.3) and (1.4),

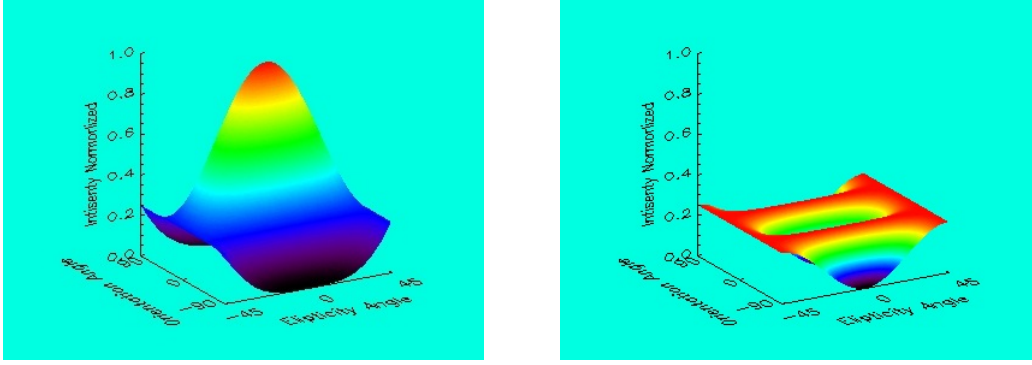


**Figure 2.2** — Co-polarization and cross-polarization signature of a dipole

another representation of Stokes vector as the angles specifying the polarization ellipse could be

$$G_{Ai} = Q \begin{bmatrix} 1 \\ \cos 2\tau \sin 2\phi \\ \cos 2\tau \cos 2\phi \\ \sin 2\tau \end{bmatrix} \quad (2.2)$$

where  $\tau$  and  $\phi$  is the ellipticity and orientation angle respectively of the polarization ellipse and  $\tau \in [-45^\circ, 45^\circ]$ ,  $\phi \in [-90^\circ, 90^\circ]$ . For each arbitrary combination of disposal value for  $\tau$  and  $\phi$ , the received power could be quantified directly as

$$W_{av}(S, \tau_t, \phi_t, \tau_r, \phi_r) = \begin{bmatrix} 1 \\ \cos 2\tau_r \sin 2\phi_r \\ \cos 2\tau_r \cos 2\phi_r \\ \sin 2\tau_r \end{bmatrix}^T K \begin{bmatrix} 1 \\ \cos 2\tau_t \sin 2\phi_t \\ \cos 2\tau_t \cos 2\phi_t \\ \sin 2\tau_t \end{bmatrix}$$

where  $K$  is the Kennaugh matrix. The resulted power is called the polarization signature of the target [48, 49], and the technique of building polarization signature for targets is polarization synthesis. Following this technique, a group of typical polarization signatures of standard scatters had been worked out and helped a lot in the field of target classification.

Two standard scatterers, dipole and dihedral shows in Figure 2.2 to 2.4. A dipole rotated along the plan perpendicular to the line of sight (LOS) is more common in modelling a capillary wave since the surface capillary wave always runs along the passage of a longer wave with a rotation corresponding to an equal shift of orientation angle of the polarization base. The polarization response of an orientated dipole of  $45^\circ$  shows a  $45^\circ$  shift of the signature on the orientation direction (Figure 2.3).

Nasr et. al [50] described the target as a collection of elementary geometric reflectors (EGR), including depolarized double-bounce dihedral structures, depolarized single-bounce dipole structures and polarized single specular reflection. Cylindric scatterers depolarize the

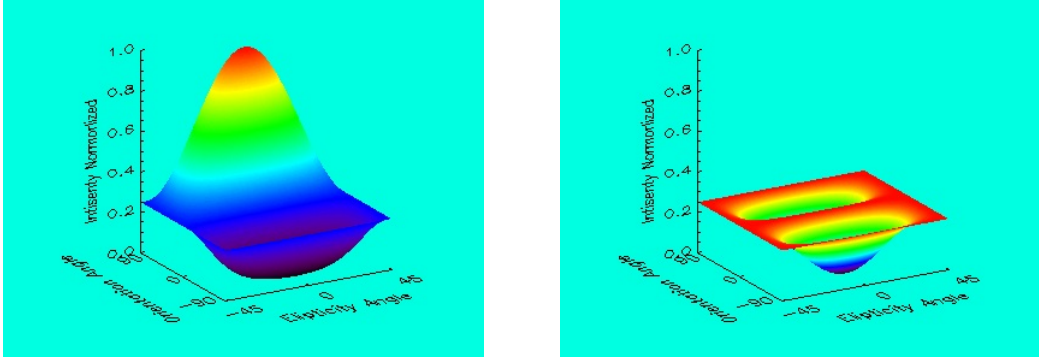


**Figure 2.3** — Co-polarization and cross-polarization signature of an orientated dipole ( $45^\circ$ )

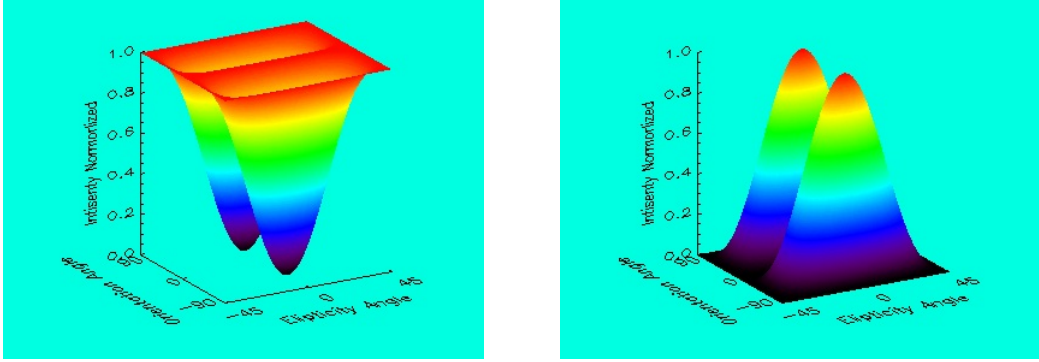


**Figure 2.4** — Co-polarization and cross-polarization signature of a dihedral

incidence field according strictly to the Fresnel reflection coefficients [48], is one kind of dihedral structure. A dihedral corner reflector has the polarization signature as in figure 2.4.

Van Zyl et al. studied the polarization signature of rough dielectric surface [48], to find the Bragglike signatures (in figure 2.5 which will be introduced in following sections) for high incidence angle measurements over the ocean surface. Hajnsek et al. [51] reviewed the two common approximate methods for radar backscattering from rough surfaces, KA and SPM, and gave the scattering matrix of a Bragg surface where the surface roughness  $ks \ll 0.3$  as

$$[S] = \begin{bmatrix} S_{HH} & S_{HV} \\ S_{VH} & S_{VV} \end{bmatrix} = m_s \begin{bmatrix} R_S(\theta, \epsilon) & 0 \\ 0 & R_P(\theta, \epsilon) \end{bmatrix} \quad (2.3)$$

where  $m_s$  is the backscatter amplitude containing the information about the roughness condition of the surface,  $R_S$  and  $R_P$  are the Bragg scattering coefficients perpendicular and parallel to the incidence plane respectively, and functions of the complex permittivity  $\epsilon$  of the ferromagnetic media and the local incidence angle  $\theta$ ,

$$R_S = \frac{\cos \theta - \sqrt{\epsilon - \sin^2 \theta}}{\cos \theta + \sqrt{\epsilon - \sin^2 \theta}}, \quad R_P = \frac{(\epsilon - 1)(\sin^2 \theta - \epsilon(1 + \sin^2 \theta))}{(\epsilon \cos \theta + \sqrt{\epsilon - \sin^2 \theta})^2} \quad (2.4)$$

This expression for scattering matrix is equivalent to the first-order solutions in [16].

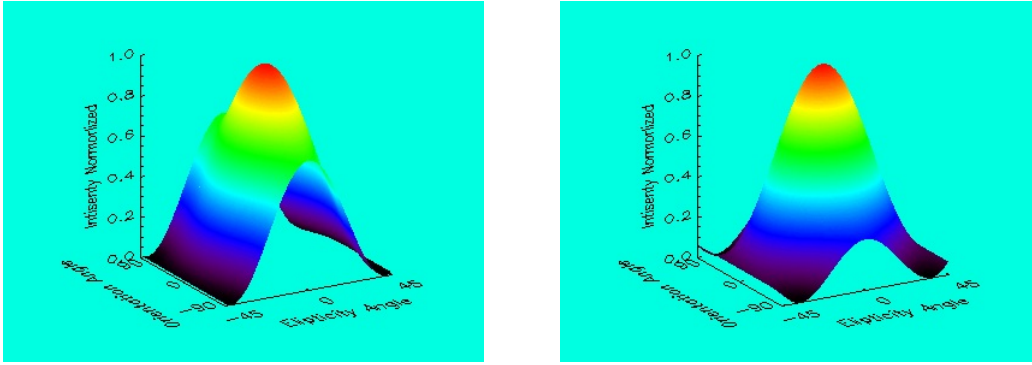


Figure 2.5 — Co-polarization Bragglike signature of a rough surface

### 2.1.2 CTD Model based decomposition

The polarization synthesis technique compose the polarization signature, provided the Ken-  
naugh matrix is known, which is defined by the Sinclair scattering matrix  $S$ . Point target,  
which has definite  $S$ , has definite polarization signature. If we consider point targets as  
members of a group of scatterers which has the radar backscatter  $S$ , the problem of target  
decomposition could be the inverse problem for each of the group of coherent scattering ma-  
trices. Cameron[52] decomposed the scattering matrix based on the two basic properties of  
radar scatterers, reciprocity and symmetry, into eleven classes of scatterers. This decomposi-  
tion were reviewed both in [10] and [53], with opposite opinions [54], starting from where the  
former researchers reached at a new decomposition of H- $\alpha$ -entropy decomposition, while the  
latter researchers followed the Cameron’s decomposition to develop an adaptation referred  
to as SSCM [55].

If we do not focus on the distributed sea surface, instead we consider for each single pixel  
area, i.e. for each facet [56, 57, 58, 59], about the Bragg wave, which has a dimension as  
the dipole, and the foam and bubble introduced by wave breaking, which has a dimension of  
Rayleigh scatterers, and even the specular facet, the problem belongs to Cameron’s coherent  
target decomposition (CTD) problem. Using CTD method, Ringrose et al. analysed SIR-  
C quad polarization SAR complex imageries of ocean to find the main scatterer type is a  
cylinder [60] with an insignificant relationship with wind speed. But Touzi et al. found that  
when the coarse classification scheme of the Cameron method is dropped it becomes apparent  
that less than 1% of ocean pixels are pure cylindrical scatterers [54, 61].

The complex amplitude  $\xi((x_0, y_0))$  of a pixel with coordinates  $(x_0, y_0)$  is either equal to  
the  $S_{ij}$  component of the scattering matrix if we work with calibrated data, or proportional  
to the total backscattered field if the data are not calibrated [35]. Converting measured  
powers to geophysical quantity RCS  $\sigma$  or average backscattering coefficient  $\sigma^0$  requires careful  
calibration and characterization of the system. However, for the purposes of such as mapping,

target detection, and texture measurement, calibration may not be necessary as long as radiometric distortions are changing slowly relative to the features of interest in the scene [36].

### 2.1.3 Incoherent target decomposition and partially coherent sea surface

To validate Huynen-Kennaugh decomposition using the real radar measurement and due to the practical difficulty of measuring the absolute phases for the complex scattering matrix, Van Zyl [62, 48] expressed the scatter transform by the real  $4 \times 4$  Mueller matrix  $M$  instead of the complex  $2 \times 2$  scattering matrix  $S$ . However, by the non-linear average of the incoherent (spatial and temporal variate) target, the transform from  $M$  back to  $S$  is proved to be not unique. Point target, which has definite  $S$ , has definite real matrix  $M$ . If we consider point targets as members of a group of scatterers which has the radar backscatter  $S$ , the problem of target decomposition could be the inverse problem for each of the group of coherent scattering matrices. Based on this knowledge, Claude and Pottier[10] proposed a new decomposition of H- $\alpha$ -entropy decomposition for incoherent targets.

Although it is incoherent radar target considering its unlimited extension and spatial-temporal variation, the sea surface is not perfect random surface and hence the sea surface is not incoherent radar target only. Except for the incoherent radar backscatters from the sea surface supplying a random noisy background, what caught oceanographers' interests are the coherently imaging Bragg resonant, and frequently happened specular reflectors, as well as grouping of surface foams. The coherent imaging is the reason why radar could be used for ocean observation. We noticed that during the early days scientists analysed radar signals as incoherent backscatter [63] and ignored the coherent backscatter [47] due to the low resolution of radar imaging, while the consideration for each single pixel area, i.e. for each facet [56, 57, 58, 59] of different scattering mechanisms makes sense, especially when the recent improvement of the RCA [18] model represented the azimuth polarization variation of the NRCS using Bragg wave number instead of the whole wave spectral. Here we introduce 'partially coherent' to acknowledge the incoherent elements over the sea surface while, not introducing confusion, focus on the coherent scatterers over the surface, such as Bragg waves, specular reflectors, and the Rayleigh foams, according to their polarization properties. Again, the decomposition will be neither coherent target decomposition (CTD) nor incoherent target decomposition (ICTD).

## 2.2 Simple model

### 2.2.1 Sea surface imaging formation

SAR is a method for generating high-resolution radar maps. It is actually an imaging scatterometer (Appendix B). SAR system is characterized by high spatial resolution and radiometric resolution, which determine the amount of information that can be extracted from the image. Spatial resolution is a measure of the accuracy with which the physical dimensions of an object can be determined, and radiometric resolution is a measure of the accuracy with which the microwave reflectivity of the terrain can be ascertained [64]. In signal sampling field, spacing is equivalent to resolution, while it is also the size in meters of each pixel of the imagery in image domain. Being defined as the width of the half power of the impulse response of radar pulse, it's the minimum space separation of two targets or equal cross section that can be resolved as separate targets. In range direction, the range-compression technique has been used to find the balance between long pulse repetition interval (PRI) and pulse length  $\tau_p$  and achieve the high spatial resolution in range direction. The azimuth spacing was improved by using the Doppler shift [65], and therefore, relative motion between the radar platform and the target is the key element in SAR imaging. The formation of a SAR image relies on an accurate model of the imaging system, the transmitted signal, the imaging geometry, the terrain surface and its evolution through time [66].

However, the theoretical basis of SAR principle assumes that the target field is stationary. Whereby waves are imaged? Various effects and properties that contribute to the formation and/or the degradation of satellite SAR images of ocean surface are summarised in [67] such as tilt modulation, hydrodynamic modulation, velocity bunching, and azimuth smearing. To the range direction, the wave imaging process for SAR is the same as that for any type of radar (RAR), commonly described on the basis of a two-scale model, wherein the sea surface radar backscatter is dominated by the statistical average properties of the short waves within the resolution cell, with a modulation by longer waves, which is called tilt modulation, inducing varying surface tilt and straining. Tilt modulation modifies the local incidence plan hence the incidence angle, refer to figure 2.6 (middle), and is supposed to be linear related to the slope of the long waves. The long wave effect on straining is called hydrodynamic modulation, by changing the local roughness distribution heterogeneously. It is usually described by the weakly non-linear formulation, as shown in figure 2.6 (bottom).

To the azimuth direction, the SAR special observation of Doppler history is sensitive to the relative velocity between the radar and the target. In fact, a steady velocity of target in radial direction, say the slant range and we will use 'radial' to mean 'slant range' when referring to Doppler for simplicity, produces three possible effects known as azimuth image shift, range walk, and amplitude reduction. Longer wave orbital motion has large component

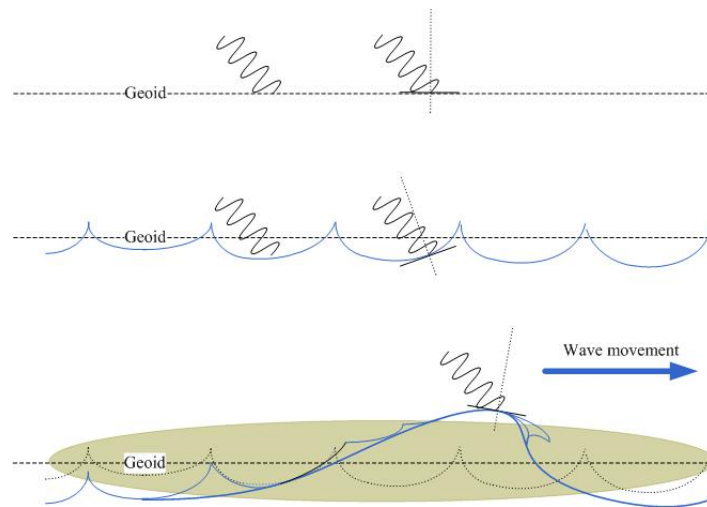


**Figure 2.6** — Sea surface wave effect on SAR imaging

in the radial direction (figure 2.7), therefore is capable of causing constructive or destructive image degradation in the azimuth direction. This may effect on the shorter wave in the azimuth direction too significantly to imaging on the SAR instrument, say there is a non-linear relationship between SAR image spectra and ocean wave spectra, cutting off the shorter waves to be imaged.

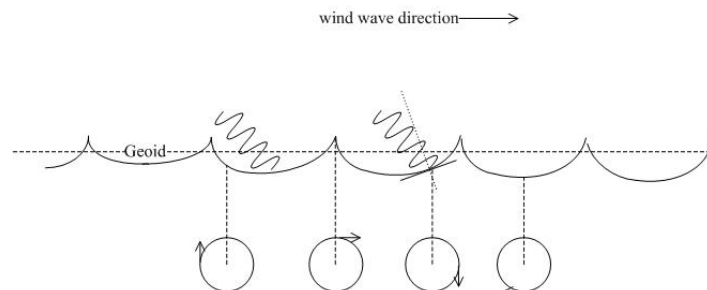


**Figure 2.7** — Orbital motion of water molecule in the moving waves

Besides the azimuth distortion introduced by velocity bunching effect, the wave phase velocity field can also lead to a systematic deterministic mis-registration between successive looks (defocusing effect) [67]. This reduction of along-track resolution associated with both the unresolved random scatter motions and the limited scatter lifetime during the SAR integration time is referred to as azimuth smearing. This effect lowers the apparent image contrast, while it may give the opportunity to remove the directional ambiguity of imaged harmonic components, if one can sufficiently resolve the main wave pattern translation between the different looks as it occurs during the SAR integration time.

Sea state can be completely characterized statistically by the two-dimensional directional wave spectrum  $F(k)$  describing the distribution of wave energy with respect to the wave propagation wave number [45, 68]. Before systematical organized field studies, the theory of wind-generated ocean waves had already been improved since Jeffreys [69, 70] proposed the linear instability mechanisms, which has been supported by Snyder and Cox's measurements in the item of growth but not in the item of growth rate. Both of field studies by Snyder and Cox in 1966 and by Wilkerson in 1967 utilized a single mobile wave station to determine the evolution of the wave spectrum in space and time, and similar exponential growth rate of a single frequency component had been found. Meanwhile, field studies carried out indirectly from measurements at a single fixed location under different wind conditions by Kitaigorodskii in 1962. Based on Kitaigorodskii's scaling law, laboratory experiments has been carried out in late 1960s and early 1970s [71]. Combined with laboratory measurements, the theoretical understanding of wave growth pushed out the first generation wave models in 1960s and early 1970s [72]. In order to interpret the energy interaction between air and sea, wave spectrum has been investigated during 1960s by oceanographers measuring the same locating with different wind speed or by air-born radar altimeter [71]. Direct measurements of the wind as engine for waves lead to the second generation wave models. The shortcomings of the first and second generation have been identified and discussed in detail in the SWAMP wave-model intercomparison study, initiating a new generation of WAM model [72]. However, it was until 1990s that the measurements of full two-dimensional spectrum have been obtained only at selected sites and for restricted time periods using large wave-staff arrays, or special remote sensing systems onboard aircraft such as Radar Ocean-Wave Spectrometer (ROWS), the surface contouring radar or stereophotography.

Since 1990s, global measurements of the two-dimensional wave spectrum became possible from space-born SAR flown on satellites ERS-1/2, Radarsat 1/2, shuttle missions and polar platforms. New missions of ocean wave investigations experienced the mapping of ocean wave spectrum from the SAR image spectrum [45], the unification of the directional spectrum [73], the effect of long waves and swell [74, 75, 76]. The bound wave / free wave model by Plant shows the consistency with sea surface slope spectrum measured in 1950s [77].

For full polarization radar imagery, it is possible to use the polarization synthesis technique to solve optimal polarization problems. Among polarization parameters, orientation angle is of special use for ocean remote sensing due to the so-called polarization modulation transfer function (MTF) [78], which was first introduced by Schuler in 1995. The polarization MTF is jointly driven by orientation angle and wave slope, i.e., at a special selected orientation angle, the modulation of the wave slope on radar measured intensity could be enhanced, better than any of that from the standard linear polarization  $HH$ ,  $VV$ ,  $HV$  or  $VH$ . This principle of this method had been discussed earlier by Boerner et al. [8].

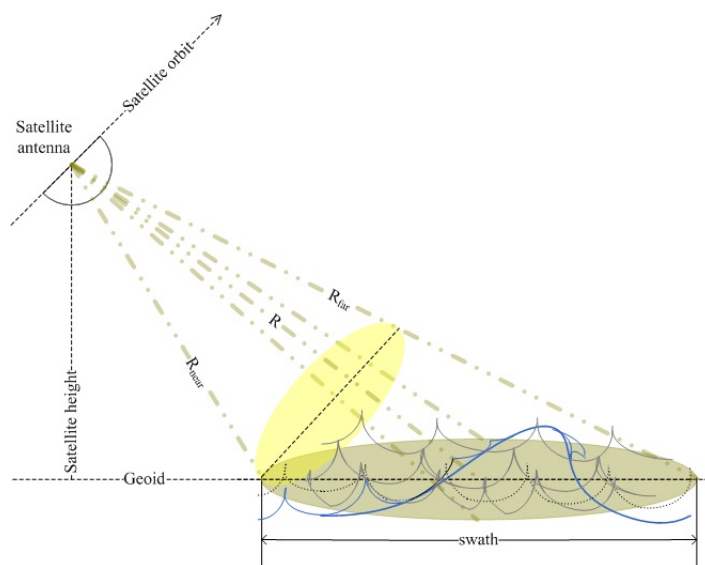


**Figure 2.8** — Right looking geometry of SAR imaging over the sea surface

A similar azimuth slope effect called orientation angle modulation proposed in [79] can further be combined with an eigenvector  $\alpha$  angle modulation which is more sensitive to incidence angle, resulting a 2-D slope modulation. This  $\alpha$  parameter was introduced in Cloude-Pottier entropy-anisotropy-  $\alpha$  polarization decomposition theorem [10]. It is roll-invariant in the azimuth direction with high sensitivity to wave-induced modulation on local incidence angle. Surface wave on azimuth and range direction can be accurately represented by the two polarization parameters, orientation and eigenvector  $\alpha$  angle, within each facet on the sea surface. In [80] a circular polarization algorithm was proposed. To make difference between this  $\alpha$  parameter with the polarization ratio  $\alpha$  in the former chapter, this  $\alpha$  parameter will be referred to as the  $\alpha$  angle while the former  $\alpha$  will be mentioned as  $\alpha$  ratio.

For the orientation angle and eigenvector alpha angle, an average over image pixels should be performed. This helps to better cope with the reflection asymmetry condition which is the base of the circular polarization method of orientation shift calculation [80].

On the estimation of the orientation angle, a method based on the circular polarization rotation property with the reflection asymmetry model was proposed in [81, 80], which has more computational efficiency and accuracy than the polarization signature method which gives an direct presentation of the orientation angle shift, denoting a shift from the maximum co-polarization response induced by the azimuth slope of the imaging area (especially a distributed media) [1].

Polarimetry approaches has been investigated for RADARSAT-2 SAR imagery [68, 82], but different from the development by [79]. Here we recall the circular polarization method,

which was recommended in [81, 80] as

$$\phi = \begin{cases} \eta, & \text{if } \eta \leq \pi/4 \\ \eta - \pi/2, & \text{if } \eta > \pi/4 \end{cases} \quad (2.5)$$

where

$$\eta = \frac{1}{4} \left[ \tan^{-1} \left( \frac{-4\Re \left( \langle (\tilde{S}_{HH} - \tilde{S}_{VV}) \tilde{S}_{HV}^* \rangle \right)}{-\langle |\tilde{S}_{HH} - \tilde{S}_{VV}|^2 \rangle + 4\langle |\tilde{S}_{HV}|^2 \rangle} \right) + \pi \right] \quad (2.6)$$

which equals to

$$\phi = \frac{1}{4} \left[ \tan^{-1} \left( \frac{-4\Re \left( \langle (\tilde{S}_{HH} - \tilde{S}_{VV}) \tilde{S}_{HV}^* \rangle \right)}{-\langle |\tilde{S}_{HH} - \tilde{S}_{VV}|^2 \rangle + 4\langle |\tilde{S}_{HV}|^2 \rangle} \right) \pm \pi \right] \quad (2.7)$$

where the plus sign for the minus arctangent while minus sign for the plus arctangent, i.e.,

$$4\phi \in \left( -\frac{3\pi}{2}, -\frac{\pi}{2} \right) \cup \left[ \frac{\pi}{2}, \frac{3\pi}{2} \right)$$

The shift of orientation angle in the polarization signature is related to the azimuth surface slope, the radar look angle, and the range slope [83, 84],

$$\tan \phi = \frac{\tan \omega}{\sin \theta - \tan \gamma \cos \theta} \quad (2.8)$$

where  $\phi$ ,  $\tan \omega$ ,  $\theta$  and  $\tan \gamma$  are orientation angle, azimuthal slope, radar look angle and the range slopes. This relationship also imply that orientation shift could be taken as an effect from surface slopes in both azimuth and range directions.

The direct measurements of surface slopes were firstly used and valid on the topographic [85]. But considering about the sea surface [79], there is still a difficulty of non-linear velocity bunching introduced by the radial component of the orbital velocity of the surface wave [86]. For sea surface application, this technique was limited within the condition when the range-to-velocity (R/V) is quite small so that the azimuth smearing item  $\Delta a = -u_R(x_0)R/V_{st}$  (equation [18] in [86]) will not introduce ambiguity when mapping the wave coordinate  $x_0$  into SAR image coordinate. Generally this problem is more significant for space borne SAR than for air-borne SAR conditions, with the latter has a smaller R/V (which is normally less than 100s).

Keeping in mind of the orbital motion of water molecule in figure 2.7, the radial component (along the direction of LOS) achieves its maxima around the wave peak, and the larger the incidence angle, the nearer of this position to the wave peak. Based on this modelling, we suppose that the velocity bunching effect dominates the scalar part while seldom appears on the tilt Bragg part, so the limitation from velocity bunching on the Bragg wave spectra retrieval will not be the problem in the following.

According to target decomposition (TD) theorem, a target has a scattering matrix only when it is a single scatter, i.e., the coherency matrix  $T_3$  has only one non-zero eigenvalue. When there are more non-zero eigenvalues, a mean scattering matrix could be used to represent the primary scattering mechanism inside one facet. This mean scattering matrix has an eigenvector as [1]

$$k = \sqrt{\lambda} e^{j\varphi} \begin{bmatrix} \cos \alpha \\ \sin \alpha \cos \beta e^{j\delta} \\ \sin \alpha \sin \beta e^{j\gamma} \end{bmatrix} \quad (2.9)$$

in which  $\lambda$ ,  $\alpha$  are roll-invariant roll-invariant mean scattering and the mean target power (span) separately respectively, identifying the dominant scattering mechanism and the rest three parameters  $\beta$ ,  $\delta$ ,  $\gamma$  are orientation angle related, they are rotation variant and used to define the target polarization orientation angle. The  $\lambda = \sum_{k=1}^3 p_k \lambda_k$ , where  $p_k$  is the eigenvalue pseudo probability,

$$p_k = \frac{\lambda_k}{\sum_{i=1}^3 \lambda_i}$$

The five parameters connect with radar measurements by

$$T_3 = k_p \cdot k_p^{*T} = k \cdot k^{*T} \quad (2.10)$$

in which the '3-D Pauli feature vector' [1]

$$k_p = \begin{bmatrix} S_{VV} + S_{HH} \\ S_{VV} - S_{HH} \\ S_{HV} + S_{VH} \end{bmatrix}. \quad (2.11)$$

and  $S_{pq}$ ,  $p, q \in \{H, V\}$  is the components of Sinclair scattering matrix.

For the ocean surface of the pixel size of SAR measurement, the averaged slopes are small as the onset of wave breaking occurs at about  $7^\circ$ . The approximation made from 2.9 and 2.11 yields

$$\tan \alpha \approx \frac{S_{VV} - S_{HH}}{S_{VV} + S_{HH}} \quad (2.12)$$

Using the SMP model and considering only incidence angle, for the water dielectric constant  $\epsilon \rightarrow \infty$ , the relationship between  $\alpha$  angle and incidence angle  $\theta_i$  is

$$\tan \alpha = \sin^2 \theta_i, \quad (2.13)$$

as shown in figure 10.21 in [1]. Range slopes can be derived from the local incidence angle corresponding to  $\alpha$  angle subtracted by the incidence angle according to the radar geometry.

So far, using Bragg theory a model can be derived for sea surface slopes by the circular polarization transformation for orientation angle and by eigenvector alpha angle as

$$\begin{aligned} \gamma &= \theta_i - \theta \\ \tan \omega &= \tan \phi (\sin \theta - \tan \gamma \cos \theta) \end{aligned} \quad (2.14)$$

where  $\sin^2 \theta_i = \tan \alpha$  and

$$\tan(2\phi) = \frac{2\tilde{S}_{HV}}{\tilde{S}_{VV} - \tilde{S}_{HH}}, \tan(\alpha) = \frac{\tilde{S}_{VV} - \tilde{S}_{HH}}{\tilde{S}_{VV} + \tilde{S}_{HH}} \quad (2.15)$$

in which  $\tilde{S}_{HV}$ ,  $\tilde{S}_{VV}$ ,  $\tilde{S}_{HH}$  are Bragg scattering estimates due to the small roughness elements modulated by the longer waves.

### 2.2.2 Simple model as polarization difference

Valenzuela [16] investigated sea surface depolarization following Rice's method for slightly rough surface, indicated that polarization ratio of VV over HH is independent of the wave spectrum of the surface while increase with the absolute magnitude of the complex dielectric constant of the scattering surface, e.g. for dielectric constant as high as sea water, the polarization ratio could increase from 0 at 0 incidence angle to 10 dB at 50 deg. of incidence angle. Also in [16] the depolarized power for backscattering in both polarizations were given as the second-order fields effect.

For the case of radar remote sensing of distributed sea surface, the polarization ratio (PR) defined in [22, 18] as the ratio of the normalized radar cross-section (NRCS) in VV over HH expressed in a linear scale, wherein PR is presented in dB,

$$PR = \frac{NRCS_{VV}}{NRCS_{HH}}$$

The Normalized radar cross-section (NRCS) has a statistical definition as

$$NRCS_{pq} = \frac{RCS_{pq}}{RCS_{pq-max-whole}} \quad (2.16)$$

where  $RCS_{pq} \equiv \langle |S_{pq}|^2 \rangle - |\langle S_{pq} \rangle|^2$ . By analysing the NRCS and its approximation, the sea surface was characterised with the average level of radar backscatters. Polarization ratio models considering only incidence angle, such as M2 [22] and Z2 [87] fits separately part of the satellite data, as shown in figure 2.12 (a). On the comparison with the model considering wind direction (M1) [22], an overestimation happens when the incident angle is higher than 40°. Also the recent experimental model Z1 [87] depending on wind speed overestimates for the high incidence angle and high wind speed. Differences arise from the high incidence angle and high winds, wherein the polarization independent scattering from the sea surface dominants the radar backscatter.

However, the discrepancy between the SAR measurement NRCS and the two-scale model indicates a third kind of scattering mechanism may be invoked, which was supposed to come from breaking waves [23, 88]. According to the laboratory observation showing the polarization ratio of the co-polarization backscattering coefficients is around unit [47], we suggest to

consider this third type of scattering as a scalar (non-polarized) contribution attributed to wave breaking effects through specular reflection on surface patches [18, 23]. Based on this understanding, the direct radar measurements could be write as

$$\begin{aligned}
NRC S_{HH} &= scalar_{Co.pol} + TiltBragg_{hh} \\
NRC S_{VV} &= scalar_{Co.pol} + TiltBragg_{vv} \\
NRC S_{HV} &= scalar_{X.pol} + TiltBragg_{hv} \\
NRC S_{VH} &= scalar_{X.pol} + TiltBragg_{vh}
\end{aligned} \tag{2.17}$$

where  $scalar_{r.pol}$  ( $r = \{Co, X\}$ ) denotes the third kind of scattering mechanism (we group them into one third kind for simplicity although may be due to different types of scatterers),  $TiltBragg_{pq}$  ( $p, q = \{h, v\}$ ) corresponds to the tilt Bragg model. From this separation, tilt Bragg should be the only contributor to polarization difference, for the assumption of the same  $scalar_{Co.pol}$  for both HH and VV polarization. This could explain the overestimation of PR models for the high winds and high incidence angles in [22] and [87]. It is straightforward that from the separation (2.17) if we know the relationship between  $TiltBragg_{hh}$  and  $TiltBragg_{vv}$ , the scalar contribution will be estimated directly from radar measurements, and is also clear that if we could split the scalar contribution from the SAR measurement, the discrepancy of the SAR measured PR should change. At this point, the ratio of  $TiltBragg_{vv}$  over  $TiltBragg_{hh}$  would not be PR any more, so the ratio  $\alpha$  is defined as

$$\alpha \equiv \frac{TiltBragg_{vv}}{TiltBragg_{hh}} \tag{2.18}$$

and the PR could be estimated as

$$PR = \frac{NRC S_{VV}}{NRC S_{HH}} = \frac{scalar_{Co.pol} + \alpha TiltBragg_{hh}}{scalar_{Co.pol} + TiltBragg_{hh}}. \tag{2.19}$$

To implement this simple model, we simplify the scattering matrix decomposition as Bragg scattering and cylinder-like contributions, as for figure ??, but here the Bragg scattering matrix will replace the dipole matrix,

$$S = \sum a_i S_{bri} + \sum s_j \begin{bmatrix} \cos 2\phi_{scj} & \sin 2\phi_{scj} \\ \sin 2\phi_{scj} & -\cos 2\phi_{scj} \end{bmatrix} + S_{residual} \tag{2.20}$$

where  $a_i S_{bri}$  are Bragg scattering matrices, and  $s_j$ ,  $\phi_{scj}$  are complex scattering coefficients and orientation angles of cylinder-like scatterers.

We know the Bragg scattering matrix as in equation 2.3. Considering depolarization, the tilt effect will be expressed by an orientation angle, under the 'con-similarity transformation' [1],

$$S_{tilt\_bragg} = U_2(\phi)^T S_{bragg} U_2(\phi) \tag{2.21}$$

where

$$U_2(\phi) = \begin{bmatrix} \cos \phi & -\sin \phi \\ \sin \phi & \cos \phi \end{bmatrix} \quad (2.22)$$

with  $\phi$  the orientation angle and  $S_{bragg}$  the one in equation 2.3, which arrives at

$$\begin{aligned} S_{tilt.bragg} &= \begin{bmatrix} S_{tilt.HH} & S_{tilt.HV} \\ S_{tilt.VH} & S_{tilt.VV} \end{bmatrix} \\ &= m_s \begin{bmatrix} R_S(\theta, \epsilon) \cos^2 \phi + R_P(\theta, \epsilon) \sin^2 \phi & (R_P(\theta, \epsilon) - R_S(\theta, \epsilon)) \frac{\sin 2\phi}{2} \\ (R_P(\theta, \epsilon) - R_S(\theta, \epsilon)) \frac{\sin 2\phi}{2} & R_S(\theta, \epsilon) \sin^2 \phi + R_P(\theta, \epsilon) \cos^2 \phi \end{bmatrix} \end{aligned} \quad (2.23)$$

where  $m_s$  is still the backscatter amplitude containing the information about the roughness condition of the surface,  $R_S$  and  $R_P$  are the Bragg scattering coefficients perpendicular and parallel to the incidence plane respectively, and functions of the complex permittivity  $\epsilon$  of the ferromagnetic media and the local incidence angle  $\theta$ ,

$$R_S = \frac{\cos \theta - \sqrt{\epsilon - \sin^2 \theta}}{\cos \theta + \sqrt{\epsilon - \sin^2 \theta}}, \quad R_P = \frac{(\epsilon - 1)(\sin^2 \theta - \epsilon(1 + \sin^2 \theta))}{(\epsilon \cos \theta + \sqrt{\epsilon - \sin^2 \theta})^2} \quad (2.24)$$

Transform into HH and VV convention we used before, orientated Bragg scattering matrix could be written into equation 2.20,

$$\begin{aligned} S &= \sum b_i \begin{bmatrix} R_h(\theta, \epsilon) \cos^2 \phi_{bri} + R_v(\theta, \epsilon) \sin^2 \phi_{bri} & (R_v(\theta, \epsilon) - R_h(\theta, \epsilon)) \frac{\sin 2\phi_{bri}}{2} \\ (R_v(\theta, \epsilon) - R_h(\theta, \epsilon)) \frac{\sin 2\phi_{bri}}{2} & R_h(\theta, \epsilon) \sin^2 \phi_{bri} + R_v(\theta, \epsilon) \cos^2 \phi_{bri} \end{bmatrix} \\ &\quad + \sum s_j \begin{bmatrix} \cos 2\phi_{scj} & \sin 2\phi_{scj} \\ \sin 2\phi_{scj} & -\cos 2\phi_{scj} \end{bmatrix} + S_{residual} \end{aligned} \quad (2.25)$$

in which  $b_i = a_i m_s$ . To be analogue with definition 2.18, a ratio of Bragg scattering coefficients  $R_v$  over  $R_h$  could simplify Equation 2.25,

$$\begin{aligned} S &= \sum b_i R_h(\theta, \epsilon) \begin{bmatrix} \cos^2 \phi_{bri} + \beta \sin^2 \phi_{bri} & (\beta - 1) \frac{\sin 2\phi_{bri}}{2} \\ (\beta - 1) \frac{\sin 2\phi_{bri}}{2} & \sin^2 \phi_{bri} + \beta \cos^2 \phi_{bri} \end{bmatrix} \\ &\quad + \sum s_j \begin{bmatrix} \cos 2\phi_{scj} & \sin 2\phi_{scj} \\ \sin 2\phi_{scj} & -\cos 2\phi_{scj} \end{bmatrix} + S_{residual} \end{aligned} \quad (2.26)$$

where the ratio of Bragg scattering coefficients

$$\beta = \frac{R_v}{R_h} = \frac{(\epsilon - 1)(\sin^2 \theta - \epsilon(1 + \sin^2 \theta))(\cos \theta + \sqrt{\epsilon - \sin^2 \theta})}{(\cos \theta - \sqrt{\epsilon - \sin^2 \theta})(\epsilon \cos \theta + \sqrt{\epsilon - \sin^2 \theta})^2}. \quad (2.27)$$

One should be note is that the second-order SPM depolarization is not yet considered, hence so far, the only source being considered for depolarization is the tilt effect. Before the implementation, explanations to several assumptions should be given to simplify the complexity.

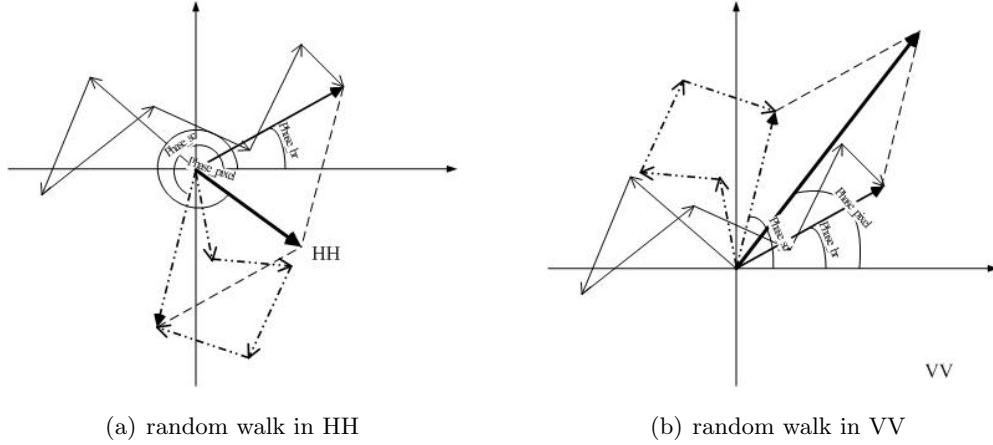


**Figure 2.9** — Random walk of Bragg vs scalar, co-pol. Solid line represents the random walk of Bragg scattering and the vector sum has a phase bragg, dashed line represents the random walk of Scalar scattering and result in the vector sum with a phase scalar, and the radar measurements (HH and VV) is the vector sum of Bragg vector and Scalar vector, with a phase of phase pixel.

### 1. Phase

Looking into the scattering mechanisms within pixel cell area, the interaction of quite a number of isolated scatterers could be modelled by random walk [89]. At microwave wavelengths, a rough surface is concerned about the wavelength larger than  $\frac{1}{4}$  of the Bragg wave, according to the Rayleigh criterion (which we talked about this in details in Chapter 3), meaning a mean quadratic phase shift higher than  $\pi/2$ . For a rough surface, the distances between the elementary scatterers and the radar receiver vary due to the random location of scatterers. Since phase relates only to the distance between the target and the receiver, the received waves from each scatter, although coherent in frequency, are no longer coherent in phase [1]. At this point of view, in our simple scattering model, the Bragg contribution is the result of random walk of Bragg resonances and the scalar contribution is the result of random walk of scalars, as shown in figure 2.9(a) and 2.9(b). We are not going to concern each of the isolated scatterers at this stage, that is to say, since the backscattered signals from both Bragg-like and scalar-like scatters could be modelled as random walk, as shown in figure 2.9(a) and 2.9(b), the Bragg-like contributions could be taken as a whole by end-to-end sum, and the same for the scalar-like contributions, leaving

$$S = B \begin{bmatrix} \cos^2 \phi_{br} + \beta \sin^2 \phi_{br} & (\beta - 1) \frac{\sin 2\phi_{br}}{2} \\ (\beta - 1) \frac{\sin 2\phi_{br}}{2} & \sin^2 \phi_{br} + \beta \cos^2 \phi_{br} \end{bmatrix} + S_a \begin{bmatrix} \cos 2\phi_{sc} & \sin 2\phi_{sc} \\ \sin 2\phi_{sc} & -\cos 2\phi_{sc} \end{bmatrix} + S_{residual} \quad (2.28)$$

where  $B$ ,  $\phi_{br}$  and  $S_a$ ,  $\phi_{sc}$  are complex scattering coefficient and orientation angle from

whole dipole-like scatters and whole cylinder-like scatterers. On this assumption,  $B$ ,  $\phi_{br}$  and  $S_a$ ,  $\phi_{sc}$  are the ene-to-end sum over the pixel cell surface area. The difference between figure 2.9(a) and 2.9(b) comes from the difference of  $\pi$  in the phase of horizontal co-pol and vertical co-pol in the cylinder-like scatter matrix, the second terms on the right of equation 2.25.

## 2. Orientation angle

In Equation 2.28,  $\phi_{br}$  and  $\phi_{sc}$  are mean orientation angles for the Bragg-like scatterers and cylinder-like scatterers inside the pixel surface area. The orientation angle  $\phi$  relates with the azimuthal slope and range slope as well as incidence angle by [84, 83]

$$\tan \phi = \frac{\tan \omega}{\sin \theta - \tan \gamma \cos \theta} \quad (2.29)$$

where  $\phi$ ,  $\tan \omega$ ,  $\theta$  and  $\tan \gamma$  are orientation angle, azimuthal slope, radar look angle and the range slopes. Investigations shows that for the ocean surface at scales  $6.6 \times 8.2m$ , the averaged tilt angles are small, and the onset of wave breaking occurs at about 7 deg [79]. Thus the orientation angle could be assumed to be related only with azimuthal slope and radar look angle. Based on this knowledge, the assumption of  $\phi_{br} = \phi_{sc}$  could be established.

## 3. Residual

The residual scattering matrix exists because the phase difference between radar received co-pol and X-pol signals and even between X-pol signals, i.e. HV and VH. That's the indication to the existence of helix-like scatterers inside the pixel cell surface area. On this point, we improve equation 2.25 as

$$S_{residual} = CS_{righthelix} + DS_{lefthelix} \quad (2.30)$$

where  $C$  and  $D$  are end-to-end sums of complex scattering coefficients from total right helix-scatters and left helix-like scatterers, for which the scattering matrix satisfying

$$S_{righthelix} = \begin{bmatrix} \cos 2\phi_{rhelix} - i \sin 2\phi_{rhelix} & -\sin 2\phi_{rhelix} - i \cos 2\phi_{rhelix} \\ -\sin 2\phi_{rhelix} - i \cos 2\phi_{rhelix} & -\cos 2\phi_{rhelix} + i \sin 2\phi_{rhelix} \end{bmatrix}$$

and

$$S_{lefthelix} = \begin{bmatrix} \cos 2\phi_{lhelix} - i \sin 2\phi_{lhelix} & \sin 2\phi_{lhelix} + i \cos 2\phi_{lhelix} \\ \sin 2\phi_{lhelix} + i \cos 2\phi_{lhelix} & -\cos 2\phi_{lhelix} + i \sin 2\phi_{lhelix} \end{bmatrix},$$

with  $\phi_{rhelix}$  and  $\phi_{lhelix}$  the average level of orientation angles for total right helix-scatters and left helix-like scatterers, and for simplicity with confidence, the assumption of  $\phi_{rhelix} = \phi_{lhelix} = \phi_{br} = \phi_{sc}$  could be established. One should be noticed is the helix-like scattering contributes equal intensities to different polarization channels, thus to be

taken as scalar. Another one should be noticed is although helix scatter introduce the asymmetric but not non-reciprocal yet. Here we refer to the explanation in [52], saying if reciprocity is violated it is likely to be due to propagation effects, interaction with special materials or for low RCS returns, perhaps measurement noise. On this two notices, the residual components has no help to explain the inter X-pol difference and should be considered as a part of scalar.

Based on above assumptions, We rewrite equation 2.20 straightforwardly as

$$S = B \begin{bmatrix} \cos^2 \phi + \beta \sin^2 \phi & (\beta - 1) \frac{\sin 2\phi}{2} \\ (\beta - 1) \frac{\sin 2\phi}{2} & \sin^2 \phi + \beta \cos^2 \phi \end{bmatrix} + S_a \begin{bmatrix} \cos 2\phi & \sin 2\phi \\ \sin 2\phi & -\cos 2\phi \end{bmatrix} \quad (2.31)$$

So far, there are 6 equations (in the following equation 2.32) for 6 unknown variables, i.e. complex scattering coefficients  $B$ ,  $S_a$ , and one orientation angle  $\phi$  and polarization ratio  $\beta$ .

$$\begin{aligned} \Re(B)(\cos^2 \phi + \beta \sin^2 \phi) + \Re(S) \cos 2\phi &= \Re(S_{HH}) \\ \Im(B)(\cos^2 \phi + \beta \sin^2 \phi) + \Im(S) \cos 2\phi &= \Im(S_{HH}) \\ \Re(B)(\sin^2 \phi + \beta \cos^2 \phi) - \Re(S) \cos 2\phi &= \Re(S_{VV}) \\ \Im(B)(\sin^2 \phi + \beta \cos^2 \phi) - \Im(S) \cos 2\phi &= \Im(S_{VV}) \\ \Re(B)(\beta - 1) \frac{\sin 2\phi}{2} + \Re(S) \sin 2\phi &= \Re(S_{HV}) \\ \Im(B)(\beta - 1) \frac{\sin 2\phi}{2} + \Im(S) \sin 2\phi &= \Im(S_{HV}) \end{aligned} \quad (2.32)$$

This decomposition were implemented on Radarsat-2 (R2) C-band data, and the preliminary results are discussed here, leading to improvements in the following chapters. Since in Equation 2.32 there are 6 unknowns in 6 equations, the first step is to estimate  $\beta$  with radar look angle instead of local incidence angle, shown in the flowchart of Figure 2.10 where the iteration flow chart goes for the first iteration. Based on the first estimated Bragg components ( $Bragg_{hh}$ ,  $Bragg_{vv}$ ,  $Bragg_{hv}$ , and  $Bragg_{vh}$ ), the local incidence angle could be estimated by the relationship of  $Bragg_{hh}$  and  $Bragg_{vv}$ , as introduced by Cloude-Pottier entropy-anisotropy-  $\alpha$  polarization decomposition theorem, in Equation 2.13 and 2.15. 18 scenes of full polarization involved here, as shown in Table 2.1, processed as slant range product with a complex data type, i.e., SLC, for which the pixel spacing is determined by the radar range sampling rate and pulse repetition frequency (PRF), and the single look processing made use of full available signal bandwidth, reaching at a fine spatial resolution.

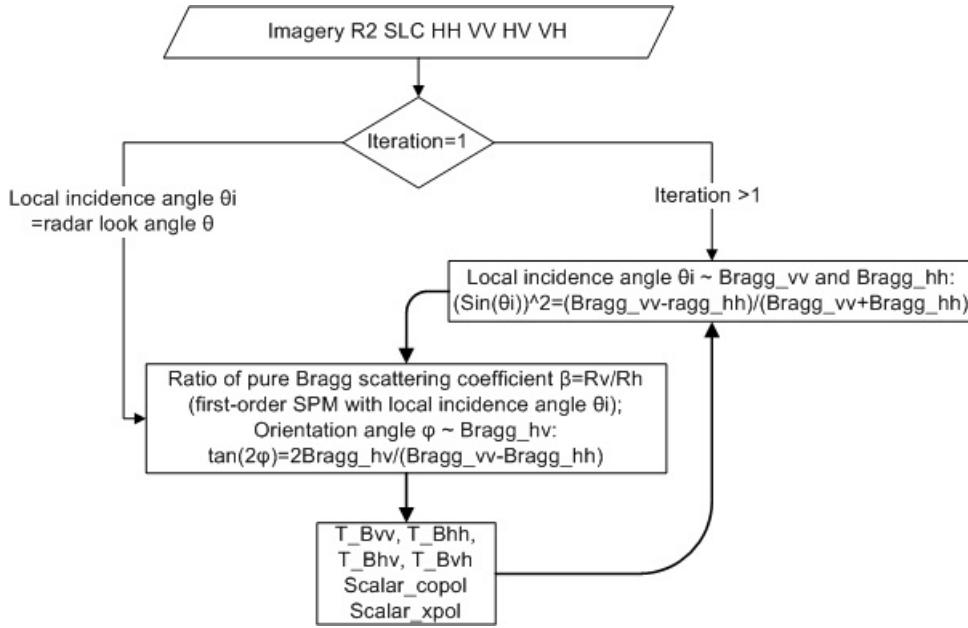


Figure 2.10 — Iteration flow chart

## 2.3 Preliminary result and discussion

### 2.3.1 Wind and wave data

In-situ platforms collocated with R2 satellite data set are offered by the Observing System Monitoring Center (OSMC) programme funded by NOAA/OCO, providing both the near real and historical status of globally distributed meteorological and oceanographic data collection systems. These platforms include both buoys and voluntary ships, returning one record per hour, generally. The nearest records were interpolated in time for satellite data acquired in August and September, and latter records come from meteorological moored buoys located exactly in the satellite image scene, as shown in table 2.1. Sea states ranges from smooth wavelets, according to Douglas sea scale (see table 2.2), to very rough sea surface, even high sea state with a wave height as high as 7m.

Considering wind streaks, wind changes will induce changes of radar cross section, and shall help to evaluate the relative sensitivity of VV, HH, and HV (or VH) polarization composition to wind parameter. This will help to assess which channel is best to retrieve wind speed around a relatively high wind condition. Considering the detected waves, the cut-off wavelength for VV, HH, HV, VV-HH and  $VV \cdot \text{conj}(HH)$  polarization compositions have been analysed. This should help to assess the proper polarization ratio  $\alpha$  (defined former in Equation 2.18) of tilt Bragg VV over HH which separates the polarization part (the tilt Bragg scatter) from the polarization independent part, i.e., the scalar contributions, as denoted in

*Table 2.1* — OSMC Wind and Wave

satellite acquisition	incidence angle (center)	wind spd m/s	wind dir deg.	wave height m.
(0)20110803	40.90	1.65	121.13	0.70
(1)20110809	45.92	15.00	320.00	3.40
(2)20110810	45.89	14.38	300.00	2.98
(3)20110812	36.27	5.95	50.47	1.20
(4)20110819	40.92	7.00	320.00	0.40
(5)20110820	36.25	4.22	11.95	0.20
(6)20110904	19.38	14.92	270.00	2.10
(7)20110907	19.38	8.42	284.00	1.52
(8)20111203	45.09	12.40	240.00	2.06
(9)20111205	45.11	10.29	290.00	4.50
(10)20120329	29.32	11.84	320.00	2.95
(11)20120405	25.91	9.60	356.67	2.05
(12)20120406	32.56	9.78	40.00	2.70
(13)20120408	28.20	7.95	230.00	1.20
(14)20120409	30.42	4.76	282.50	3.05
(15)20120416	33.60	10.19	260.00	1.74
(16)20120423	27.06	17.50	309.00	7.51
(17)20120509	24.35	2.85	335.00	1.00

*Table 2.2* — Douglas sea state

Douglas sea state	Description	Wave height (SWH ft)	Wind speed (kn)	Fetch (nmi)	Duration (h)
1	Smooth	0-1	0-6		
2	Slight	1-3	6-12	50	5
3	Moderate	3-5	12-15	120	20
4	Rough	5-8	15-20	150	23
5	Very rough	8-12	20-25	200	25
6	High	12-20	25-30	300	27
7	Very high	20-40	30-50	500	30
8	Precipitous	> 40	> 50	700	35

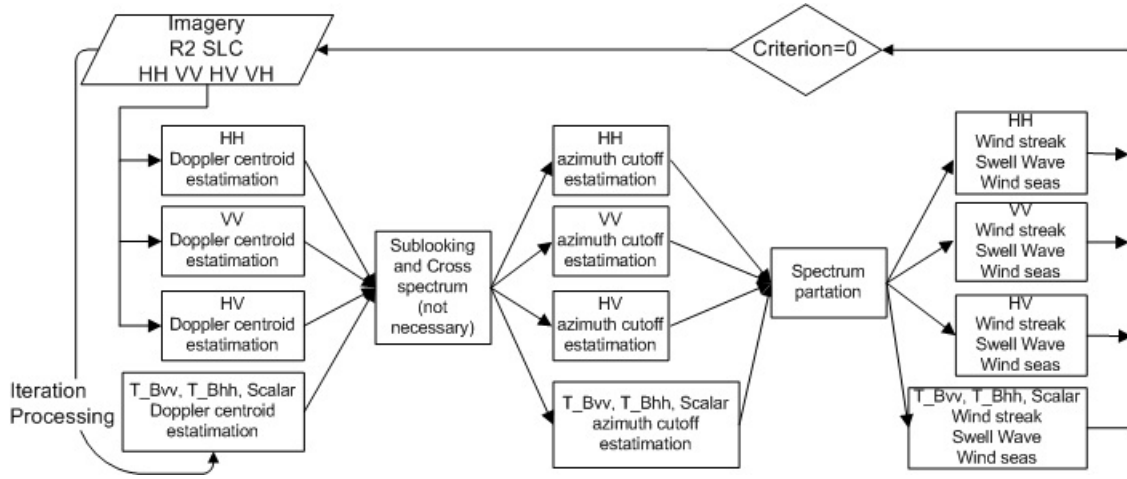


Figure 2.11 — Validation flow chart

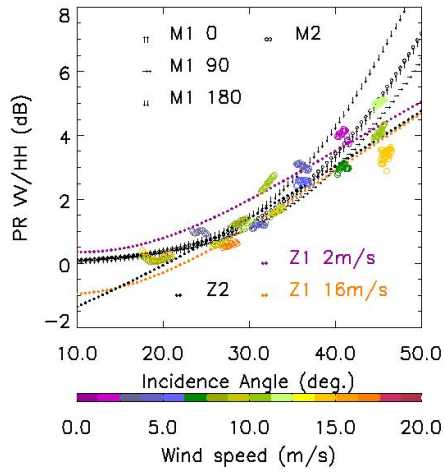
the simple model in Section 2.2.2. This part of work will be introduced in spectral analysis section as the validation as well as to find the criterion for ceasing the iteration processing of Figure 2.10. The validation flow chart is shown in Figure 2.11.

For the 'zeroth' iteration, we took polarization ratio (imagery NRCS VV over HH) according to the cross-polarizaion HV with wind reference, shown in Figure 2.12. Figure 2.12 (b) (c) and (d) show the correlation between PR and HV, in which colors are according to incidence angle, wind speed and direction separately. It is clear from (b) that incidence angle classifies the PR-HV tuple, i.e., HV represents wind information as well as PR. An evidence in the following plots of (c) and (d) expresses well the dependence on wind speed and direction of HV.

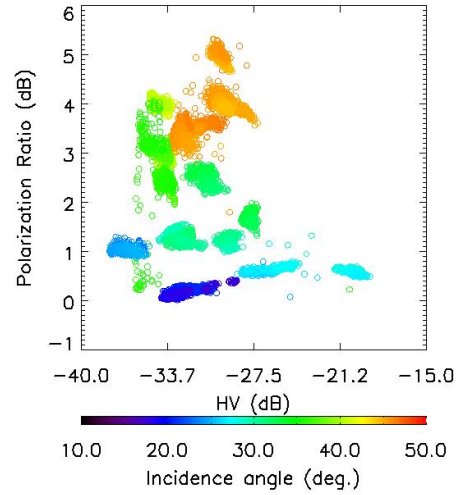
By decomposing the scattering matrix into tilt Bragg and scalar, for the first iteration, i.e. without consideration of local incidence angle introduced by surface slope on range direction, it is possible to find the polarization ratio  $\alpha$  of tilt Bragg NRCS in VV polarization over HH polarization, as in Figure 2.13 (a). From the second iteration and then on (Figure 2.13), the local incidence angle introduced by surface slope on range direction could be estimated from 'Bragg model', as shown in the flow chart Figure 2.10 where the iteration goes into the circulant to the right.

### 2.3.2 Doppler analysis

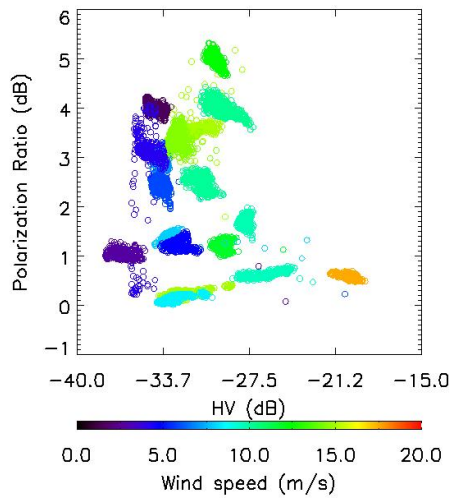
SAR instruments are essentially sensitive to Doppler effects. Due to the 'velocity bunching' formation (equation (8) in [86]), a larger radial velocity where  $\frac{R}{V} \frac{du_r}{dx} \geq 1$  leading to a larger displacement  $\xi$  in azimuth direction, leaving the backscattered signals with same range distance unresolvable (smearing) within this displacement. This displacement was found to



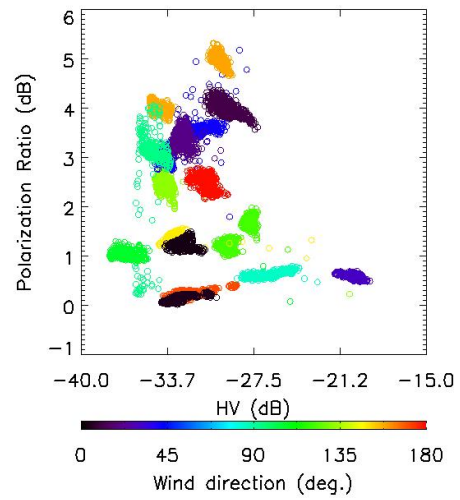
(a) PR vs. models



(b) PR vs. HV,  
colored by incidence angle

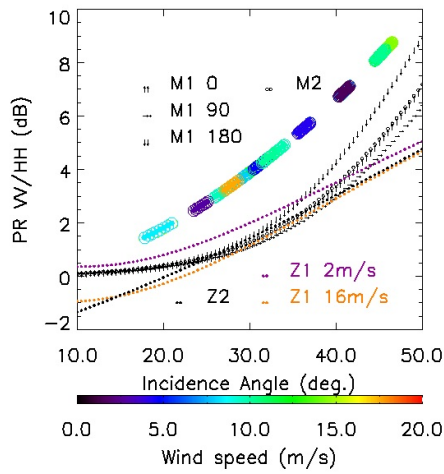


(c) PR vs. HV,  
colored by wind speed in situ

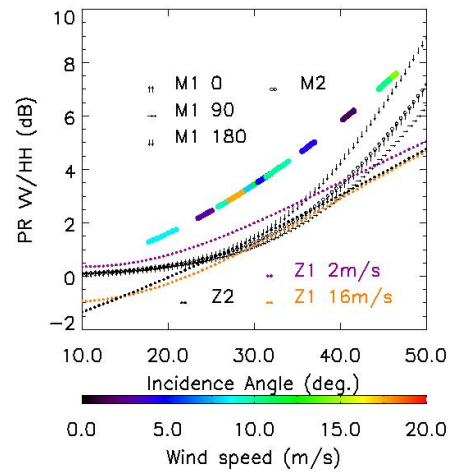


(d) PR vs. HV,  
colored by wind dir. in situ

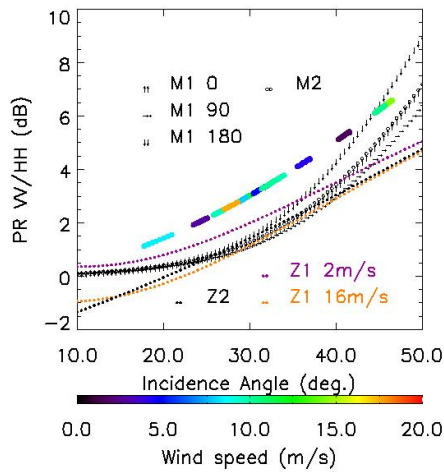
Figure 2.12 — Polarization ratio and depolarization HV.



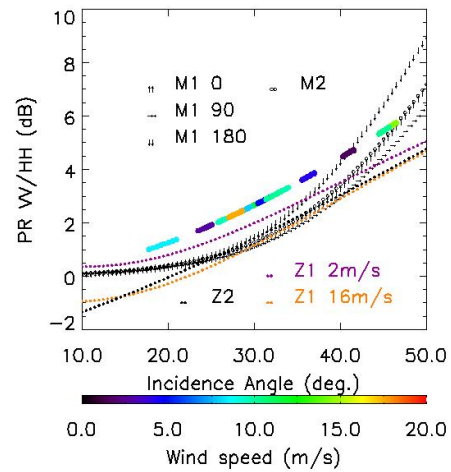
(a) Tilt Bragg PR, Iteration1



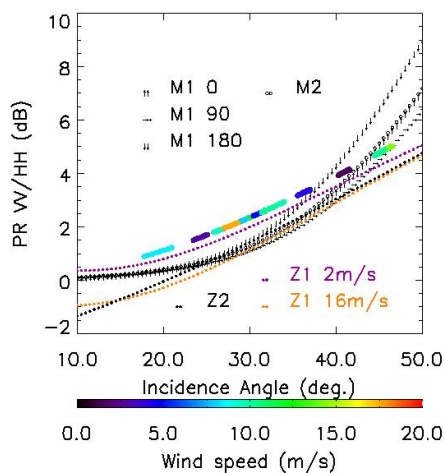
(b) Tilt Bragg PR, Iteration2



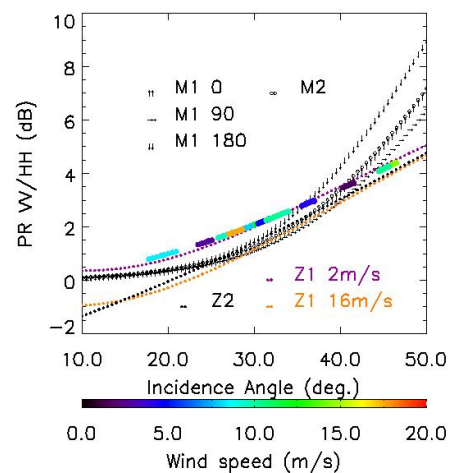
(c) Tilt Bragg PR, Iteration3



(d) Tilt Bragg PR, Iteration4



(e) Tilt Bragg PR, Iteration5



(f) Tilt Bragg PR, Iteration6

Figure 2.13 — Polarization ratio of Tilt Bragg. (Iteration 1,2,3,4,5,6)

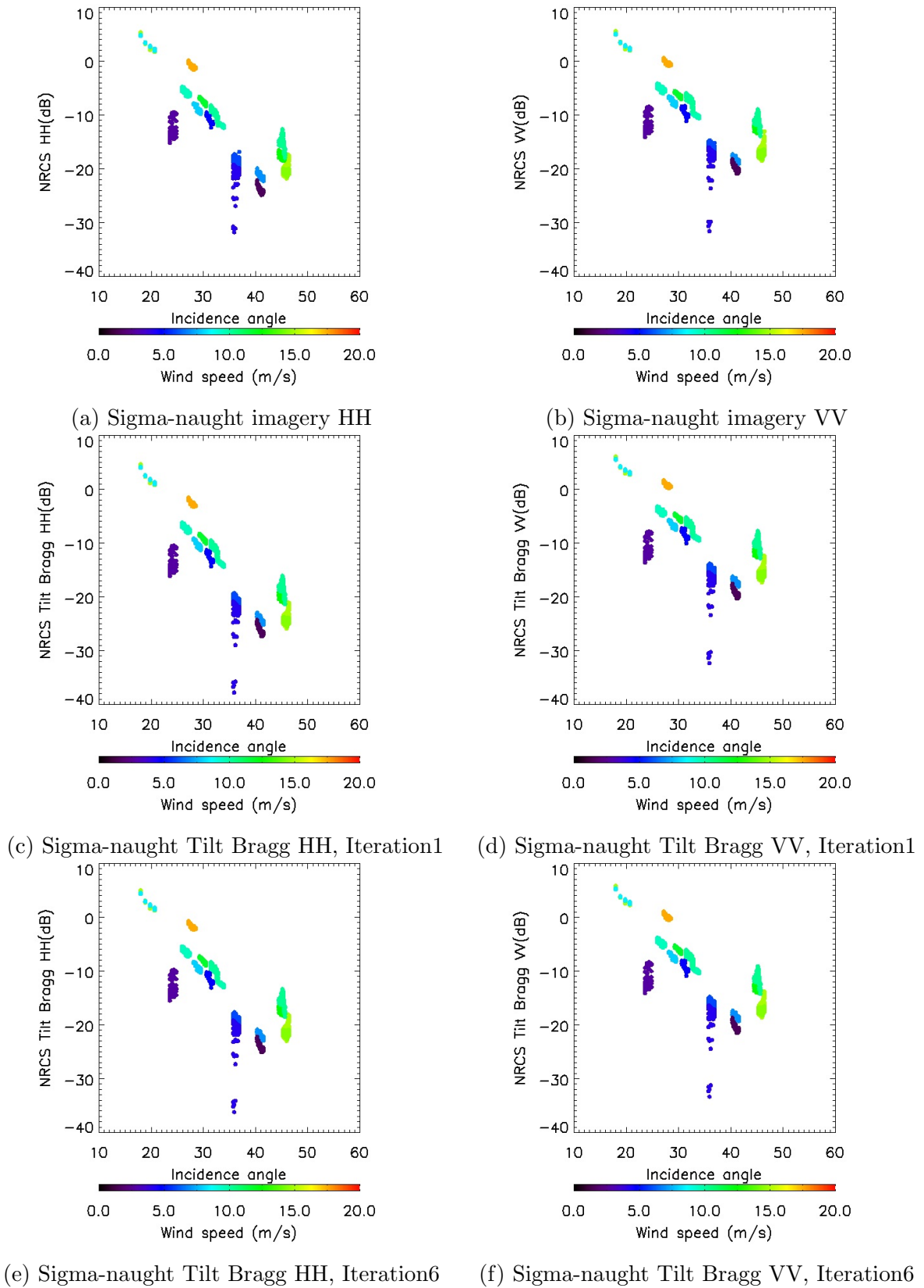


Figure 2.14 — Sigma-naught of co-pol . (Iteration 0,1,6)

function as the azimuthal cut-off factor with a Gaussian shape of  $\exp(-k_x^2 \xi'^2)$ , which represents the linear SAR spectrum into a quasi linear approximation [45]. Kerbaol et al. analysed ERS-1/2 wave mode imagerettes to find the relationship between azimuth cut-off and wind speed [90]. For ERS 1/2 wave mode, the operation incident angle of  $19.9^\circ$  and  $23.5^\circ$  relies the radial component to the vertical velocity which is mainly supported by the gravity waves.

The non-linear also produce significant shift of the spectral peak and other distortions of the spectrum [45], by which the analysis of the Doppler spectrum allows us to produce maps of sea surface velocity [91]. Chapron et al. for the first time systematically extracted global Doppler measurements for the range velocity. From a theoretical analysis and co-located atmospheric wind and wave model predictions, these Doppler shifts are shown to carry valuable quantitative information about the expected mean motion between the sea scatters and the satellite platform, i.e., the radial velocity [3].

This technique of using Doppler difference to measure surface currents was firstly established by an airborne two-antenna system [92], in which the two antennas are assumed to be collinear with the radar motion and the time lag for the same surface scatter passing by the two antennas' boresights should be chosen long enough to obtain measurable phase differences while shorter than the decorrelation time of the backscattered field [93]. With a very stable satellite orbit and attitude, a similar residual Doppler shift could be achieved by subtracting an accurately estimated satellite motion contribution  $f_{Dcm}$  from the measured Doppler centroid  $f_{Dc}$  [3, 91], at this point of view, without the two-antenna system.

### 2.3.2.1 Azimuthal Doppler centroid and wind sea

RADARSAT-2 SAR product files specify the Doppler centroid predicted from satellite orbit parameters. Due to the relative spacecraft-to-earth rotation rate expressed in equation (5) of [94], the Doppler centroid prediction ( $f_{Dcm}$ ) has a positive sign for an ascending pass and a negative sign for a descending pass. Doppler centroid prediction supplied in orbit for each 15 seconds, i.e., for SLC product normally only one Doppler centroid prediction could be contained in the data product, while for Wide swath product it is possible to have more than one predictions, such as the ScanSAR mode product in Figure 2.15.

If the surface is in motion, the velocity on the radial direction contributes to the Doppler shift leading to an estimation of ( $f_{Dc}$ ) from radar measurements which is different from the predicted ( $f_{Dcm}$ ) according to the orbit parameters. This difference expressed in equation (1) of [93], where a positive value of the surface motion radial component  $v_r$  corresponds to a target receding from the radar. The residual doppler centroid ( $f_{Dca} = f_{Dc} - f_{Dcm}$ ) is considered to have a linear relationship with the sum of surface velocity and current velocity [95]. Recent research reveals that Doppler centroid anomalies helps to improve the wind

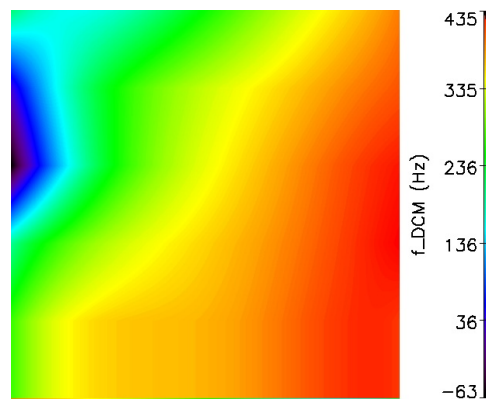


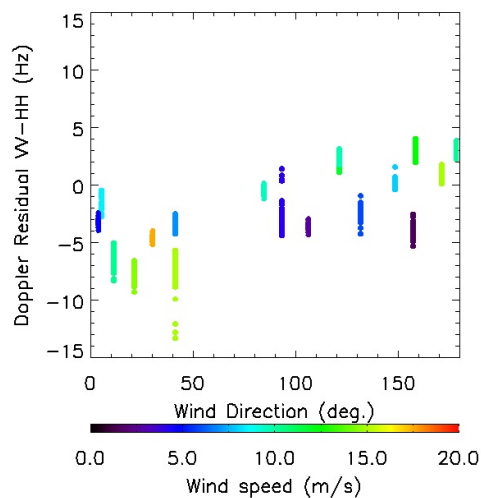
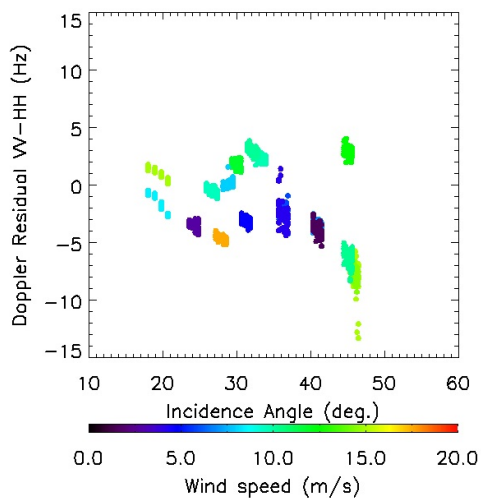
**Figure 2.15** — Doppler centroid predicted by satellite orbit parameters, for one scene of ScanSAR mode, ascending pass

direction retrieval [96]. For future SAR missions, in particular Sentinel-1, the Doppler centroid anomaly will be more robustly retrieved.

Doppler centroid corresponds to azimuth power spectrum density (PSD) peak location [97, 98] and can be estimated by analysing the phase of the correlation function of the complex signal measurements [97]. The estimation shown in Figure 2.16 were given in terms of difference between co-pols, which were estimated over blocks of  $512 \times 512$  pixels, where the azimuth correlation functions of each azimuth block of 512 pixels averaged over range block of 512 pixels. If the Doppler estimate is accurate enough, small block sizes are possible, down to an azimuth size of the order of the real antenna footprint [91]. For SLC data, total azimuth bandwidth equals azimuth bandwidth per look, while for SGF data, total azimuth bandwidth equals the sum of all the azimuth bandwidth per look [99]. The standard quad-pol SLC product were processed with an azimuth look bandwidth of  $900\text{Hz}$ , i.e, an integration time of  $T = 0.0011\text{s}$ , say the Doppler centroid shift between  $[-450\text{Hz}, 450\text{Hz}]$  (as equation 2 in [100]), according to the orbit as described at the beginning. For Bragg, there were too little difference between HH and VV to be detected even to the 6 iteration in our programme. On the point of view as target decomposition, the Doppler difference between HH and VV from the imagery is largely introduced by scalar contributions, which has a Doppler centroid different from that of Bragg, but concentrates with iterations (in Figure 2.16 compare (c) with (e)). On the right column in Figure 2.16, Doppler differences, with a linear function, relate to the azimuth angle between wind and radar LOS.

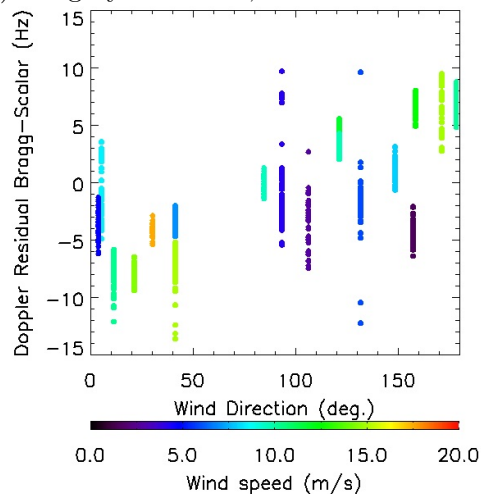
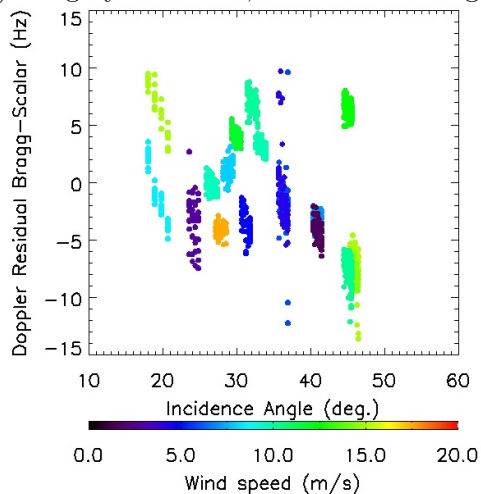
### 2.3.2.2 Azimuthal cut-off wavelength and wind sea

Orbital motions associated with the surface wave scatters cause azimuth smearing effect on SAR imaging, leaving waves with wavelength shorter than 'azimuth cut-off' unresolved. This cutoff is wind speed related and qualifies the retrieval of wave information from the data.



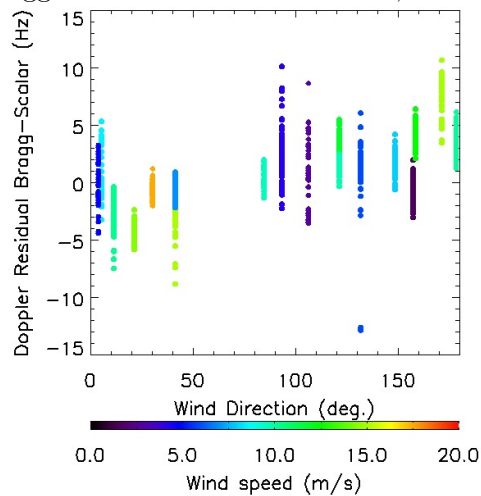
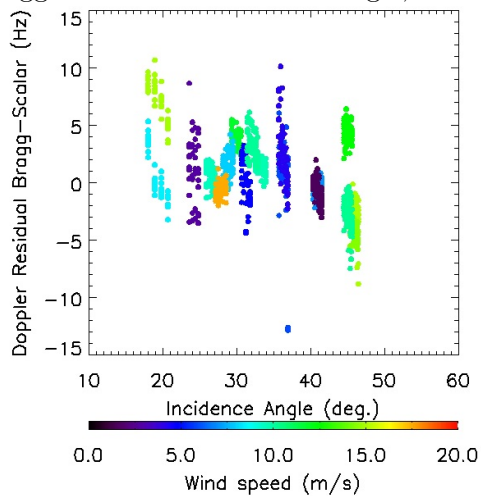
(a) imagery VV - HH, vs. incidence angle

(b) imagery VV - HH, vs. wind direction



(c) Bragg - Scalar vs. incidence angle, Iteration1

(d) Bragg - Scalar vs. wind direction, Iteration1



(e) Bragg - Scalar vs. incidence angle, Iteration6

(f) Bragg - Scalar vs. wind direction, Iteration6

Figure 2.16 — Doppler residual estimate by co-pol, Bragg, and scalar

Non-linearity theory of mapping ocean wave onto SAR imagery helps to find this cut-off. According to the theory [45], a roll-off Gaussian function  $\exp(-k^2\xi^2)$  filters out the linear part of SAR imagery spectrum, with  $\xi$  as the cut-off wavelength which could be estimated by fitting the auto-covariance function (ACF), which is derived from inverse Fourier transform of SAR image power spectrum, with the Gaussian cut-off factor [101]. As the azimuth Doppler frequency spectrum of SAR imagery could be approximated as a Gaussian filtered quasilinear spectrum, which has a correlation function as Figure 2.17(a), and to the pixel spatial domain as 2.17(b), the estimate of cut-off wavelength could be find by fitting with a Gaussian function. The central peak can be improved using cross correlation function between independent looks (Figure 2.17(c) and (d)) instead of correlation function of single look.

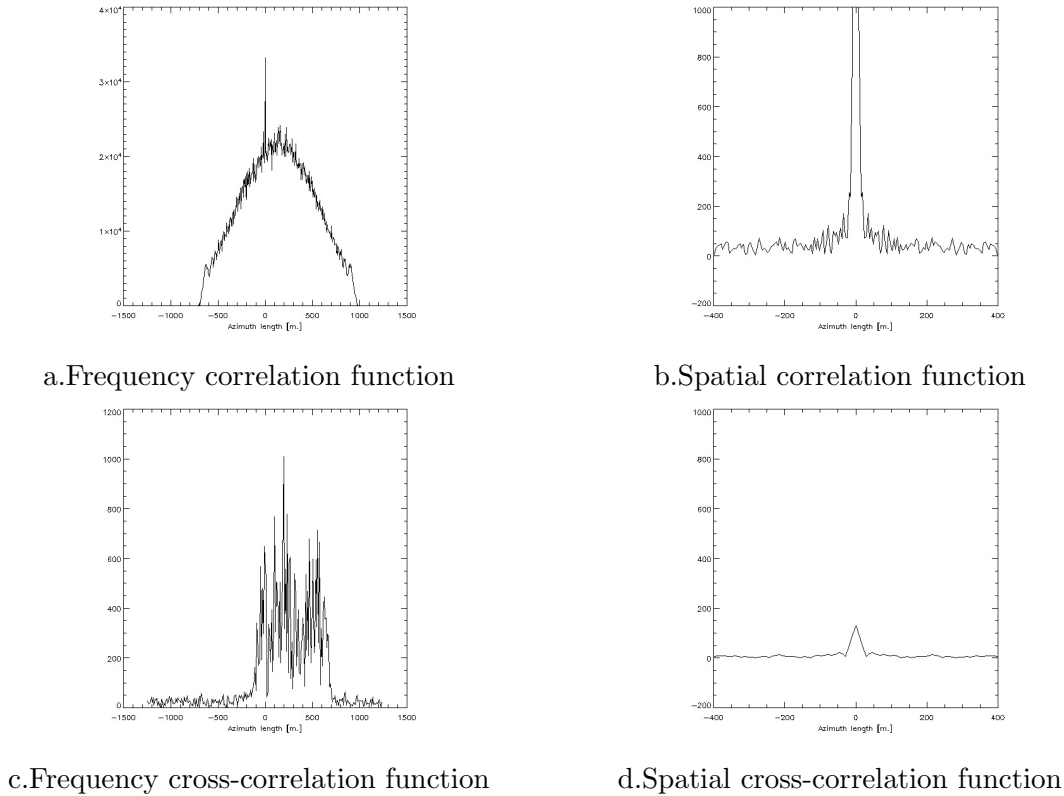
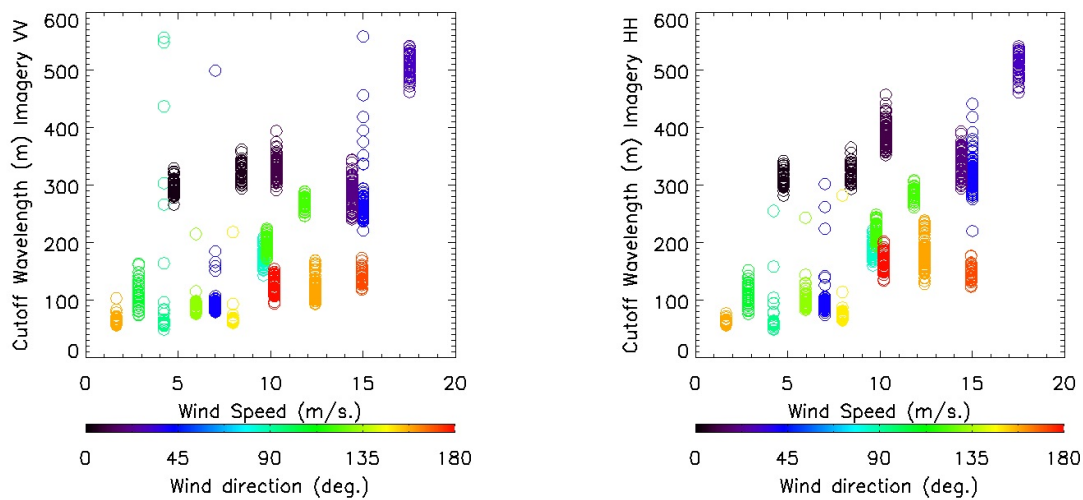


**Figure 2.17** — Doppler frequency cross- and co-spectra

SAR azimuth cutoff estimation is based on fully developed sea, where the lower integration limit  $k_{cutoff}$  is 1/6 of the peak of the wind sea spectrum [102]. For extremely high sea state, when the traditional wind retrieval algorithms based on the SAR backscatter measurements might be affected by the analog-to-digital saturation, azimuth cut-off exclusively depend on vertical components of sea surface orbital motions, having a linear relationship of [90]

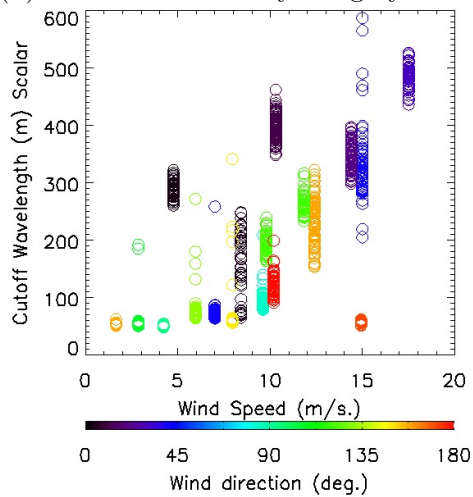
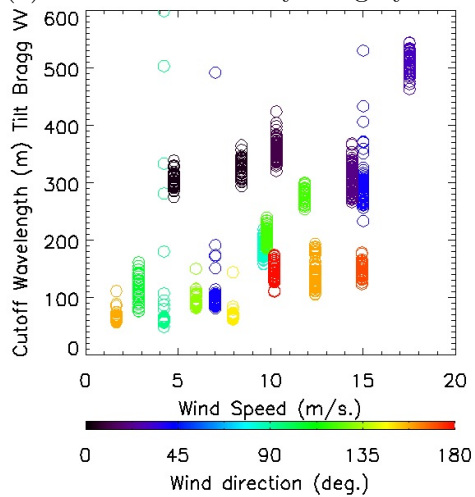
$$\lambda_c = 23.4 \cdot U_{10} + \Lambda \quad (2.33)$$

in which  $\Lambda$  represents a residual cut-off involving the nominal SAR azimuthal resolution.

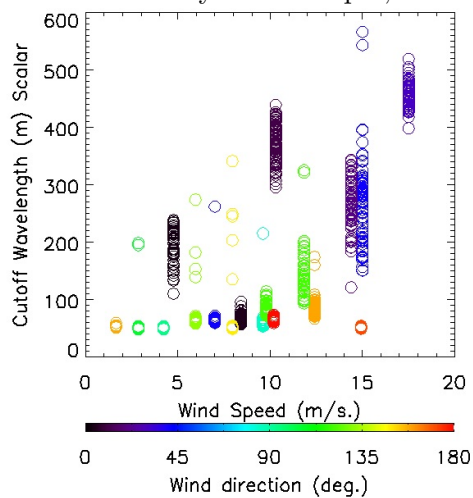
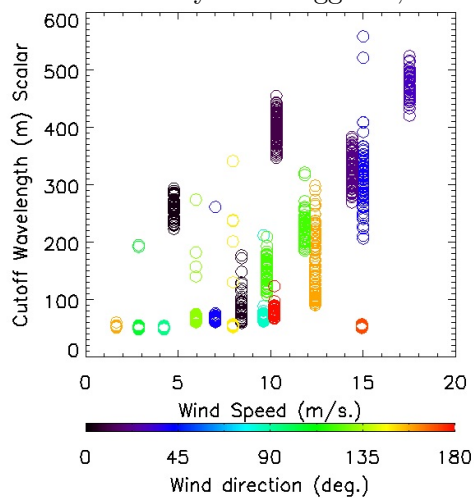


(a) Cut-off estimate by imagery VV

(b) Cut-off estimate by imagery HH



(c) Cut-off estimate by tilt Bragg VV, Iteration (d) Cut-off estimate by scalar co-pol, Iteration 1



(e) Cut-off estimate by scalar co-pol, Iteration 3 (f) Cut-off estimate by scalar co-pol, Iteration 5

Figure 2.18 — Cut-off estimate by co-pol Bragg and scalar scattering

Figure 2.18 shows the cut-off estimate for co-polarization (radar imagery, Bragg component, and Scalar component). Out of our expectation, Bragg contributions does not show a less variation than radar measurements, although still keep the linear shape along wind speed. The scalar part turns to give up the detection of cut-off, meaning that the scalar surface has very long coherence distance which may be longer than the imaging area, or has no coherence at all.

### 2.3.3 Spectral analysis

Wind streaks are manifestations of roll vortices in the planetary boundary layer [103, 104, 105, 106], corresponding to the linear, low-frequency expressions could be detected in SAR image [107]. By calculating Fourier transform over SAR imagery, the spectral energy corresponding to the wind streaks can be located, and the wind direction should be  $90^\circ$  from this direction of wind streak, with several degrees of rotation [108]. Detailed algorithm for detecting wind streaks from SAR imagery spectrum was illustrated in [109].

So far from what we know from the former analysis of Doppler shift and azimuth cut-off wavelength, the decomposition of SAR imagery into Bragg scattering and scalar contribution revealed two peak of the Doppler spectrum, which may corresponds to the wind sea and swell on the wave spectrum respectively. On this point of view, the decomposition would be optimized only when a maximum similarities between Bragg spectrum and its wind sea part as well as those between scalar spectrum and its swell part have been reached. With this hypothesis deducing different scattering mechanisms to different wave type, Bragg component and scalar component are expected to have only one peak respectively.

This criterion will be given as

$$J = \frac{Bragg}{Windseas} - \frac{Scalar}{Swell} \quad (2.34)$$

Wave spectrum partition is a problem having been studied for long. Three Butterworth filters used for spectrum splitting, as shown in Figure 2.19. Sub images of  $1024 \times 1024$  pixels contained only sea surface of the data set were studied. FFT window was set to be  $512 \times 512$  moving over sub images with step of 256 pixels, thus there are 9 FFT spectra for each sub image, and the sum of the 9 FFT spectra help to restrain noise level of the whole sub image. To detect wind streaks on those FFT spectra of  $512 \times 512$  pixels, only around  $10 \times 10$  pixels should be considered, due to a pixel spacing around  $5m$  and the scale of streaks from  $1km$  to  $9km$ . Concerning the partition of wind seas and swell, since we have azimuth cut-off wavelength estimated formerly, the median of cut-off was selected as the splitting wavelength. The filters for streak and wind seas are straightforwardly by a second order 2D Butterworth filters, and the filter for swell could be established as the product of the other two.

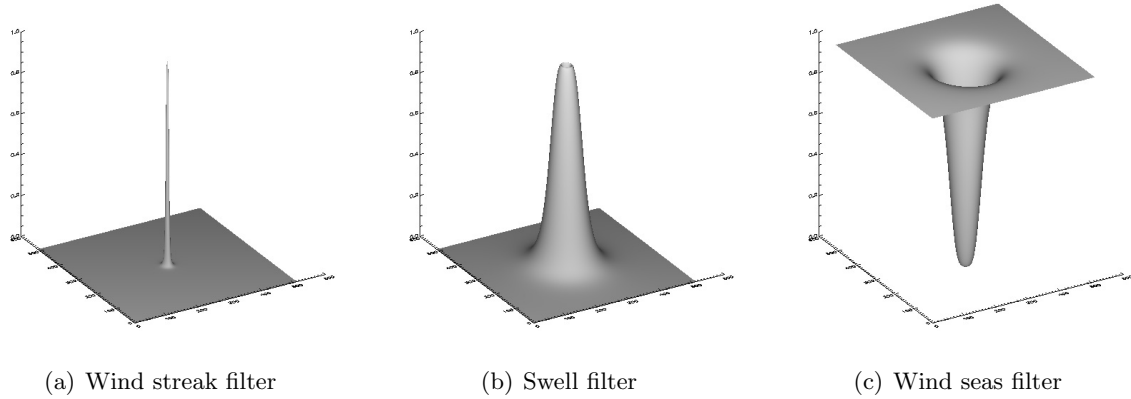


*Figure 2.19* — Three Butterworth filters for spectrum splitting

The variation of streak part and swell part is shown in Figure 2.20. Although the coherency of swell with scalar is not as expected, the one between wind seas and Bragg gives confidence of the criterion in Equation 2.34.

## 2.4 Discussion and conclusion

It is straightforward to derive from Equation (2.32) that

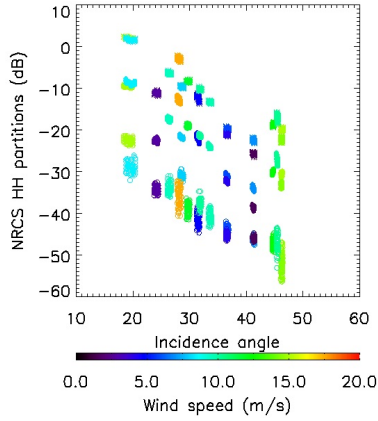
$$\begin{aligned} B(\beta + 1) &= S_{HH} + S_{VV} \\ B(\sin 4\phi) &= (S_{HH} - S_{VV}) \sin 2\phi - (S_{HV} + S_{VH}) \cos 2\phi \end{aligned} \quad (2.35)$$

Bragg contribution relates by  $\beta$  and  $\phi$  with complex HH+VV, HH-VV, and HV+VH, which are the three components of Pauli vector. Thus this decomposition is different from Pauli decomposition by introducing the depolarization ratio  $\beta$  and the surface slope  $\phi$ . With an estimate of Bragg from (2.35), the Scalar contribution could be found from (2.32). As we supposed formerly that Bragg and Scalar scatterers are following the model of random walking inside of each pixel area, if the first two equations in (2.32) be powered and then averaged for a sufficient pixel corresponding to an extent surface, Bragg and Scalar components are incoherent with each other but coherent in phase by themselves, and hence the complex product of  $B$  and  $S_a \hat{a}^- \hat{a}^-$  is zero on average. Thus the model proposed in [21] will be confirmed here,

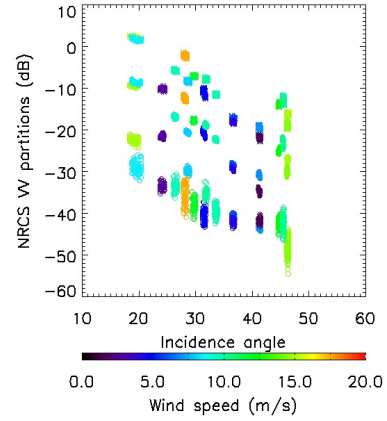
$$\sigma_{hh}^0 - \sigma_{vv}^0 = \sigma_{brHH}^0 - \sigma_{brVV}^0 \quad (2.36)$$

i.e., the Scalar contribution to  $\sigma_{hh}^0$  and  $\sigma_{vv}^0$  will be delimited by a subtraction and leaving only Bragg related contribution.

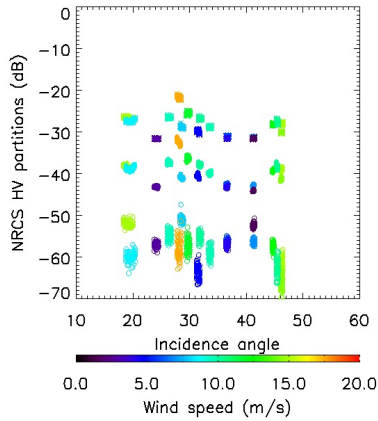
But when happened the average of complex product of  $B$  and  $S_a$  be non-zero? Figure 2.21 shows an example of HH vs. the sum of BraggHH and Scalar, VV vs. the sum of BraggVV



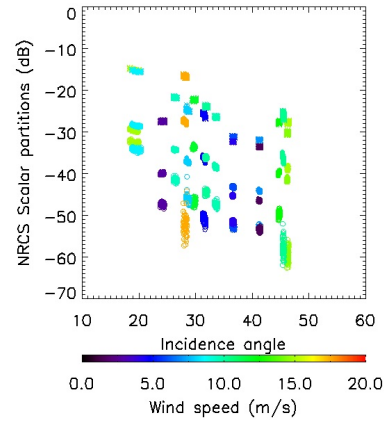
(a)  $NRCS_{hh}$  streak, swell, and wind sea



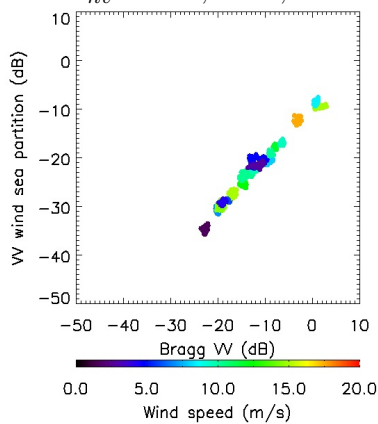
(b)  $NRCS_{vw}$  streak, swell, and wind sea



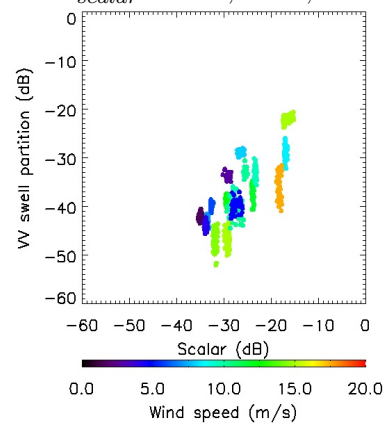
(c)  $NRCS_{hv}$  streak, swell, and wind sea



(d)  $NRCS_{scalar}$  streak, swell, and wind sea



(e)  $TiltBragg_{vw}$  vs. TiltBragg wind sea



(f)  $Scalar_{co-pol}$  vs. Scalar swell

Figure 2.20 — Spectra partitions

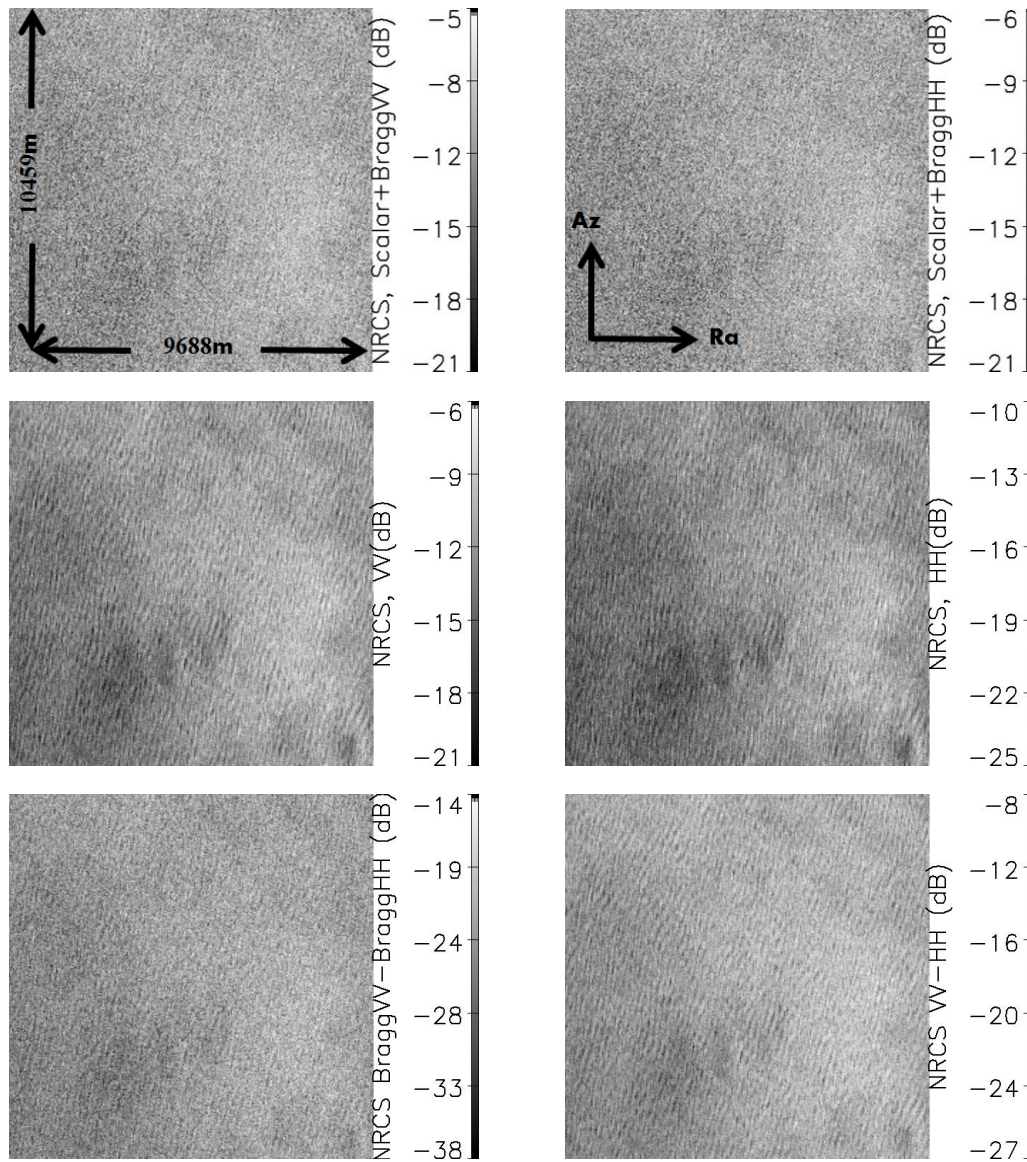
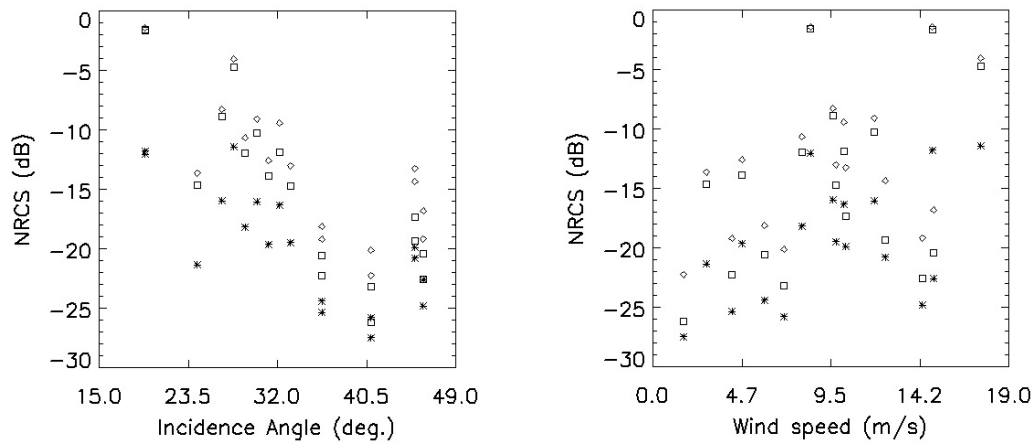


Figure 2.21 — NRCS HH and VV vs. sum of NRCS Bragg and NRCS Scalar, data No.20111205



*Figure 2.22* — NRCS HH (square), VV (diamond), and conj(BraggVV)\*Scalar (star)

and Scalar, and the comparison of VV-HH residual and Bragg VV-HH residual. Be consist with the spectral analysis of the data No. 20111205, Bragg components reveal more local wind related information, while HH, VV, even VV-HH is more influenced by the swell with a wave length around 300 meters.

In real conditions, there would rarely be non-related Bragg and Scalar scatterers, as shown in figure 2.22, where incidence angle and wind speed act as two fundamental rules for the value of NRCS. The correlation Bragg and Scalar (star) is normally 5-10 dB lower than the radar measured HH/VV. The fluctuation would be swell or current, any effect correlates Bragg scatterers with Scalar scatterers.

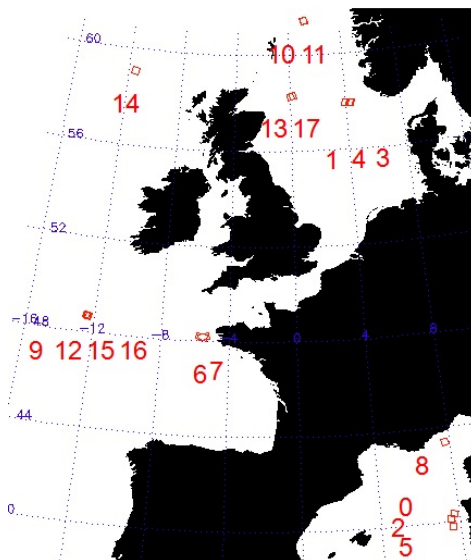


*Figure 2.23* — Location of data set.

Concerning about the data set, as shown in figure 2.23, where the numbers refer to the

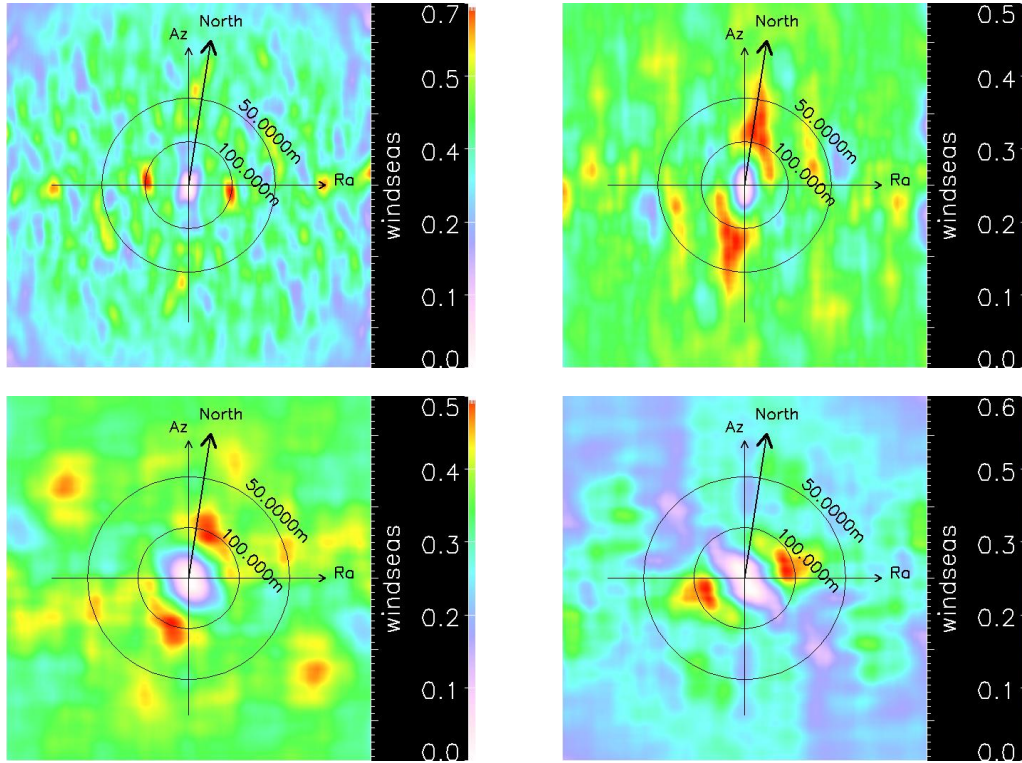


**Figure 2.24** — spectra for windseas, top: Scalar (left) vs. VV (right), data No.20110904; bottom: BraggVV (left) vs. VV (right), data No.20120509.

data numbers in table 2.1, the Mediterranean Sea wind seas have been extracted well either by Bragg or by Scalar, and some others from North Sea, Celtic Sea, and the Atlantic Ocean could also be retained by Bragg or Scalar. Two exceptions are shown in figure 2.24, where the data No.20110904 located to the west of Ouessant Island in the Celtic Sea, and the data No.20120509 located in the North Sea where is to the east of Scotland. For the Celtic scene, the correlation of Bragg and Scalar is very high (as in figure 2.22) and in fact the local wind of 14.92 m/s is inducing a wave of 100 meters to the the land. To the other end, the scene from North sea with a wind speed of only 2.85 m/s supplied an extreme low correlation of Bragg and Scalar, and although could be find from Bragg or Scalar spectra, a inclusion of the wind seas peak is overwhelmed by the a swell propagating along the North-South direction.

To sum up, the cross product of Bragg and Scalar contributions are not ignorable for most of cases, thus the sea surface depolarization and polarization could be separated by complex scattering matrix better than the NRCS. By separation of scattering polarization, the fine scale wind seas information are retained better than the direct SAR measurements.

*Chance, as we understand it, supposes the existence of things, and their general known properties: that a number of dice, for instance, being thrown, each of them shall settle upon one or other of its bases. After which, the probability of an assigned chance, that is of some particular disposition of the dice, becomes as proper a subject of investigation as any other quantity or ratio can be. But chance, in atheistical writings or discourse, is a sound utterly insignificant: it imports no determination to any mode of existence; nor indeed to existence itself, more than to non-existence; it can neither be defined nor understood: nor can any proposition concerning it be either affirmed or denied, excepting this one, "That it is a mere word."*

*Abraham de Moivre, 1735*

Microwave remote sensing is different from optical remote sensing where the different frequencies beyond visible light wavelengths supply an incoherent light source and meanwhile the high frequencies lead to very short coherence lengths, and hence to most optical receivers, echoes will appear incoherent so that make it possible to sum up their intensity contributions resulting in the speckle-free images. For microwave wavelengths, which is monochromatic and where the coherence length has an order of centimetres, the emitted radar wave train is generally far longer than the wavelength and we thus speak of a coherent illumination [89]. The sum of echoes backscattered by each target will be carried out coherently, i.e. amplitudes (in-phase) are summed up, resulting to a vary large intensity as the power of sum, rather than the sum of the power (the case of optical remote sensing). In fact speckle has been well-known for all coherent imaging modalities, such as laser imagery [32], optical coherent tomography [33], as well as the speckle-free photoacoustic tomography [34]. Speckle is not really noise but

rather contains information on the sensor and observed surface [35], while heretofore, speckle reduction is commonly known as 'filtering', although ill-suited, since speckle appears as a chaotic jumble and fluctuates the backscattered signal with a standard deviation to mean of unity, which is the same property as white noise [35, 32].

On the other hand, for an optical wavelength, the vast majority of surfaces are rough according to Rayleigh criterion, saying that for an incident angle  $\theta$ , if the mean quadratic deviation of the surface irregularities  $\delta h$  satisfies  $\delta h > \lambda/(8 \cos(\theta))$ , i.e. a mean quadratic phase shift higher than  $\pi/2$ , the surface is rough. While for microwave wavelength, surfaces expire the Rayleigh criterion easily, such a generic target, whose characteristic length of discontinuities  $L \gg \lambda$ , or a set of Rayleigh point targets, with  $L \ll \lambda$ . A generic target will be discussed in the following as Chapter 4 and a set of Rayleigh point targets has been discussed in Chapter 2.

Since radar was firstly used in the WWII for ship detection, the backscatter from the sea surface was found to obscure small boats, thus termed as 'sea clutter' [110]. Once successive realizations on rough surfaces are observed, scattering by a set of point targets could be considered as a randomly scattering [35, 32]. On this point, the observed sea clutter could be statically modelled as speckle-like characteristics. In fact, during the early days when a radar imaged over the sea surface with a resolution area much greater than the sea swell wavelength, clutter is usually modelled simply as speckle and the amplitude is Rayleigh distributed. As the radar resolution is increased, the clutter amplitude distribution is observed to develop a long 'tail' and the returns are often described as becoming spiky [42].

To sum up, the instantaneous power received from a single radar resolution cell varies about its mean, which is represented by the sea surface reflectivity, due to two contributions. The first source of the variation is the interference of these de-phased but coherent wavelets results in the granular pattern we know as speckle [32]. Another variation, as high resolution radar being used to resolve the finer structure of the sea surface, comes from the local surface shape, incidence angle, capillary wave density and the hydrodynamic effect by the passage of long waves and swell [42], whose effects on the SAR measurements have been presented in the former Chapter 2.

Filtering approaches, which have been historically designed for incoherent imaging, may have their limitations and yield less than optimal results when we try to extract specific information from SAR images. However, if we think of filtering as a sequence of decisions and estimates of unknown surface parameters, we see it fits perfectly well in a second approach [35]. In any case, we have to define the surface parameters and to determine the influence of speckle on our observations and consequently on their optimal assessment. For polarimetric SAR data, the speckle problem is more complicated than that for a single polarization data, because of the difficulties of preserving polarimetric properties as well as dealing with the

cross-product terms [111] for existed filters, such as the mostly promised Lee filter [112]. Above all, speckle is not real noise but the coherent result of all the scatterers inside the pixel area. We treat the radar signals stingily and care of even the trial information by pixel.

## 3.1 Theories

In the early days around 1990s, the well acknowledged model for SAR backscatter signal is a band-pass Gaussian random with 0 mean [113], for which the envelope obeys Rayleigh distribution, with a uniform phase on  $(0 - 2\pi)$ , and the power obeys negative exponential distribution. However, disobeying from Rayleigh distribution had been observed using high resolution radars [114], leading to improvements from then on. The approach of radar detections has anyhow been the compound, or multiplicative. In the computation of characteristic functions, the Mellin transform has been adopted recently, besides of the usual Fourier transform [115, 116]. The main clue of the story from circular Gaussian to K distribution and recently been generalized to G distribution will be shortly introduced in this section, and other more distributions could be found in [116, 117].

### 3.1.1 Complex circular Gaussian model

#### 3.1.1.1 Phase and circular Gaussian

We simplified in section 2.3 that for each kind of contribution to the total scattering matrix, there should be a random walk process among total backscattering of the same type. Random walk is amply substantiated by the coherent frequency of radar wavelength scattering on a randomly structured rough surface, with an ignorable volume scattering. At this point, the phase information contained in complex scattering coefficients  $B, S_a$  of equation 2.26 should be regarded as the sum of several phase shifts [35]:

$$B = \sum b_i R_h(\theta, \epsilon) = \sum a_i m_s R_h(\theta, \epsilon) = \sum |B_i| e^{k\varphi_i} \quad (3.1)$$

and

$$S_a = \sum s_j = \sum |S_{aj}| e^{k\varphi_j} \quad (3.2)$$

where  $k$  denotes the imaginary unit vector, and

$$\varphi_{\{i,j\}} = \arg S_{pq\{i,j\}} + \arg h(x_{\{i,j\}}, y_{\{i,j\}}) + \frac{-4\pi D_{\{i,j\}}}{\lambda} \quad (3.3)$$

with  $S_{pq}$ ,  $p, q \in \{H, V\}$  denotes the polarization component of the scattering matrix, and  $h(x_{\{i,j\}}, y_{\{i,j\}})$  the radar response function by scattering point  $(x_{\{i,j\}}, y_{\{i,j\}})$  on the surface,  $D_{\{i,j\}}$  the range distance between radar and the scattering point  $(x_{\{i,j\}}, y_{\{i,j\}})$  on the surface.

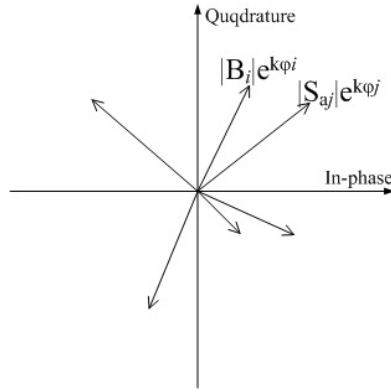


**Figure 3.1** — Random walk on the complex plain of backscatters for isolated single pixel area

We have known in Chapter 2 that  $\arg S_{pq}$  of Bragg scattering depends on local incidence angle and complex permittivity on/of the sea surface, while  $\arg S_{pq}$  of scalar contributions, for which a cylinder-like approximation was used, has no difference between VV polarization and cross-polarization, with a  $\pi$  difference from HH polarization, c.f. equation 2.26.

The second item on the right  $\arg h(x_{\{i,j\}}, y_{\{i,j\}})$  depends on the radar configuration thus could be taken as a system constant. The last item relates only to range distance hence is surface roughness dependent. In the surface area corresponding to one pixel size on the SAR imagery, the differences between various ranges  $D_{\{i,j\}}$  of an order of  $\lambda/2$  are enough to cause destructive interferences. In [28], Rayleigh criterion was replaced by Fraunhofer criterion,  $\delta h > \lambda/(32 \cos(\theta))$ , which is more stringent requiring the maximum phase difference between rays coming from the center and the edge of the antenna be less than  $\pi/8$ .

Based on the above analysis, we can see a random walk of the backscatters on the complex plain, as in figure 3.1, where an 0 mean value for real and imaginary part of the complex signal achieved by a large number of scatters separately, i.e.  $i, j \in [0, N]$  for which the scatterers number  $N$  is readily to be as large as enough to satisfy the central limit theorem (on the list of C), and the envelop (amplitude,  $A$ ) received from this single pixel to be around the sea surface reflectivity  $R$ , according to a Rayleigh distribution

$$p_A(A/R) = \frac{2A}{R} \exp\left(-\frac{A^2}{R}\right) \quad (3.4)$$

whose power (intensity,  $I$ ) obeys exponentially distribution

$$p_I(I/R) = \frac{1}{R} \exp\left(-\frac{I}{R}\right), \quad (3.5)$$

using the change of variable relation  $p_A(A) = 2Ap_I(A^2)$ . The complex signal ( $C_s = \Re(C_s) + i\Im(C_s)$ ) received from each single pixel is called complex Gaussian random variable, for which the vector of real and imaginary parts ( $vector = (\Re(C_s), \Im(C_s))$ ) is bivariate Gaussian distributed [118].

### 3.1.1.2 Multivariate complex Gaussian distribution

Now we consider not only about each isolated but more pixels, i.e. to take SAR imagery as samples of realization for the complex Gaussian random process, i.e. radar reflectivity  $R$  of the pixel area. So far, we regard radar reflectivity as uniform all over the imagery, i.e. the imagery area is homogeneity. The whole of these samples is already a  $p$ -variate (set  $p$  the pixel number of the SAR imagery) complex Gaussian random variable,  $z = (C_{s1}, C_{s2}, \dots, C_{sp})^T$ , which is a  $p$ -tuple of complex Gaussian random variables such that the vector of real and imaginary parts,  $(\Re(C_{s1}), \Im(C_{s1}), \dots, \Re(C_{sp}), \Im(C_{sp}))^T$ , is  $2p$ -variate Gaussian distributed [118]. The distribution of  $z$  is

$$p(z) = \frac{1}{\pi^p |\Sigma_z|} \exp(-z^{T*} \Sigma_z z), \quad (3.6)$$

where  $\Sigma_z = E(z z^{T*}) = \|E(C_{si} C_{sj}^*)\| = \|\sigma_{ij}\|$ , the  $p$  Hermitian positive definite complex covariance matrices, generalizes the radar reflectivity concept, since its diagonal elements,  $C_{sp}$  variances, correspond to radar reflectivities  $R_p$ , for

$$\sigma_{ij} = \begin{cases} \sigma_i^2 & \text{if } j = i, \\ (\alpha_{ij} + k\beta_{ij})\sigma_i\sigma_j & \text{if } j \neq i. \end{cases} \quad (3.7)$$

where  $k$  is the imaginary unit. Moreover, in equation 3.7, the non-diagonal elements, covariances between  $C_{si}$  and  $C_{sj}$ , are proportional to the complex correlation coefficient [119]

$$\rho_{ij} = \frac{E(C_{si} C_{sj}^*)}{\sqrt{E(C_{si} C_{si}^*) E(C_{sj} C_{sj}^*)}} = D_{ij} \exp(k \arg(\frac{\beta_{ij}}{\alpha_{ij}})) \quad (3.8)$$

where the complex correlation module  $D_{ij}$  is simply called coherence, while the phase  $\arg(\frac{\beta_{ij}}{\alpha_{ij}})$  is the effective phase shift between  $C_{si}$  and  $C_{sj}$ .

### 3.1.1.3 Gamma distribution

One special multivariate case is multi-look processed data. Multi-look processing reduce the fully developed speckle into non-fully developed, by dividing the Doppler spectrum into  $L$  sub-looks. The looks generally overlap and the  $L$  sub-looks will then be correlated. Operationally, a weighting filter (e.g., an Hanning filter for ERS1/2 and ENVISAT) is used to decorrelate the  $L$  sub-looks [35]. After this processing, we have  $L$  independent samples for each pixel, the averaged power fit a Gamma distribution as

$$p(I) = \frac{L(LI)^{L-1}}{(L-1)!(\alpha\sigma^2)^L} \exp(-\frac{LI}{\alpha\sigma^2}) \quad (3.9)$$

where  $I = \frac{1}{L} \sum (\Re(C_{si})^2 + \Im(C_{si})^2)$  is the averaged power for each pixel,  $\Re(C_{si})$  and  $\Im(C_{si})$  are independently Gaussian distributed real and imaginary part of the complex signal, for

which

$$\begin{aligned} p(\Re(C_{si})) &= \frac{1}{\sqrt{\pi R}} \exp\left(-\frac{\Re(C_{si})^2}{R}\right) \\ p(\Im(C_{si})) &= \frac{1}{\sqrt{\pi R}} \exp\left(-\frac{\Im(C_{si})^2}{R}\right) \end{aligned} \quad (3.10)$$

where  $R$  is the radar reflectivity for the pixel area.  $\alpha$  is the square law coefficient,  $L \geq 2$  is the look number and  $\sigma^2$  is the Gaussian covariance for both  $\Re(C_{si})$  and  $\Im(C_{si})$ , and  $\sigma^2 = \frac{R}{2}$ .

Gamma distribution  $\mathcal{G}(\alpha, \beta, \gamma)$  is the type III solution to Pearson system [120], determined by  $\alpha, \beta, \gamma$ ,

$$p_X(x) = \frac{(x - \gamma)^{\alpha-1} e^{-(x-\gamma)/\beta}}{\beta^\alpha \Gamma(\alpha)}, x > \gamma; \alpha > 0, \beta > 0. \quad (3.11)$$

If  $\gamma = 0$ , three-parameter Gamma is simplified to double-parameter Gamma distribution  $\mathcal{G}(\alpha, \beta)$ ,

$$p_X(x) = \frac{x^{\alpha-1} e^{-x/\beta}}{\beta^\alpha \Gamma(\alpha)}, x > 0; \alpha > 0, \beta > 0. \quad (3.12)$$

and when  $\beta = 1, \gamma = 0$ , Gamma distribution has the standard expression as

$$p_X(x) = \frac{x^{\alpha-1} e^{-x}}{\Gamma(\alpha)}, x > 0. \quad (3.13)$$

Obviously,  $\alpha$  is the shape parameter of Gamma distribution while  $\beta$  is the scale parameter. When  $\alpha = 0$ , the standard Gamma distribution (3.13) turn out to be a negative exponential distribution, corresponding to multi-looking processed Gamma distribution and single look negative exponential distribution respectively. If  $\alpha$  is positive, the standard Gamma distribution has a name of Erlang distribution. Furthermore, if random  $U_1, U_2, \dots, U_v$  obey Gaussian distribution independently, then  $\sum_{j=1}^v U_j^2$  will follow a standard Gamma distribution (3.13) with  $\alpha = v/2, \beta = 2, \gamma = 0$ ,

$$p_X^2(x^2) = \frac{(x^2)^{\frac{v}{2}-1} e^{-x^2/2}}{2^{\frac{v}{2}} \Gamma(\frac{v}{2})}, x^2 > 0. \quad (3.14)$$

This type of Gamma distribution has a name of  $\chi^2$  distribution with a freedom of order  $v, \chi_v^2$ . For  $\frac{1}{2} \sum_{j=1}^v U_j^2$ , the standard Gamma distribution of  $\alpha = v/2, \beta = 1, \gamma = 0$  works well,

$$p_X^2(x^2) = \frac{(x^2)^{\frac{v}{2}-1} e^{-x^2}}{\Gamma(\frac{v}{2})}, x^2 > 0. \quad (3.15)$$

The  $\chi^2$  distribution, negative exponential distribution, Gamma distribution and Erlang distribution all belong to exponential family.

#### 3.1.1.4 Wishart distribution, coherence, and phase difference

Another multivariate case, multi-polarization data, is in a more general case where the statistics of phase difference and coherence between difference channels are of ultimate importance.

Furthermore, their statistical characteristics are not limited to the intensities or amplitudes [1]. For a quad-pol case with a pixel number of  $p$ , each polarization channel could be regarded as a  $p$ -variate complex Gaussian random variable, whose possibility distribution function is as Equation 3.6, and the four-polarization-channel could be regarded as four samples of  $p$ -variate complex valued vectors. The polarimetric covariance matrix,  $n\hat{\Sigma}_z = \sum z_{1\dots p}^{T*} z_{1\dots p}$ , (for quad-pol here  $n = 4$ ), is found to have a complex Wishart distribution [118],

$$p(n\hat{\Sigma}_z) = \frac{|n\hat{\Sigma}_z|^{n-p}}{I(\Sigma_z)} \exp\left(-\text{tr}(\Sigma_z^{-1} n\hat{\Sigma}_z)\right) \quad (3.16)$$

where  $I(\Sigma_z) = \pi^{p(p-1)/2} \Gamma(n) \cdots \Gamma(n-p+1) |\Sigma_z|^n$ .

The above consideration about multi-polarization data is straightforward from Section 3.1.1.2, while there is another way of thinking of the  $p$ -variate vector and its samples of realization, i.e., to consider the quad-pol data as  $p$  realizations of 4-variate vector, then the polarimetric covariance matrix,  $p\hat{\Sigma}_z = \sum z_{1\dots 4}^{T*} z_{1\dots 4}$  have the complex Wishart distribution as

$$p(p\hat{\Sigma}_z) = \frac{|p\hat{\Sigma}_z|^{p-n}}{I(\Sigma_z)} \exp\left(-\text{tr}(\Sigma_z^{-1} p\hat{\Sigma}_z)\right) \quad (3.17)$$

where  $I(\Sigma_z) = \pi^{n(n-1)/2} \Gamma(p) \cdots \Gamma(p-n+1) |\Sigma_z|^p$ , for quad-pol here  $n = 4$ . A special case for single polarization channel can be achieved when  $n = 1$  and Equation 3.17 has the same expression as Equation 3.9. By this explanation,  $p$  could be regarded as either the pixel number of a single look sub imagery or a  $p$ -look processing.

Lee et al. [112] proved that the correlation coefficient of multi-look intensities is independent of the number of looks and to be the  $D_{ij}^2$  of Equation 3.8.

### 3.1.1.5 Non-Gaussian cases

The above hypothetical condition modelled well the SAR imagery when the resolution was not so fine thus be able to enclose a large number of scatterers which are equivalently and randomly de-coherent in phase, leaving a random variation by in-phase coherent sum.

As we mentioned in Chapter 2, casual observations have shown that the sea surface is not a random rough surface but a superposition of significant structures. The imaging mechanism has been a controversial issue for quite a while. The main problem still lies in the proper inclusion of the motion effects associated with ocean surface waves. Nevertheless, all the different theories consider the velocity bunching effect as a basic imaging element. In fact, the hydrodynamic interactions between short and long gravity waves imply that a given resolution cell roughness is dependent on the position of the cell on the wave [56]. Then the number of scatterer per resolution cell is directly related to the sea state. With this consideration, ENVISAT ASAR had been configured to concentrate the main efforts

on a better representation of the hydrodynamic modulation transfer function by its higher incidence angles and both VV and HH polarisation settings [67].

### 3.1.2 *K*-distribution family

Rayleigh distribution approximated well the envelope of the return signal when the radar illuminates a large area of the sea. However, non-Rayleigh sea clutter was found since the narrow beam-divergence and short pulse-length had been used on radars illuminating sea surface. If the radar has pulse-to-pulse frequency diversity greater than the reciprocal of the pulse length, which is generally considered sufficient to decorrelate returns, there is still pulse-to-pulse correlation with respect to the whole population of returns [114, 121, 122]. For RADARSAT2, a pulse bandwidth of 100MHz is acquired to achieve a range resolution of 3 meters for ultrafine mode [94], while even for the fine mode, where the pulse bandwidth of 30MHz vs the pulse length of  $21\mu s$ , can definitely find the pulse-to-pulse frequency diversity greater than the reciprocal of the pulse length. As early as 1970s, the non-Rayleigh distribution such as Lognormal distribution and Weibull distribution has also been proposed in literatures, but *K*-distribution has been proved to be the most accuracy [123, 121].

#### 3.1.2.1 Correlation effect

As the refinement of resolution, the pixel cell area on the surface will not be "homogeneity" as an average of a large area but contains structures, i.e. Bragg wave modulated by longer waves, currents, etc. Valenzuela [124] suggested that the return from a single 'patch' of sea surface can be expressed as the product of two statistically independent factors, one related to the intrinsic properties of the 'patch' and the other to its overall tilt. They assumed the first factor to be negative exponentially distributed and the latter a rather complicated expression. Here will refer what have been discussed in Section 3.1.1.5. The radar reflectivity  $R$ , which is the parameter of most interest, will not be uniform. Thus it is straightforward to consider the Equation 3.4 as a 2-variate distribution

$$p_{A,R}(A, R) = \int \frac{2A}{R} \exp\left(-\frac{A^2}{R}\right) p(R) dR \quad (3.18)$$

where  $p(R)$  is the probability density function of the radar reflectivity  $R$ . Measurements identified this variation as a Gamma distribution [42], which also proved that multi-look processing isolated the Gaussian speckle variation and left the large scale variation of the radar reflectivity  $R$  much more clear.

### 3.1.2.2 $K$ -distribution

$K$ -distribution was first introduced in 1976 by Jakeman [125] as the development of non-Rayleigh sea clutter modelling. The basic assumption of this modelling is that the scattered electric field can be written as the sum of contributions from  $N$  independent scatterers,

$$\xi(r, t) = e^{j\omega t} \sum_{i=1}^N a_i(r, t) e^{j\varphi_i(r, t)} \quad (3.19)$$

where  $a_i(r, t)$  is a real form factor governing the angular distribution of radiation from the  $i$ th scatterer,  $\varphi_i(r, t)$  is a phase factor depending on its position at time  $t$  with respect to the observation point  $r$ . Defining the RCS  $\sigma(r, t)$  to be equal with the square of the envelope of the field,  $\sigma(r, t) \equiv |\xi(r, t)|^2$ , formula 3.19 describes a 2-D random walk in the complex plane of  $N$  steps of lengths  $\{a_i\}$ , which was introduced with approximation methods in the previous chapter 2, and is useful in statistical modelling of the RCS in 2-D plane hence form a 2-D SAR imagery. To be different from the approach of Valenzuela [124] and modelling the second factor,  $p(R)$  in Equation 3.18, as the  $\chi^2$  distribution with a freedom of order  $2(\nu + 1)$ , an exact solution of the finite 2-D random walk problem is  $K$ -distribution,

$$p(a; r) = \frac{2b}{\Gamma(1 + \nu)} \left(\frac{ba}{2}\right)^{(\nu+1)} K_\nu(ba), \quad \nu > -1 \quad (3.20)$$

where  $\Gamma(\cdot)$  is the Eulerian Gamma function,  $K_\nu(\cdot)$  is the modified Bessel function of the second kind of order  $\nu$ . The most important feature of the  $K$ -distribution is that Equation 3.20 leads to an integral, where the freedom of the  $\chi^2$  distribution is integrated to be  $2N(\nu + 1)$ , which can be evaluated analytically giving the RCS distribution

$$P_N(\sigma; r) = \frac{b/\sqrt{\sigma}}{\Gamma(M)} \left(\frac{b\sqrt{\sigma}}{2}\right)^M K_{(M-1)}(b\sqrt{\sigma}) \quad (3.21)$$

where  $M = N(\nu + 1)$  is referred to as a shape parameter and  $2\sqrt{M}/b$  is the slope parameter of the distribution. In particular the shape parameter  $M$  is a real and non negative parameter which indicates the departure from the exponential model of a fully developed speckle, while the slope parameter is related to the mean intensity of the local backscattered field.

Another important assumption endowing  $K$ -distribution its reasonableness for non-Rayleigh sea clutter is the statistical independence of  $\{a_i\}$  from  $\{\varphi_i\}$ , leading to an estimate of the shape parameter  $M$  according to Equation (28) and (12) in [125]. Although the statistical independence of  $\{a_i\}$  from  $\{\varphi_i\}$  is still satisfied, the assumption of an uniform phase had been found not satisfied when the phase,  $\varphi$ , does not distributed uniformly, i.e., the RCS of 2-D random walk results a directional bias[126]. The non-uniform phase effect led to a generalized  $K$ -distribution, c.f. Section 3.1.2.3.

Furthermore, the indefinite integral of formula 3.21 can be performed exactly and the result expressed in terms of another modified Bessel function,

$$\int_0^X P_N(\sigma; r) d\sigma = 1 - \frac{2}{\Gamma(M)} \left( \frac{b\sqrt{X}}{2} \right)^M K_M(b\sqrt{X}) \quad (3.22)$$

This property is of particular value for calculating false-alarm and missed-signal probabilities in modeling the detection of targets in the presence of sea clutter.

### 3.1.2.3 Generalized-K

Barakat [126] generalized  $K$ -distribution ( $GK$ ) to a directional weak diffuser, which has a phase parameter to describe the phase departure from the uniform distribution, and Jakeman [127] analysed properties of  $GK$  by more general  $n$ -dimensional random walk assumption, to find the identical representation of  $GK$  and Rician distribution.

The generalized- $K$  ( $GK$ ) embodies Rayleigh,  $K$ , and Rice scattering scene which are typical of marine scenes by three-parameters, whose expression for RCS  $\sigma(r, t)$  is given by [128] which was originally Equation (4.5) in [126],

$$P_N(\sigma; r) = \frac{cb/\sqrt{\sigma}}{\Gamma(M)} \left( \frac{b\sqrt{\sigma}}{2c} \right)^M K_{(M-1)}(cb\sqrt{\sigma}) I_0\left(\frac{b\sqrt{\sigma}}{2\sqrt{M}}\alpha\right) \quad (3.23)$$

where  $c = \sqrt{1 + \alpha^2/(4M)}$  with  $\alpha$  the departure from the uniform distribution of the phase [127, 126], and  $I_0$  is the first kind modified Bessel function of 0th order. The other two parameters,  $2\sqrt{M}/b$  and  $M$ , are inherited from two-parameter  $K$ -distribution. In Rice distribution,  $\alpha$  deals with the presence of a dominant specular component [128]. Using the  $GK$  distribution. Ferrara et al. [129] analysed the metallic objects over sea surface to model the em backscatter from sea surface with or without metallic object by one statistic representation, by the analogy to a Ricean distribution which was discovered by S. O. Rice [130], the pioneer in the field of communication theory, and is generally used to indicate the link quality for wireless communication [131]. Fried [132] derived a theory to calculate the two parameters of the Rician distribution for laser radar cross section from a randomly rough target, and recently, Rician distribution has been reviewed by radar engineers for radar measurements[133].

## 3.2 ENL analysis

The RADARSAT-2 is Canadian satellite launched in December, 2007, onboard which is the next-generation C-band synthetic aperture radar (SAR). RADARSAT-2 SAR products are characterized by different beam modes used by the satellite and levels of processing for data

**Table 3.1** — Description of RADARSAT-2 SAR data for the experiment

data NO	acquisition	center	beam mode
A	20090903T065905	13.857449W,38.538203N	ScanSAR wide
B	20090818T174203	3.4700495E,39.206341N	ScanSAR wide
C	20090831T180450	3.0840412W,43.836872N	Wide swath single
D	20090903T065703	11.326580W,47.208936N	Wide swath single

samples	lines	incidence angle	looks R/A	pixel spacing	line spacing
10536	12402	19.4336185-49.4577484	4 / 2	50	50
10521	9976	19.4126492-49.4239120	4 / 2	50	50
7378	22743	30.7488785-39.5422554	1 / 1	11.8326979	4.96723223
7378	54122	30.7951603-39.5673752	1 / 1	11.8326979	4.96975422

**Table 3.2** — Description of RADARSAT-2 SAR data for the experiment (cont.)

data NO	samples	lines
C1	7378	11372
C2	7378	11372
D1	7378	10824
D2	7378	10824
D3	7378	10824
D4	7378	10824
D5	7378	10824

products. To examine speckle characteristics observed from RADARSAT-2 polarization products, two SLC products acquired in wide swath single beam mode with dual polarization of HH+HV and two SCW products acquired in ScanSAR Wide beam mode with dual polarization of HH+HV have been analysed, as in Table 3.1, which lie in the sea area around Iberian Peninsula, to the southwest (acquired on Sep. 3th, 2009), the east (acquired on Aug. 18th, 2009), the northeast (acquired on Aug. 31st, 2009) and the northwest (acquired on Sep. 3th, 2009) separately of the peninsula. Due to the large pixel size on azimuth direction of the SLC data, the whole image was split in azimuth direction into 2 parts and 5 parts for data C and D respectively, while for SCW data, the image can be processed as a whole. After splitting, data C turns to be C1 and C2, and data D turns to be D1, D2, D3 D4 and D5, shown in Table 3.2.

A land mask with a resolution of 1km from NGDC is used to focus the analysis on the

sea area. The sub images of 30\*30 pixels are collected over sea area by the land mask. Firstly we visit the whole image by sliding a window of 30\*30 pixels in step of 15 pixels. The file lutSigma.xml scaling Look-up Table (LUT) included with the product is used to convert the digital numbers in the SAR imagery to sigma-nought values, applying a constant offset and range dependent gain to the SAR imagery.

### 3.2.1 ENL and Chi-square test

Multi-look processing is the most commonly used speckle reduction technique, it reduces speckle 'noise' by averaging single-look images, in the sacrifice of resolution. The principle behind this technique is that the sum of  $N$  identically distributed real-valued uncorrelated random variables has a mean value which is  $N$  times the mean of any one component [136]. Traditional digital multi-look processing consists of incoherent addition of independent looks of the same scene. The looks can be obtained by partitioning the available signal bandwidth and processing each look independently. If no look overlapping is used, similar results are obtained by using a simple mean filter applied on the one look processed image [137]. The equivalent (or effective) number of looks (ENL) describes the degree of the averaging applied to SAR measurements, and therefore it is a parameter to describe the speckle characteristic of SAR imagery, and to be used as an indicator of the quality of SAR images generated, with the definition as

$$\text{ENL} \triangleq \frac{(E(I))^2}{\text{VAR}(I)} = \frac{[E(I)]^2}{E(I^2) - [E(I)]^2} \quad (3.24)$$

where  $I$  is the intensity of a pixel in the multiple-look image,  $E(\cdot)$  and  $\text{VAR}(\cdot)$  represents the expectation value and the variance of  $I$  respectively [138]. This definition trace back to the early days when the intensity images are generally acquired by a square-law detector of the envelope detection [136].

Multi-look processing has been discussed in Section 3.1.1.3, where a weighting filter had been used to decorrelate sub-looks and arrived at the Gamma distributed intensity, which supplies an improved estimate of the geophysical parameter  $\sigma$  or  $\sigma^0$  [36]. If the multi-look is carried out with  $L$  correlated sub-looks, the intensity of the averaged image, with a look number of  $L' < L$ , is no longer distributed according to a Gamma distribution, but rather according to Goodman distribution [35, 119], where the intensity distribution is expressed in terms of  $L$  real non-negative eigenvalues  $\lambda_k$  of the covariance matrix. The Goodman distribution is almost always approached in practice by a Gamma distribution using  $L'$  rather  $L$ , by the relation with the coefficient of variation (CV)  $\gamma_S$

$$\gamma_{SI} = \frac{1}{\sqrt{L'}} \quad (3.25)$$

where

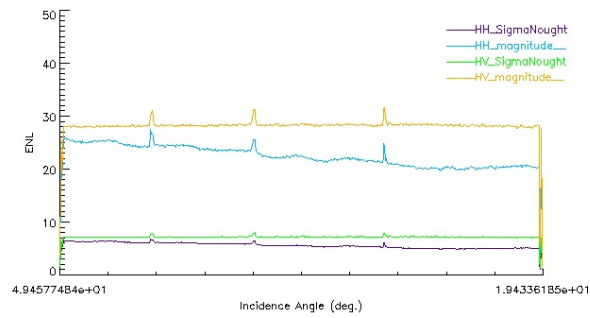
$$\gamma_{SI} \triangleq \frac{\sqrt{\text{VAR}(I)}}{E(I)} = \frac{\sqrt{E(I^2) - [E(I)]^2}}{E(I)} \quad (3.26)$$

is the ratio of the standard deviation to the mean and sometimes called a contrast parameter, a measure of speckle strength which is always unity for speckle [119]. We note in Equation 3.25 that for  $L$  independent sub-looks,  $L'$  will be replaced by  $L$ . From this understanding, ENL has a physical meaning as the reciprocal of the power of coefficient of variation  $\gamma_S$ .

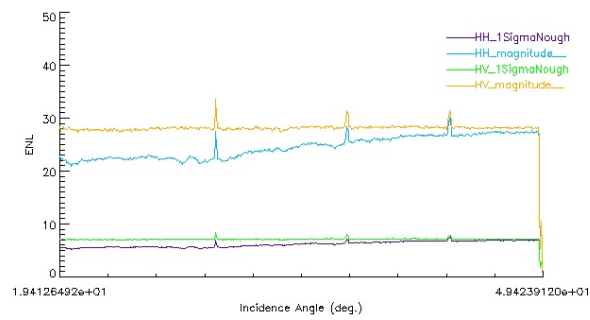
The contrast is an important parameter contributing the improvement of speckle models from uniformly Gaussian distributed to finer surface structures considered, such as K, distributions. Pioneer experimental work by Fujii and Asakura [139] found that the contrast of the speckle is related to the surface roughness and already one year before, Berny and Imbert [140] developed an optical instrument for measuring surface roughness based on the properties of the diffuse and specular reflected fields. ENL was also used to classify targets with directional behavior from the SAR imagery [141]. Concerning various sea state imaged by SAR, sea clutter model such as Gaussian, lognormal, K, Rayleigh, Weibull have been quantitatively tested by Pearson's  $\chi_m^2$  test [142], which indicates K models sea clutter the best, then lognormal, which is still better than Gaussian, Rayleigh and Weibull [143, 144].

In this study, ENL was investigated for dual polarization channels of both magnitude data and sigma nought, and comparisons between HH and HV polarization as well as those with and without incidence angles affection are plot in Figure 3.2. For the SCW products, sub images of different sea area (so with different incident angle) from each of the SAR imagery (both HH and HV) composed a data set. Then the ENLs (Equivalent Number of Looks) are calculated for each sub image, compared with the ENL given by the description of the product. For each sub image, the fitness of the histogram with Gamma as well as Gaussian distribution are tested by chi-square statistical test of  $\chi_m^2$ .

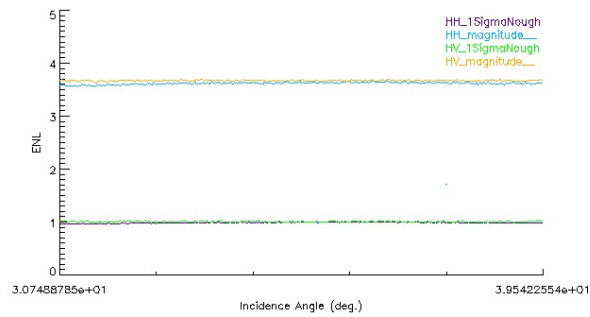
Figure 3.2 (a) (b) come out from multi-look processed products with 4 looks on range direction and 2 looks in azimuth direction, and (c) (d) come out from single look products. It seems that the sigma nought values perform at look numbers given by the product description, while the magnitude detected data performs with an ENL about 4 times as that of sigma nought, i.e., the sigma nought data suffers from more speckle than the magnitude data. By the horizontal axis, the ENL of HV channel stably hold on with a value with slightly change, while it usually has a lower ENL for HH channel in lower incidence angle, i.e. the near range of the swath, and the difference between near range and far range is bigger for SCW products than SLC products, since the wide swath has a span of 7 degree of longitude. An IDL programme with GUI has been built as a tool for this work, in which the ENL of the sub images could be marked with color, showing the distribution of ENL on a user specified area, as Figure 3.3. The ENL maps for all the data could be easily worked out.



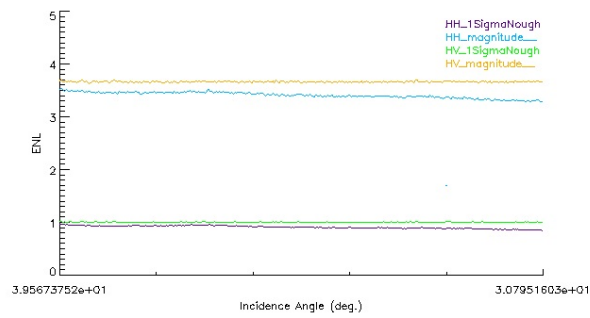
(a) azimuth averaged ENL of data A



(b) azimuth averaged ENL of data B

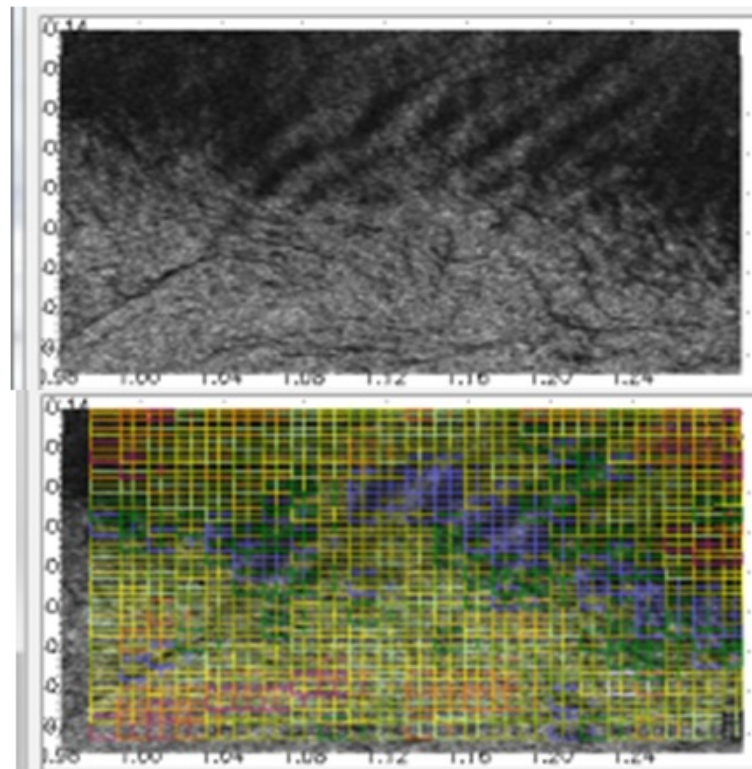


(c) azimuth averaged ENL of data C1



(d) azimuth averaged ENL of data D2

**Figure 3.2** — ENL of ABCD magnitude vs. sigma nought for HH and HV, averaged in azimuth direction

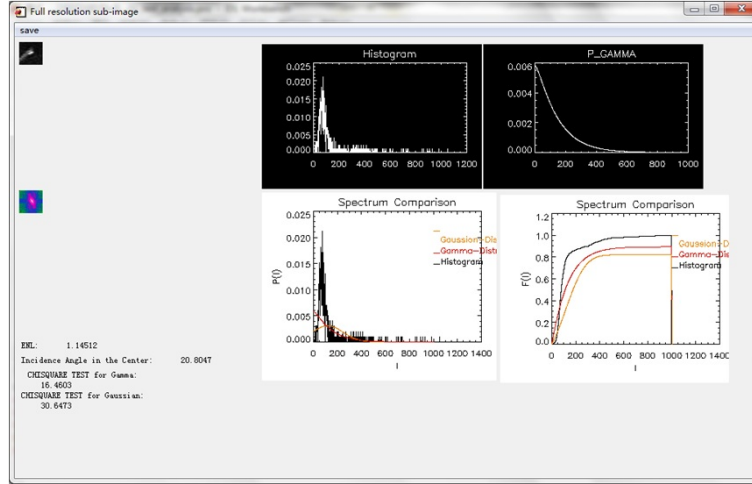


**Figure 3.3** — GUI presents the ENL distribution for a sub image, with the rainbow color showing the ENL map from a low value of blue from the slick areas to a high value of red by the homogeneous area. Sub image size of  $473 \times 473$  pixels, center: 1.1271450E, 40.058058N, center incidence angle: 23.7285 deg.

Statistical properties of sea-clutter are of interest to radar designers for the prediction of probability of detection and probability of false alarm. In radar applications, goodness of fit of clutter statistics to a model is important mainly in the low probability of false alarm region. Standard statistical tests such as the Chi-square goodness of fit test are of limited use for clutter data [138, 143]. For the modified chi-square test, set  $K=50$ , boundary of test region is where the probability of false alarm less than 0.1. The modified Chi-square result for the sub image of Figure 3.3 as the Table 3.3. It was found that the ENL of the whole sub image is effected mainly by the ship signature, and the Gamma distribution always fit better than Gaussian distribution in both polarization of magnitude data and sigma nought data.

### 3.2.2 Generalized K motivated by ENL analysis

ENL maps for all the data had been worked out, from which we can find local areas with large range of data value, since the image scenes is mainly over the coastal area, large area of slicks, ships, etc, where ENL turns to be a minimum value at the edge of signatures [145]. To set different size of sub image for ENL computing could identify whether it is a single target or a large area of sea surface phenomena. Sub images with ships are investigated by sub images

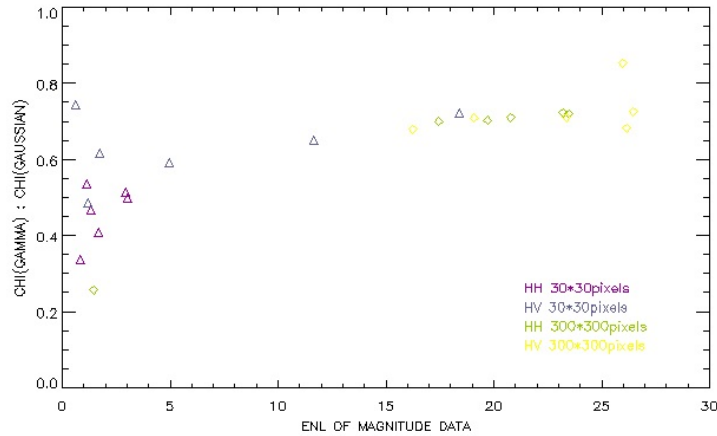
**Table 3.3** — Modified Chi-square test

Center: 0.80935087E, 38.932451N

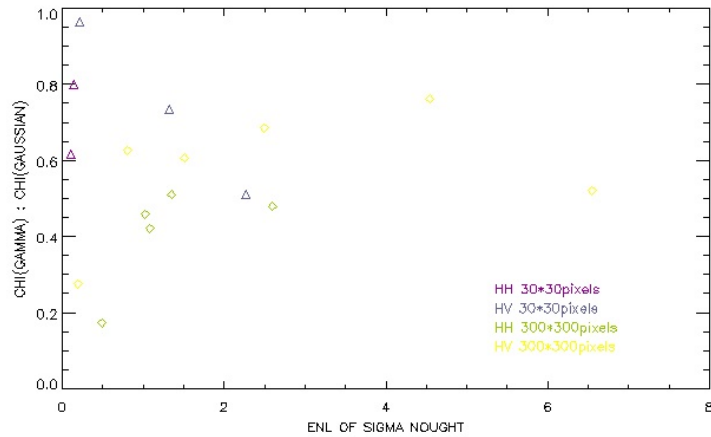
Incidence angle: 20.80470 deg., Size: 30 × 30 pixels

SB7	Magnitude HH	Magnitude HV	Sigma0 HH	Sigma0 HV
Min value	305	132	0.000215842	0.0000401194
Mean value	2166.8629	932.92820	0.020911358	0.0037265709
Max value	16069	8621	0.598286	0.172445
ENL	1.14512	1.18036	0.141585	0.0707068
$\chi_m^2$ Gaussian	30.6473	38.7491	49.1862	54.6243
$\chi_m^2$ Gamma	16.4603	18.8614	39.3768	52.3360

size of 30 × 30 pixels and 300 × 300 pixels. To see the goodness of Gamma distribution fitting the SAR imagery, a ratio of Gamma distribution to Gaussian distribution over the  $\chi_m^2$  value is plot in Figure 3.4, the smaller of the  $\chi_m^2$  the better fit. With the horizontal axis of the ENL value, figure 3.4 indicates that Gamma distribution performs better than Gaussian at the lower value of the ENL, i.e., where has a heavy contaminated area. The advantage of Gamma distribution is especially overwhelming for the magnitude data. For the sigma nought data, Gamma distribution has not a much clear advantages over Gaussian distribution. Gamma distribution performs better at smaller size of sub images when using magnitude data, while a bigger size of sub image would be better for Gamma distribution when using sigma nought data. Ferrara et al. [129] did the similar analysis, and an indicator of homogeneity by ENL was used to form a generalized K distribution.



(a)



(b)

**Figure 3.4** — Test ratio of Gamma over Gaussian as function of ENL, (a) for the magnitude Gamma distribution performs better than Gaussian at the lower value of the ENL, i.e., where has a heavy contaminated area. (b) for sigma nought the advantage of Gamma distribution has not clear advantages over Gaussian distribution.

### 3.2.3 Polarization and non-polarization contributions over the sea surface

Although the contrast parameter,  $\gamma$ , of the surface considered the finer structures in terms of correlate and non-correlate, it resolved the problem still remains by a scale of sub-image, where a region of interests (ROI) should be selected priorly. Other improvements such as  $G$  distributions, considered the detections as backscatter multiplied by speckle contributions. We will not deny this approach, just considering about its general success, but we now reconsider this problem by approach of more physically decomposition of scattering mechanisms, i.e., Bragg and Scalar contributions. The reasonability of this reconsideration relies on the fact that the sea surface is never static hence the speckle phenomenon appearing on the ocean scenes envoys different information from that on the land scenes.

Furthermore, the priority of polarization decomposition of single pixel makes difference from the detection on 2-D sub-image scale to the detection within single pixel. By the pixel scale, with a brief recall of Chapter 2, we decomposed radar scattering matrices into Bragg and Scalar contributions physically. The decomposition is an iteration initiated with the radar incidence angle and then controlled by a local incidence angle which is function of co-polarization and cross-polarization. Based on these developments and testing, a strategy has been refined to analyze the signature of different features, to retrieve wind seas and sea swell parameters, as well as slick areas, ships, oil rigs, such non-polarized targets that may be buried in the Scalar contributions.

### 3.2.3.1 Polarized- $K$ distribution

For polarimetric SAR, the single-look SLC data can be represented by a scattering matrix,  $S$ , while the multi-look processing of scattering matrix could not be the simple average, since the vector summation of random complex numbers obeying circular Gaussian is still complex circular Gaussian[1], but should turn to the covariance or coherency matrix, which are the statistical average introduced in Chapter 1. Without loss of generality, we will present polarimetric data, both single- and multi-look, using the coherency or covariance matrix in the following. After carefully estimating polarimetric scattering coefficients for both Bragg and Scalar contributions, we then proposed a sea clutter model, polarized- $K$  ( $Pol - K$ ) distribution, which describes quite the real sea surface.

We decomposed Bragg and Scalar scattering as dealing with single scattering respectively, for each pixel, hence the covariance matrix  $C$  or coherency matrix  $T$  has one single non-zero and non-negative real eigenvalue. The eigenvector represents scattering process, and this eigenvalue relates to its magnitudes [1]. This decomposition gives the probability of weighting each pixel to be Bragg or Scalar. The flowchart in Figure 3.5 describes this strategy. Moreover, the reciprocity property satisfied by the equal cross-pol of both Bragg and Scalar respectively promise the simple representation of  $T_3$  and  $C_3$  for the coherency and covariance matrices. For pure target, the single non-zero eigenvalue  $\lambda$  is equal to the Frobenius norm of the unit target vector  $u$  and corresponds to the span of the associated scattering matrix [1], i.e.,

$$\lambda = S_{HH}^* S_{HH} + S_{HV}^* S_{HV} + S_{VH}^* S_{VH} + S_{VV}^* S_{VV} = span(S) \quad (3.27)$$

where  $S = \{S_{br}, S_{sa}\}$  corresponding to  $\lambda = \{\lambda_{br}, \lambda_{sa}\}$ , could be the scattering matrix for either Bragg or Scalar contribution.

The derivation of  $Pol - K$  distribution stems from Wishart distribution (c.f. Equation 3.17 in Section 3.1.1.4) which is based on the circular Gaussian assumption, and wherein the complex covariance matrices  $\Sigma_z$ , defined in Equation 3.6, is the average of complex

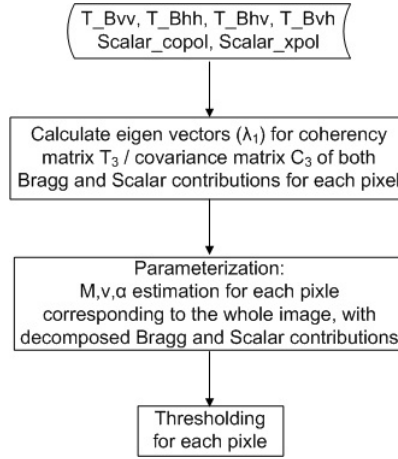


Figure 3.5 — Pol-K detection

covariances, i.e., the scattering coefficients, of each complex measurement, hence different from the covariance matrix  $C$  defined in Chapter 1. Alternatively, for each single-look Sinclair matrix  $S$ ,  $\Sigma_z$ , defined in Equation 3.6, is the total scattered power which is called span,

$$\Sigma_z = S_{HH}^* S_{HH} + S_{HV}^* S_{HV} + S_{VH}^* S_{VH} + S_{VV}^* S_{VV} = \text{span}(S) = \text{Tr}(C) = \text{Tr}(T) \quad (3.28)$$

A simple analogue is to rewrite the GK distribution of Equation 3.23 into form of eigenvalue  $\lambda$  of polarimetric covariance matrix  $C_3$  / coherency matrix  $T_3$ ,

$$P_N(\lambda) = \frac{cb/\sqrt{\lambda}}{\Gamma(M)} \left( \frac{b\sqrt{\lambda}}{2c} \right)^M K_{(M-1)}(cb\sqrt{\lambda}) I_0 \left( \frac{b\sqrt{\lambda}}{2\sqrt{M}} \alpha \right) \quad (3.29)$$

where  $\lambda = \{\lambda_{br}, \lambda_{sa}\}$  could be the eigenvalue of the covariance matrix for either Bragg or Scalar contribution, with the three parameters, i.e.,  $M$ ,  $2\sqrt{M}/b$  and  $\alpha$ , inherited from GK, and  $I_0$  is the first kind modified Bessel function of 0th order. Before the completion of *Pol-K* modelling, the parameterization should be specified.

### 3.2.3.2 Parameterization

The *Pol-K* distribution describes quite the real sea surface by considering the ratio of Bragg over Scalar contributions, with polarimetric scattering coefficients estimated for both Bragg and Scalar contributions. Thus the parameterization here is different from those used in modelling the averaged radar measurement, but considering the fine details within single pixel, where the two contributions have been decomposed. The basic model for the K-family consisted in Equation 3.19 could be decomposed into an addition,

$$\xi(r, t) = e^{j\omega t} \left( \sum_{i_b=1}^{N_b} B_{ib}(r, t) e^{j\varphi_{ib}(r, t)} + \sum_{i_{sc}=1}^{N_{sc}} S_{c_{isc}}(r, t) e^{j\varphi_{isc}(r, t)} \right), \quad (3.30)$$

as in Figure 2.9(a) and 2.9(b). With the three assumptions described in Section 2.3, what we care about is the summation of Bragg and Scalar respectively, which result in only two components as in Equation 2.31.

### 1. Shape parameter $M$

The shape parameter  $M$  is a real and non negative parameter which indicates the departure from the exponential model of a fully developed speckle, as a result of the bunching phenomena [41, 56], which is not neglectable for pixel resolution as fine as the longer wavelength. The bunching phenomena can be included in the random walk in Equation 3.19 as well as 3.30, taking the scatter population  $N$  (in Equation 3.19 is  $N_b + N_{sc}$ ) locally Poisson, which is unconditional integrated with a Gamma distributed local mean and becomes the negative binomial (NB) distribution ruled by the non-negative bunching parameter  $\nu$  [146],

$$p(N) = \binom{N + \nu}{N} \left( \frac{\nu + 1}{\bar{N} + \nu + 1} \right)^{\nu+1} \left( \frac{\bar{N}}{\bar{N} + \nu + 1} \right)^N \quad (3.31)$$

where  $\bar{N}$  is the mean number of  $N$ . It could be clear from the NB model that the bunching effect introduced an additional number of scatterer,  $N + \nu + 1$ , instead of the real population of scatterers,  $N$ , and the Equation 3.31 gives the probability for the set of  $N$  scatterers with the presence of  $\nu$  of them to be strong ones. As  $M = N(\nu + 1)$  gets larger, the NB distribution tends to a Poisson distribution and the K-distribution becomes an exponential model. According to Equation (12) and (28) in [125], with the assumption of statistical independence of  $\{a_i\}$  from  $\{\varphi_i\}$  in Equation 3.19,  $M$  could be identified with  $2N_{eff}$ , when the scatterer population  $N$  is asymptotically large, and  $N_{eff}$  is defined to be a mean 'effective' number of scatterers,

$$N_{eff} \equiv \frac{N \langle a^2 \rangle^2}{\langle a^4 \rangle} \quad (3.32)$$

where  $a$  is the form factor in Equation 3.19 governing the angular distribution of radiation from the scatterers, and  $\langle a^m \rangle$  is the  $m$ th moment of  $p(a, r)$  in Equation 3.20.

### 2. Slope parameter $2\sqrt{M}/b$

The slope parameter is related to the mean intensity of the local backscattered field,

$$\frac{2\sqrt{M}}{b} = \sqrt{E(\sigma)} \quad (3.33)$$

where  $E(\sigma)$  is the mean RCS of the scattered field.

### 3. Phase parameter $\alpha$

The phase parameter  $\alpha$  describes the departure from the uniform distribution of the

phase [127, 126], biasing the possibility of the phase  $\varphi$  in Equation 3.19 by the von Mises form

$$p(\varphi) = \begin{cases} \frac{\exp(\alpha \cos \varphi)}{2\pi I_0(\alpha)}, & -\pi < \varphi < \pi \\ 0, & \text{elsewhere} \end{cases}, \quad (3.34)$$

where  $I_0$  is the first kind modified Bessel function of 0th order, comparing with the uniformly distributed phase  $\varphi$  in Equation 3.19 as

$$p(\varphi) = \begin{cases} \frac{1}{2\pi}, & -\pi < \varphi < \pi \\ 0, & \text{elsewhere} \end{cases}. \quad (3.35)$$

In Rice distribution,  $\alpha$  deals with the presence of a dominant specular component [128].

### 3.3 Availability of Pol – K distribution

The basic quantity measured by a coherent radar system at each pixel is a pair of voltages in the in-phase and quadrature channels [36], then the real and imaginary parts of the complex signal are derived by mixing (detect) the received signals with in-phase and quadrature local oscillators, hence the labelling with I and Q [42]. Earlier instruments utilise a square law detector to restore the detected radar returns (detected voltages) as intensities. For most applications the representation of the image magnitude is enough, i.e. square roots of detected radar returns (envelope of detected voltages), and so called amplitude. If the image has been power detected, the peak intensity is the maximum pixel value in the main lobe of the impulse response function (IRF) [147]. Many of distributions of univariate laws have been used to describe SAR data, assuming the multiplicative model, such as Rayleigh, Square Root of Gamma, Exponential, Gamma, and the class of the  $K_I$  distribution. The adequacy of these distributions depends on the data format (amplitude, intensity, complex etc. and the number of looks) and the homogeneity of the data. Here it must be stressed that, although referring to [148] which said that multiplicative model is a very common statistical model for noisy polarimetric SAR data, assuming the backscatter obeys a generalized inverse Gaussian distribution, while the speckle noise follows a Wishart distribution, and although the assumption, that the the coherent illumination on a surface with roughness of the order of a wavelength may cause speckle as a multiplication of the backscatter and the speckle, has been greatly acknowledged [149], it has been never to say that speckle has a physical source for radar received signal, let alone for noise.

The total data set, including Table 2.1 and 3.1, is analysed to test the Pol – K distribution introduced in the end of the former Section 3.2.

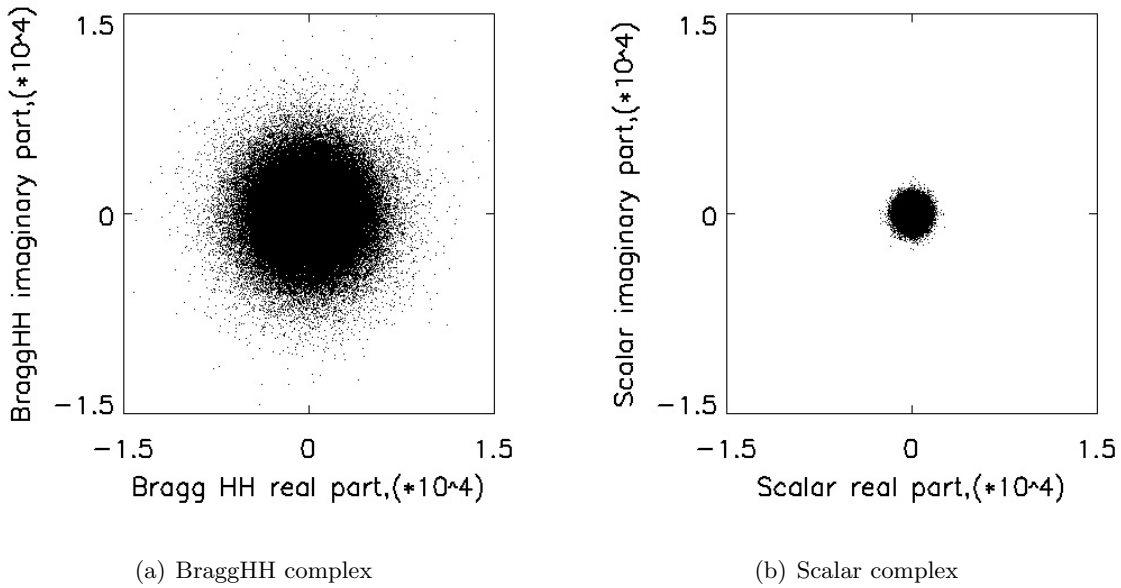
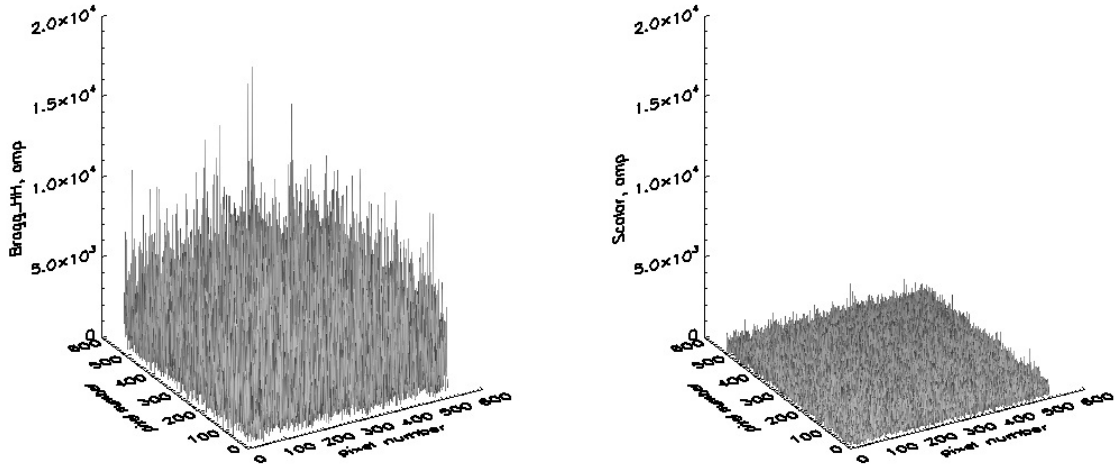


*Figure 3.6* — SLC decomposition and their circular Gaussian distribution

### 3.3.1 Single look complex data

The decomposition of Bragg and Scalar from the SLC full polarimetric data is also single look complex data. The probability density function for real and imaginary part should not be other than the circular Gaussian which was supposed for the large number of randomly distributed scatterers. Figure 3.6 and 3.7 denotes a sub image of  $512 \times 512$  pixels decomposed into the two scattering contributions at the 6th iteration, shown as the circular Gaussian as well as the amplitude. The incidence angle was 27.06 deg. and the wind speed was 17.5 m/s for that day of 23, April 2012, reads from Table 2.1.

Complex data exists only when single look detection has been carried out. For multi-look processing, complex values from the inverse FFT does not reduce speckle, but only the sum of iid hence still single look. In SLC products, the measurements result in a matrix of scattering coefficients, each image pixel is represented by a complex (I and Q) magnitude valued, dimensionless numbers that describe the transformation of the transmitted EM field to the received EM field for all combinations of transmit and receive polarization [116]. No interpolation into ground range coordinates is performed during processing for SLC image products, and so the range coordinate is given in radar slant range rather than ground range [99, 94]. Pixel spacings are determined by the radar range sampling rate and pulse repetition frequency (PRF). The processing for all SLC products covers a single look in each dimension using the full available signal bandwidths.



(a) BraggHH amplitude

(b) Scalar amplitude

Figure 3.7 — SLC decomposition and their amplitudes

### 3.3.1.1 Second order statistics

The variation, as second order statistics, of the complex data,

$$\text{var}(\xi(r, t)) = E(\Re(\xi(r, t))^2) + E(\Im(\xi(r, t))^2) - E(\xi(r, t))^2 \quad (3.36)$$

turns out to be

$$\text{var}(\xi(r, t)) = E(\Re(\xi(r, t))^2) + E(\Im(\xi(r, t))^2), \quad (3.37)$$

since the mean complex data  $E(\xi(r, t)) = 0$ , as shown in Figure 3.8, wherein is the histograms for BraggHH and Scalar at the 6th iteration, as well as HH. Here comes the relation of variation of the complex data to the radar cross-section, formerly introduced and defined to be equal with the square of the envelope of the field,  $\sigma(r, t) \equiv |\xi(r, t)|^2$ .

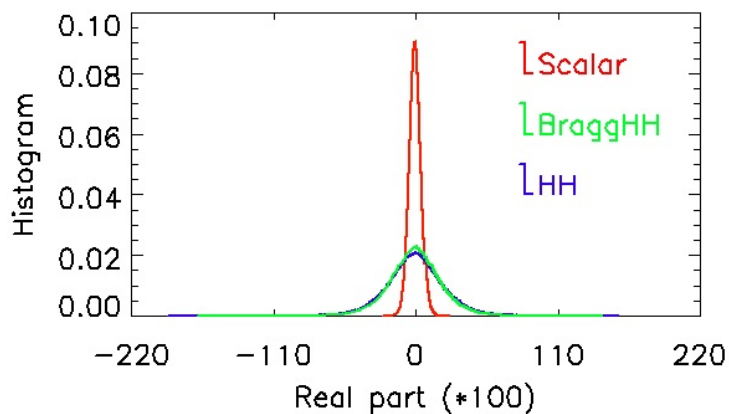
The amplitude of the backscattered wave in Equation 3.30 could also be decomposed into Bragg and Scalar contributions,

$$A^{pq} = |\xi^{pq}(r, t)| = |B^{pq} + S c^{pq}|, \quad (3.38)$$

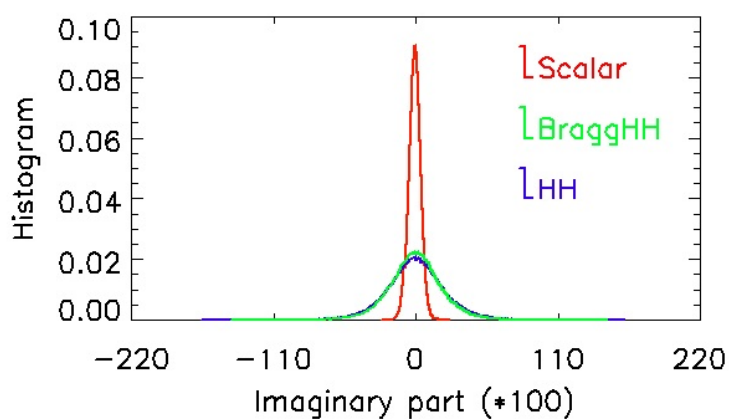
providing the independence of Bragg and Scalar contributions, and the same for intensity of single look pixel,

$$I^{pq} = |\xi^{pq}(r, t)|^2 = |B^{pq} + S c^{pq}|^2, \quad (3.39)$$

where  $p, q \in \{H, V\}$  and  $B^{pq}$  and  $S c^{pq}$  are the complex polarization components in Equation 2.31. Figure 3.9 shows the histograms for VV/HH, BraggVV/HH and Scalar, at the 6th iteration. It is interesting to see the abstraction effect of scalar from Bragg contributions for the VV-pol, while the summation of scalar and Bragg for the HH-pol.



(a) Real part

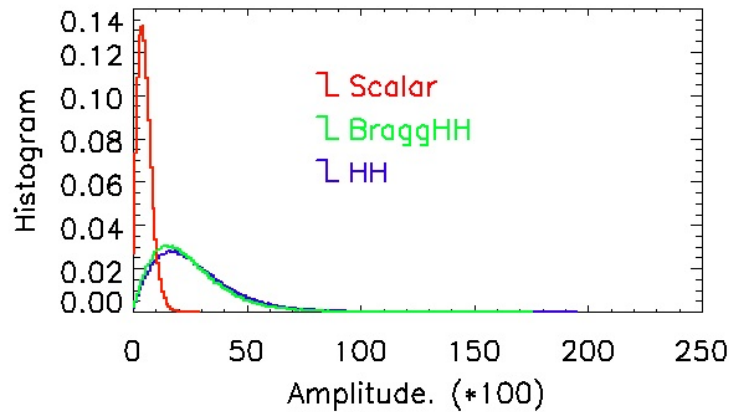


(b) Imaginary part

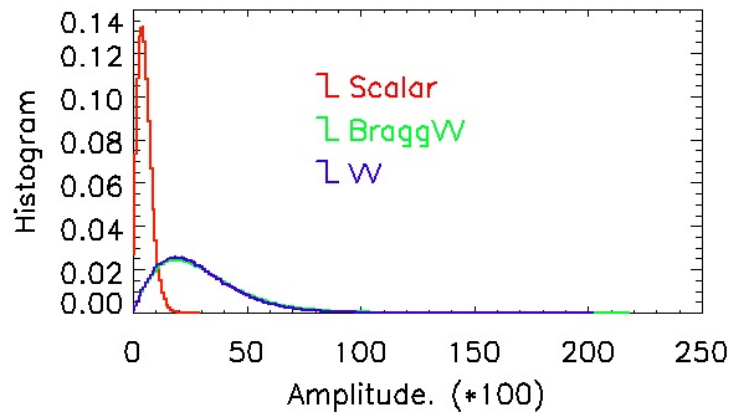
*Figure 3.8* — Histogram of real and imaginary parts of BraggHH and Scalar at the 6th iteration

### 3.3.1.2 Sub-band decomposition

Recognizing scenes in a single look meter-resolution SAR imagery requires the capability to identify relevant signal signatures in condition of variable image acquisition geometry, arbitrary object pose and configuration. Among the methods to detect relevant scatterers in SAR images, we can mention the internal coherence [150]. The SAR spectrum splitted in azimuth generates a series of images which preserve high coherence only for particular object scattering. This is the principle of multi-look processing method, which can be used on SLC data by a sub-band decomposition technique. For imageries with sense of ocean, the physical base is the mapping of ocean wave motion to the SAR imagery on the azimuth direction by Doppler frequency. From Figure 3.10 to 3.12 gives an example for the sub-band processing, the



(a) HH-pol



(b) VV-pol

**Figure 3.9** — Histogram of amplitude for VV/HH, BraggVV/HH and Scalar, at the 6th iteration

sub-image is the same one from the day of 23, April 2012. Furthermore, the RADARSAT-2 SAR antenna design allows the antenna to be partitioned into two halves along the direction of flight and thus permits two closely spaced observations to be made of the same scene to observe temporal changes [151].

As introduced in the former Section 3.2, the Equivalent Number of Look (ENL) is a parameter of multi-look SAR images, which describes the degree of averaging applied to the SAR measurements during data formation and postprocessing. [152] For the SLC sub-image in Figure 3.10 and the 2-look processed sub-image in Figure 3.12, the ENL is 0.59648025 and 0.99622768 respectively. While the coefficient of variation  $\gamma_{SI}$  is the reciprocal of squared ENL, 1.2947978 and 1.0018915, and  $\gamma_{SA}$  is  $0.61222398 = 1/\sqrt{2.6679601}$  and  $0.47314656 =$



*Figure 3.10* — SLC subimage (VV)

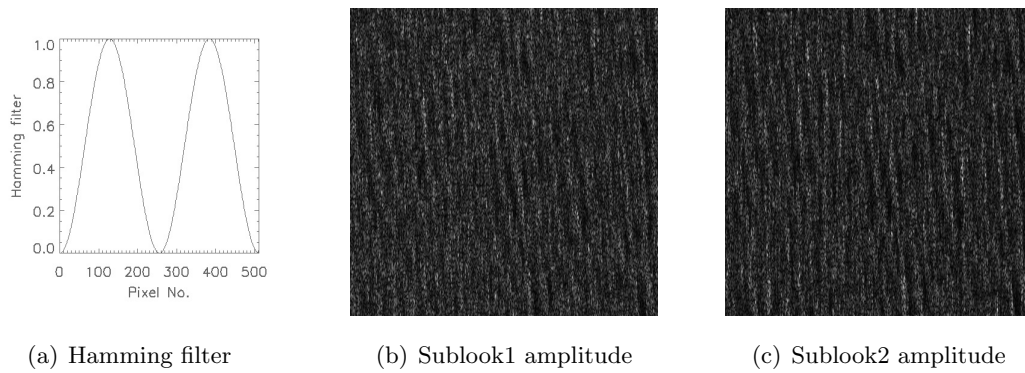


*Figure 3.11* — Sublooking process



*Figure 3.12* — 2-look processed from Figure 3.10

$1/\sqrt{4.4669246}$  respectively, meaning the amplitude has a less fluctuate from the mean than the intensity.

### 3.3.2 Intensity detected data

The use of the word 'intensity' is by analogy with measurements at optical wavelengths and is synonymous with power or energy [36]. The intensity of the detected field defined by

$$I(r, t) = |\xi(r, t)|^2 = \Re(E)^2 + \Im(E)^2 \quad (3.40)$$

had discussed as a variable change from the complex data in the former subsection. More generally, intensity and amplitude detected data is multi-look processed, for reducing the variation around the estimate for  $\sigma$  or  $\sigma^0$ .

For the multi-look processed intensity imagery,  $N$ -look intensity of each pixel [1, 134],

$$I(r, t) = \sum_{i=0}^N (\Re(E)_i^2 + \Im(E)_i^2) \quad (3.41)$$

### 3.3.3 Amplitude detected data

If the image has been power detected, the square root of the intensity is the amplitude. An extension of the complex-Gaussian distribution considering about a single large scatterer (diffuser) with deterministic amplitude embedded in a rough surface is the Rician distribution, which comes from Rician communication channel and had been applied to radar measurements [35, 130, 153].

## 3.4 Discussion and conclusion

According to the principle equation (3.19) of K-family, our decomposition has a consistency with K-distribution concerning the treatment on independent scatterers.

The shape parameter  $M$  determines the shape of 'tail'. A higher value of  $M$  corresponds to a shorter 'tail' of the PDF. The phase parameter  $\alpha$  determines the shape of 'height'. A higher value of  $\alpha$  corresponds to a lower peak of the PDF. When  $\alpha = 0$ , Pol-K degrades to K distribution, i.e., K is a special case of Pol-K distribution. For a  $1024 \times 1024$  sub-image, given the same parameters as shown in table 3.4,

**Table 3.4** — Pol-K parameters

for Bragg contribution		for Scalar contribution	
parameter	estimate	parameter	estimate
$\sqrt{E(\lambda_{bra})}$	4048.53	$\sqrt{E(\lambda_{sca})}$	1816.98
M	18.28	M	16.75
b	0.002	b	0.005
$\alpha$	1.85	$\alpha$	2.75

the comparison of Pol-K vs. K distribution are shown in figure 3.13. Although K distribution describes the shape of 'tail' as well as Pol-K does, there is an overestimate for the 'height' of the peak. This disadvantage does rarely matter with the application such as ship detection, where the problem focus on the 'tail' part of the PDF. The merit of Pol-K will be found for an application such as oil slick detection.

In this chapter, we proposed a generalized K motivated by ENL analysis, the Polarized-K distribution, which is established by the decomposition introduced in chapter 2. The principle

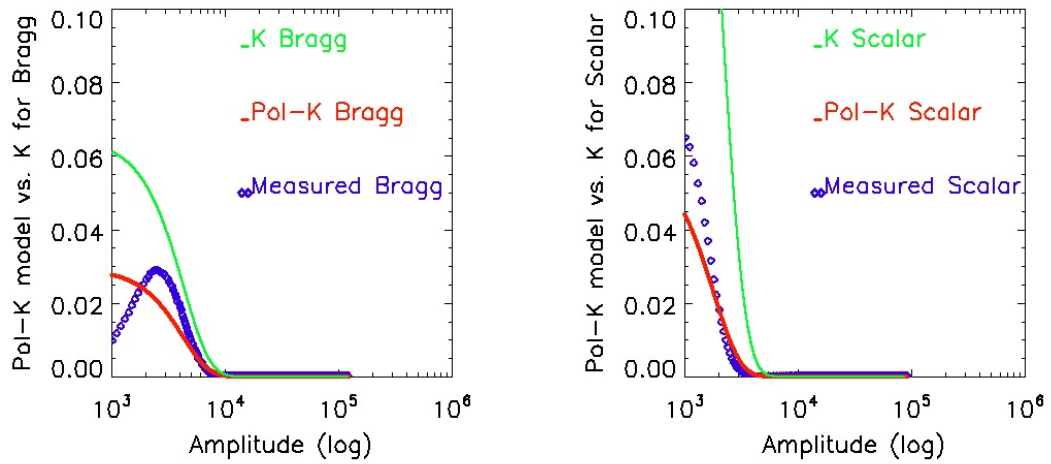


*Figure 3.13* — Comparison of Pol-K vs. K distribution for a 1024\*1024 sub image

is based on the physical generation of speckle, leading to separated modellings for each of the different scattering mechanisms, i.e., Bragg contribution and Scalar contribution. This is different from traditional modellings for speckle, where the latter are usually considering the direct radar measurements as the single variable, and the physical information inside pixel areas is ignored.



---

# 4 Target detection

*From the number of trials it happens and fails in a certain number of trials, without knowing any thing more concerning it, one may give a guess whereabouts it's probability is, and, by the usual methods computing the magnitudes of the areas there mentioned see the chance that the guess is right. And that the same rule is the proper one to be used in the case of an event concerning the probability of which we absolutely know nothing antecedently to any trials made concerning it, seems to appear from the following consideration: viz. that concerning such an event I have no reason to think that, in a certain number of trials, it should rather happen any one possible number of times than another.*

*An essay towards solving a problem in the doctrine of chances, by Thomas Bayes, published in 1763 by Richard Price*

As early as the Mercury programme, astronauts experienced the low orbits Earth observation. Then photographs taken by the Gemini programme gave the first indications that usable information about the oceans could be obtained from spacecraft. Skylab provided dramatic photographs of internal waves, and later the internal wave solitons were discovered for the first time by the Apollo-Soyuz flight in 1975, with the ground truth measurements from the experience of Skylab. Followed that, microwave sensor and radar altimeter had been equipped on the first sea satellite SEASAT. Attributed to the plentiful SAR imageries over the ocean, imaging mechanisms for sea surface phenomena have been studied by a group of oceanographers in the early 1980s. At that time, ship targets could be found only by their wakes[154], due to the low imaging resolution that could not resolve a ship target beyond one single pixel. One of the objectives of those studies aimed at the automatic interpretation of SAR

imageries. However, it was till 1993 when the general concept of automatic target recognition (ATR) was introduced by MIT scientists [155]. The principle of ATR technique is that the target detection depends on two fundamental radar parameters [44], i.e., the target-to-clutter ratio and the standard deviation of the background clutter.

To realize ATR for target detection using SAR imageries, statistical detectors had been investigated. One of the most recommended algorithm is the cell averaging CFAR detector, somewhere also referred to as the power ratio detector (PR), which considers the statistically modelling of the background, and then looks for pixels with a low probability of belonging to the background. Besides of the modelling of the background, likelihood ratio test detectors (LRT) consider also the modelling of the target for optimal detection [54]. Considering about the optimal detection, one aspect of the radar waveform that requires particular attention is its polarisation and the dependence on polarisation of the back-scattered radar signals, which can be represented by the polarisation scattering matrix [42]. Departing from Kennaugh's pioneering introduction of polarization into radar polarimetry in 1952, polarimetry has been utilized on radar backscattering mechanisms with different target parameter sets [13, 156, 157], which have already shown their great power in the domain of classification. Based on Huynen's parameterization [13] of a scattering matrix, Dilsavor et al. [158] proposed a family of polarimetric generalized likelihood ratio tests (PGLRTs) for terrain targets. Freeman and Durden [159] reported that three-component scattering model is successfully applied to decompose mixed scattering components in measured POLSAR data. However, despite of the greatly use and successful of target decomposition (TD) theory in terrain target classification, the sea surface has still been simply treated as 'kind of Bragg' scatter.

As described in chapter 2, the ocean surface has much more fluctuation than what it had been expected with comparison to the surface over the land. In fact, before the launch of the first polarimetric SAR satellites, such as Envisat which launched in 2002 being capable of imaging in dual-polarization, and RADARSAT-2 which launched in 2007 with a quad-polarization imaging capability, there had been already plenty of investigations about the capability of polarimetric data on ship detection, using air-born SAR data [160, 61]. Daniel et al. [161] discussed different cases from fully polarimetric data to single HH polarization data, from 1-ft resolution data to 1-m resolution data, for the performance of the discrimination algorithm. It was found that at operational satellite SAR incidence angles ( $< 60^\circ$ ) there is a significant improvement of ship-sea contrast when the full polarimetric information is used instead of the single channel polarization information (HH, VV, or HV) [162]. Jeremy et al. [53] suggested that with polarimetric data, ship detection algorithms will be developed with a false alarm rates reduced by correctly classifying the false alarms.

So far, the polarimetry technique benefit to ocean remote sensing mainly on retrieving sea surface slope from the orientation angle estimated on the L- or P-band SAR polarization

imageries [1]. We used polarimetric sea surface slope estimate in Chapter 2 to decompose the sea surface scattering mechanisms. Following this decomposition, a Bayesian detector relates to man-made target detection over the sea surface, which is based on generalized LRT and therefore named as TD-GLRT has been worked out. Since sea spike as the general source of false alarms had already been analysed as the sea surface signature as in Chapter 2, what we will analyse in the TD-GLRT approach is the scattering relates to scalar.

## 4.1 Polarimetric Bayesian detectors

The cross-polarized backscattering received by RADARSAT-2 SAR enables target detection at smaller incidence angles. Research works indicated also that the HH/HV combination provides optimized target detection over a greater range of incidence angles than those of RADARSAT-1. In review of state-of-art for ship detection [54], the generalized likelihood ratio test (GLRT) assuming the received signals as Gaussian distributed for polarimetric data (PGLRT) has been recommended by researches of a group of Italian scientists [163, 164]. In fact as early as 1994, Dilsavor et al.[158] proposed a family of polarimetric generalized likelihood ratio tests (PGLRTs), one PGLRT from which, designed for both Gaussian and K-distributed clutter with known covariance and unknown target amplitude, phase, and orientation angle about the radar LOS, gave a performance lying between those of the optimal polarimetric detector (OPD) and the polarization whitening filter (PWF).

### 4.1.1 OPD

Novak et al [165] derived two advanced detectors, OPD and polarimetric matched filter (PMF), to make use of polarimetric radar information in the detection and discrimination of targets in a ground clutter background. Compared with simpler detectors using only amplitude information, OPD and PMF illustrated an advanced performance. OPD is derived in an ideal situation where the parameters  $(\sigma, \epsilon, \gamma, \rho)$  and target-to-clutter ratio  $(T/C)_{in}$  are exactly known, and hence it yields the best possible probability of detection ( $P_D$ ) for a given false alarm probability ( $P_{FA}$ ). Unfortunately, the ideal situation is usually not satisfied in practical.

### 4.1.2 PWF

PWF is another extreme case with completely unknown target [166], and hence is not optimal. Processing the complex polarimetric measurements into an intensity image as a single channel measurement, PWF will find an optimal weighting transformation to achieve the minimum coherent speckle for homogeneous clutter characterized by fully polarimetric Gaussian clutter

model. The approach is evaluated via the ratio of the standard deviation of the image pixel intensities to the mean of the intensities, i.e., the ENL. The intensity ( $I_{PWF}$ ) results from PWF could be expressed as

$$I_{PWF} = X^{T*} \Sigma_c^{-1} X, \quad (4.1)$$

where the complex polarimetric measurement

$$X = \begin{bmatrix} HH \\ HV \\ VV \end{bmatrix}. \quad (4.2)$$

and the covariance of  $X$ ,  $\Sigma_c = E(X^{T*}X)$ , defined similarly as  $\Sigma_z$  in Equation 3.6. The minimum ENL of  $I_{PWF}$  achieved by PWF is  $-4.8dB$ .

### 4.1.3 PGLRTs

PGLRTs are parameterized by targets' amplitude, phase, and orientation angle about the radar LOS, i.e. the vector  $(m, \rho, \psi)$ . Those target parameters are unknown in many practical applications for the target modelling, but could be estimated by the detectors. It had been demonstrated that when the parameter vectors are known, PGLRT reduced to Polarimetric LRT (PLRT), which has equal performance with PMF, while if the parameter vectors are unknown, PGLRT equals to PWF. PGLRTs had been considered for fully polarimetric terrain responses [158] based on GLRTs.

According to Bayes criterion, the decision regions are defined by the statement as Equation (12) in [167] which be rewritten here

$$\frac{p_{r/H_1}(R/H_1)}{p_{r/H_0}(R/H_1)} \underset{H_0}{\overset{H_1}{\geq}} \frac{p_0(C_{10} - C_{00})}{p_1(C_{01} - C_{11})}, \quad (4.3)$$

where  $H$  and  $p$  represents the hypothesis and the probability respectively. The subscription 0 and 1 stands for the false and true of the hypothesis  $H$ , as well as the priori probabilities of the false and true exist in the real life, while the subscription  $r/H_0$  and  $r/H_1$  denotes the observed probabilities of the observation  $r$  provided the false and true happened respectively.  $C$  represents the cost of the decision, i.e., it cost  $C_{10}$  when you decide to be true when it is false in fact, and the rest can be assigned in the same manner. The left of the inequality is called the likelihood ratio and denoted by  $\Lambda(R)$ , and the right is threshold of the test and usually denoted by  $\eta$ . This Inequality 4.3 is a likelihood ratio test (LRT), when the likelihood ratio greater than the threshold, we should decide the observation  $r$  to be said as true, and vice verse. In the target detection using SAR imagery,  $H_1$  denotes truly to be the target while  $H_0$  denotes falsely to be the target hence to be the background, and simply to set the cost

for right decisions,  $C_{00}$  and  $C_{11}$ , to be 0, while the wrong decisions,  $C_{10}$  and  $C_{01}$ , to be 1, and obtain priori probabilities for the target and background by a false alarm rate.

To extent the hypothesis  $H$  with parameter(s), which would be one or more and will not simply be  $0 \rightarrow true$  or  $1 \rightarrow false$  but variate(s) within a set of values, i.e. in  $[min, max]$ , and to represent these parameters by a vector  $\Theta$ , the Inequality 4.3 will be extend as

$$\Lambda(R) = \frac{p_{r/\Theta_1}(R/\Theta_1)}{p_{r/\Theta_0}(R/\Theta_0)} \underset{H_0}{\underset{H_1}{\geq}} \eta, \quad (4.4)$$

In general case the function  $p_{r/\Theta}(R/\Theta)$ , which is a function of  $\Theta$ , is denoted as the likelihood function, and the maximum likelihood (ML) estimate is the value of  $\Theta$  at which the likelihood function is a maximum. If ML estimates are used in Inequality 4.4, i.e.,

$$\Lambda(R) = \frac{\max_{\Theta_1} p_{r/\Theta_1}(R/\Theta_1)}{\max_{\Theta_0} p_{r/\Theta_0}(R/\Theta_0)} \underset{H_0}{\underset{H_1}{\geq}} \eta, \quad (4.5)$$

is called a generalized likelihood ratio test (GLRT).

Further extensions of PGLRTs have the PGLRT used for multi-dimension parameter space in [168], and the PGLRT which is mainly focus on the terrain response of radar [169], as well as the one for slicks detection over the sea [170].

#### 4.1.4 TD-GLRT

Utilizing TD theorems, it is reasonable to model the polarimetric measurements into decomposed components, which may contribute both as the target and the background. Following the decomposition in Chapter 2 and the statistical analysis in Chapter 3, the Bragg contributes as the depolarized composite of and surface short waves and man-made target while the Scalar contributes as the polarized scatterings which is considered as the composition of target and wave breaking contributions. Thus for target detection, both Bragg contribution and Scalar contribution supply as the background, wherein the man-made target buried, and which could be modelled as

$$X_{br} = \begin{bmatrix} Bragg_{HH} \\ Bragg_{HV} \\ Bragg_{VV} \end{bmatrix} \quad (4.6)$$

and

$$X_{sc} = \begin{bmatrix} Scalar_{HH} \\ Scalar_{HV} \\ Scalar_{VV} \end{bmatrix}, \quad (4.7)$$

and finally to model the polarimetric measurement  $X$  as

$$X = \begin{bmatrix} HH \\ HV \\ VV \end{bmatrix} = X_{br} + X_{sc}. \quad (4.8)$$

The hypothesis used for Bayesian detection is considered as

$$\begin{aligned} H_0 : X &= X_{br}(wave) + X_{sc}(water) \\ H_1 : X &= X_{br}(target) + X_{sc}(target) \end{aligned} \quad (4.9)$$

If it is true for hypothesis  $H_0$ , the measurement  $X$  comes from the sea water, and the other hypothesis will be fit when  $X$  comes from a man-made target on the sea surface.

#### 4.1.4.1 Modelling the background

To implement the Bayesian test for hypothesis 4.9, the statistical modelling for  $X_{br}(wave)$  and  $X_{sc}(water)$  should be given,

$$p_X(X|H_0) = p_X[X|X_{br}(wave), X_{sc}(water)], \quad (4.10)$$

which are determined by the first and second order statistics of the Bragg and Scalar contributions from the ocean wave.

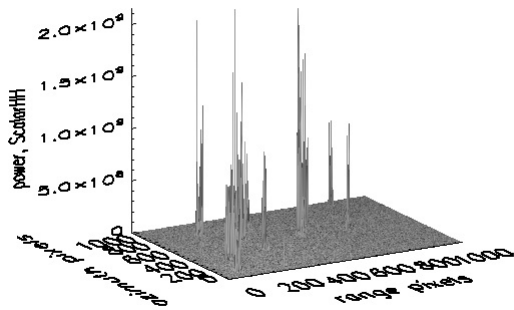
#### 4.1.4.2 Modelling the target

For an optimal detection, the statistical modelling for the target should also be given priorly. Considering about the difficulty in practical, we will model the target with its first and second order statistics, similarly to those for the background. The statistical modelling for  $X_{br}(target)$  and  $X_{sc}(target)$  should be given,

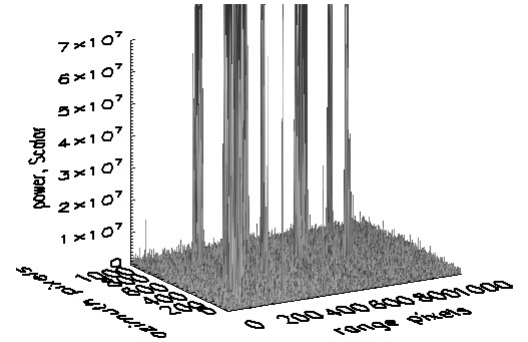
$$p_X(X|H_1) = p_X[X|X_{br}(target)], p[X_{sc}(target)], \quad (4.11)$$

which are determined by the first and second order statistics of the Bragg and Scalar contributions from the man-made target on the sea surface.

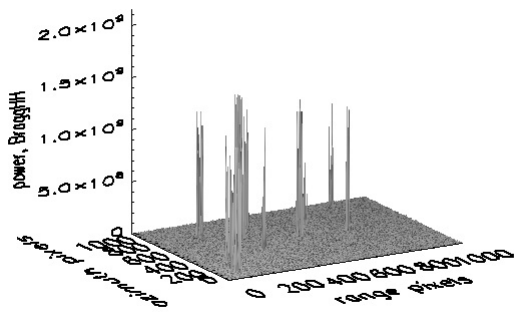
With the Scalar contribution decomposed from full polarization data besides Bragg contribution, what we will propose in this chapter is one generalized LRT (GLRT) using target decomposition (TD-GLRT). The hypothesis test has been given in inequation (4.9). It appears somehow like the multifamily LRT (MFLRT) [171], by separating the two hypotheses into four. But considering that both  $X_{br}(target)$  and  $X_{sc}(target)$  comes from target and both  $X_{br}(wave)$  and  $X_{sc}(water)$  comes from the background, the problem is still two hypotheses problem. The radar measurements vector  $X$  composites the total backscattering contributions of each pixel area by different polarization channels, and  $X_{sc}(target)$  denotes the electromagnetic coefficient for man-made target. The description 'water' specifies  $X_{sc}(water)$  could be considered as all together the specular or Rayleigh scatterer formed by the wave breaking processes, which all relate to water drops but not the wave, although by using the concept of Scalar, we did not specify which comes from the crest of the longer wave before it breaks or



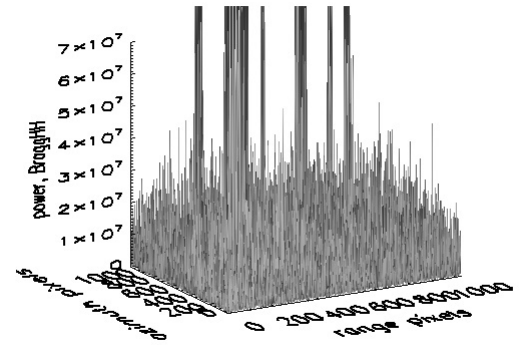
(a) Scalar power



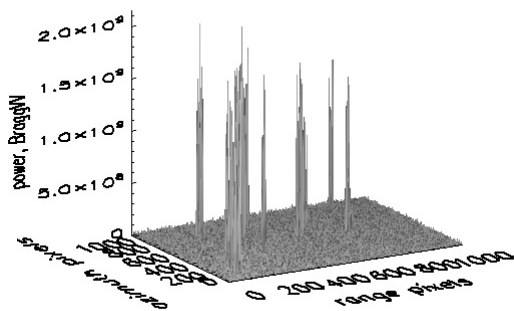
(b) Scalar power, zoomin



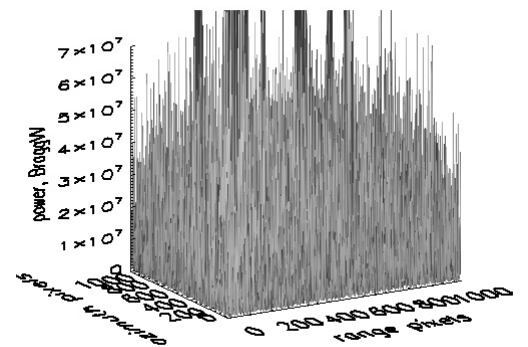
(c) BraggHH power



(d) BraggHH power, zoomin



(e) BraggVV power



(f) BraggVV power, zoomin

*Figure 4.1* — Bragg and Scalar ship subimage, Co-pol, 6th Iteration. The high target-background-ratio of Scalar contribution in comparison with those from Bragg contribution, especially when zoomed in (right column)

which comes from surface foams formed by wave breaking. It is easier to explain the physical meaning of  $X_{br}(target)$  and  $X_{br}(wave)$ , since it is considerable of the Bragg resonant scattered from man-made target and not mention to the sea surface Bragg wave. One prior knowledge of radar measurements should be noticed is that the energy from the wave should usually be much more than that from the water drops. This could also be illustrated in the coming plots in Figure 4.1.

Based on the above findings and understandings, the composite hypothesis for the sea surface water Scalar contribution equals that for the non-water scalar contributions, which says

$$\begin{aligned} H_0 : X_{sc} &= X_{sc}(water) \\ H_1 : X_{sc} &= X_{sc}(target) \end{aligned} \quad (4.12)$$

where  $X_{sc}$  is the Scalar measurement modelled as in Equation 4.13, and  $X_{sc}(water)$  and  $X_{sc}(target)$  could be estimated by the first and second order statistics,  $\Theta = [E(\sigma), \text{VAR}(\sigma)]$ , wherein is the first and second moment of the physical parameter, the scattering coefficient,  $\sigma$ . For amplitude, there is only difference between co-pol and cross-pol, i.e.  $|Sc^{HH}| = |Sc^{VV}|, |Sc^{VH}| = |Sc^{HV}|$  by our findings and assumptions in Chapter 2. At this point, Equation 4.13 could be simplified as

$$X_{sc} = \begin{bmatrix} \text{Scalar}_{co-pol} \\ \text{Scalar}_{cross-pol} \end{bmatrix}. \quad (4.13)$$

The parameter vector  $\Theta = [E(\sigma), \text{VAR}(\sigma)]$  are unknown at pixel scale but could be known as the whole image, hence at pixel scale to establish a GLRT detector with  $\Theta = [E(\sigma), \text{VAR}(\sigma)]$  could be selected for the whole image, and could be realized respectively as

$$\Lambda(X_{sc}) = \frac{\max_{E(\sigma_T)} \max_{\text{VAR}(\sigma_T)} p_{X_{sc}/E(\sigma_T), \text{VAR}(\sigma_T)}(X_{sc}/E(\sigma_T), \text{VAR}(\sigma_T))}{p_{X_{sc}/H_0}(X_{sc}/H_0)} \underset{H_0}{\overset{H_1}{\geq}} \eta, \quad (4.14)$$

where  $p_{X_{sc}/E(\sigma_T), \text{VAR}(\sigma_T)}(X_{sc}/E(\sigma_T), \text{VAR}(\sigma_T))$  denotes the likelihood function of radar measurement  $X_{sc}$  provided the man-made target radar coefficient  $\sigma_T$  has a mean of  $E(\sigma_T)$  and variation of  $\text{VAR}(\sigma_T)$ , which is equivalent to the probability function of radar measurement  $X_{sc}$ . The same manner are followed by  $p_{X_{sc}/E(\sigma_W), \text{VAR}(\sigma_W)}(X_{sc}/E(\sigma_W), \text{VAR}(\sigma_W))$ . But for  $p_{X_{sc}/H_0}(X_{sc}/H_0)$ , with the parameter fixed, denotes the probability function, which is equivalent to the likelihood function.

The merit of TD-GLRT lies in the use of scalar component  $Sc$  of radar measurement  $\xi = Bragg + Scalar$ , instead of using  $\xi$  directly, simplified the parameter vector  $\Theta$  and even to fix it for  $H_0$  as in inequation 4.14. The next step of this approach is to design a GLRT by replacing the unknown  $\Theta = [E(\sigma), \text{VAR}(\sigma)]$  with its ML estimate and setting up the LRT. Based on the ENL analysis, the estimation of  $\Theta = [E(\sigma), \text{VAR}(\sigma)]$  for background is established over homogeneous areas where the ENL is larger than those of heterogeneous areas, and the

latter is used to estimate  $\Theta = [E(\sigma), \text{VAR}(\sigma)]$  for the target. The narrow variation of Scalar background compared to Bragg and HH background could be find also in figure 4.2.

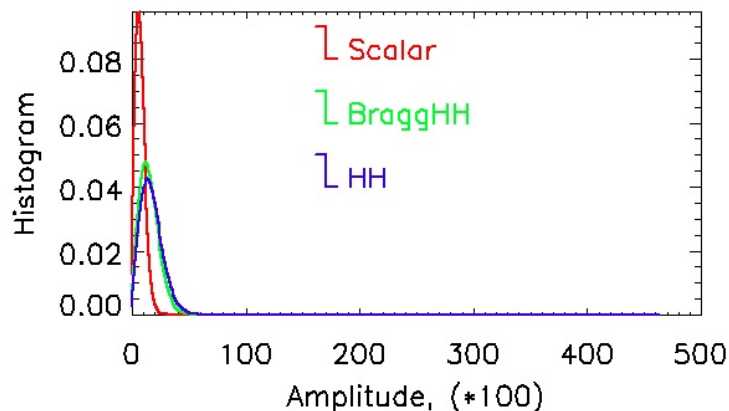


*Figure 4.2* — Amplitude histograms for Bragg and Scalar ship subimage vs. HH, 6th Iteration

## 4.2 TD-GLRT detection

To realize the TD-GLRT detection, ENL of quad polarization RADARSAT-2 SLC data will be used to perform a quick method for background and foreground parameter estimation. One sub-image with ship targets is shown in Figure 4.1 to 4.2, with the pixel location from (512, 1024) to (1535, 2047), acquired on February 28th, 2011, over the coastal area of Ijmuiden port, Holland. Compared with Bragg co-pols, either Scalar co-pol and cross-pol from both Bragg and Scalar shows a much more lower background, rising the ratio of target to clutter (T/C). Here the background indicates the reflection from water. The histograms denotes a lower variation of scalar component compare with those of Bragg and the total data (HH).

### 4.2.1 ENL estimator

Conventional ENL has been defined for the case of single polarization SAR. Manually select a homogeneous image region, assuming the speckle has been fully developed and without texture, the scattering coefficient is circular complex Gaussian. For PolSAR data, the ENL has traditionally been estimated separately for each polarimetric channel and then averaged [152]. Continued with the previous work on statistical analysis in Chapter 3, we apply an ENL threshold to estimate the parameter vector  $\Theta = [E(\sigma), \text{VAR}(\sigma)]$  for both the target and

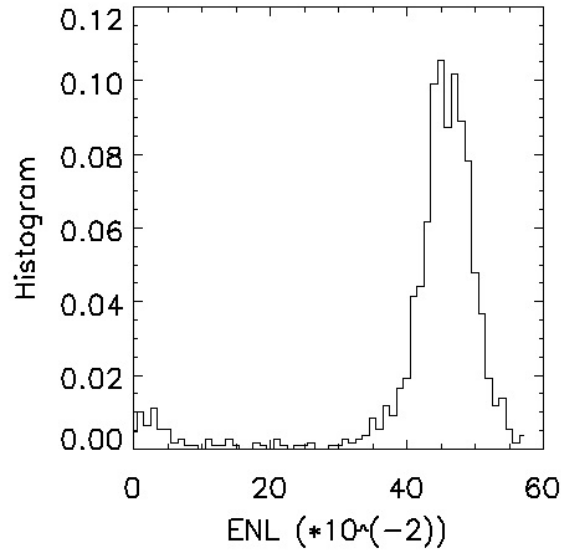


**Figure 4.3** — ENL histogram with two definitive peaks indicating a good candidate for thresholding

the background represented by the Scalar contribution,

$$\text{ENL} \begin{cases} \leq & \text{heterogeneous} \\ \equiv & \text{threshold} \\ \geq & \text{homogeneous} \end{cases} \quad (4.15)$$

The principle of this method is based on the common sense that the presence of texture will increase the locale variance and therefore leads to an underestimation of ENL, according to the traditional definition as the coefficient of variation in Equation 3.25, and on the other hand, will increase the scatters in the single resolution cell hence increase the backscattered intensity of the incident microwave, corresponding to the brighter pixels on the SAR image. As the expression in Equation 4.13,  $X_{sc}$  is a two dimension vector, and the same degradation for ENL, the polarimetric definition of which as

$$\text{ENL} = \frac{\text{Tr}(\Sigma)^2}{\langle \text{Tr}((X_{sc}^{T*} X_{sc})^2) \rangle - \text{Tr}(\Sigma \Sigma)} \quad (4.16)$$

where  $\Sigma = E(X_{sc}^{T*} X_{sc})$  is the covariance matrix of  $X_{sc}$ . This polarimetric ENL expression is an extension of the one derived in [152], and  $\langle \cdot \rangle$  stands for the average within the moving window. The homogeneity was then analyzed by computing the ENL using a moving window of 30 by 30 pixels from which the mean covariance matrix  $\Sigma$  was estimated as well as the mean of the trace of the product of the covariance matrix. Because the swath of the satellite image for quad polarization data is only half of that of the SCW products, a window of 30 by 30 pixels contains less scatters for SLC than that of the SCW data. Different sizes of window have been chosen in order to keep enough samples of the correlated scatterers and incoherent ones. A landmask from NOAA of 1km resolution was used to calculate the mean value for

the ocean image as well as the ENL distribution. The histogram shows very good threshold property, as in Figure 4.3, with the two peaks located to the opposite ends on range of the ENL. The threshold for ENL could be find easily from the histogram as 0.1. Figure 4.4 shows the homogeneity estimation by ENL estimator.

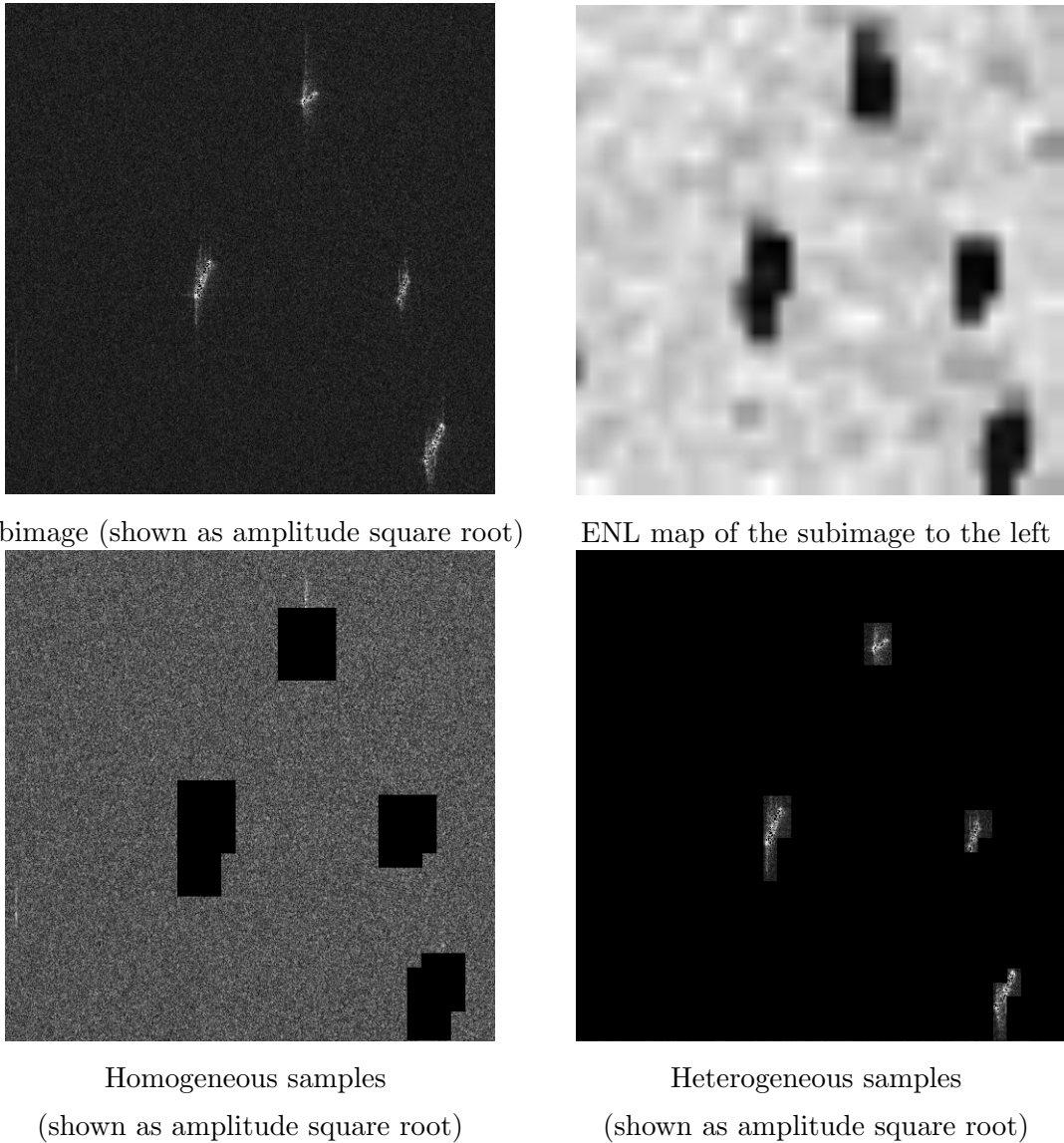


*Figure 4.4* — Homogeneity shown on the ENL map of the subimage

#### 4.2.2 TD-GLRT test

The parameter vector  $\Theta = [E(\sigma), \text{VAR}(\sigma)]$  for both the target and the background represented by the Scalar contribution could be estimated from the heterogeneity and homogeneous ROI in Figure 4.4, and could also be represented using the histograms shown in Figure 4.5.

The long 'tail' represented by the polarimetric measurements as well as the Bragg con-

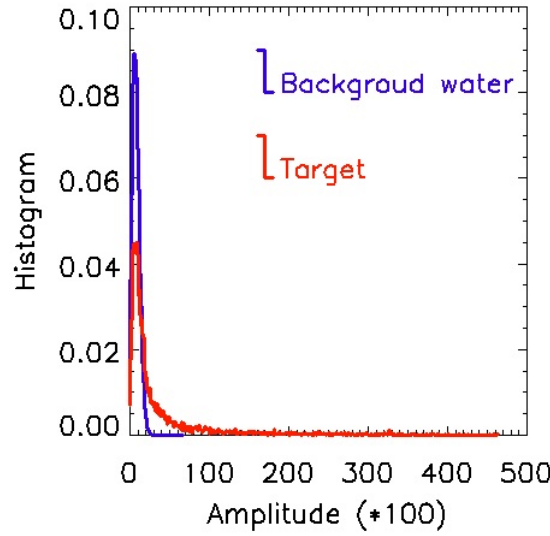


Figure 4.5 — PDF for target ( $H_1$ ) and water ( $H_0$ )

tributions could also be found in the histogram of the Scalar contribution at the present of man-made targets, and the 'tail' will be longer, e.g. may as twice longer, than that represented on the Bragg contribution without the present of man-made targets (comparison may be find from Figure 3.9 and 4.5). This could as well support the principle of using Scalar contribution to build TD-GLRT detection, since both Bragg and the total polarimetric measurements always denote a long 'tail' characteristic by the histogram while the Scalar contribution has that characteristic only when there are strong polarized scatterers, i.e. those come from man-made targets, appear in the resolution area. To our interest, the 'tail' effect on Scalar is different from the spiky effect introduced by the 'tail' of Bragg or the direct radar measurements. It is from the real generic target.

Figure 4.6 shows the statistical model will be used in the decision Inequality 4.14, which is changed as

$$\Lambda(X_{sc}) = \frac{p_{X_{sc}/\Theta_1}(X_{sc}/\Theta_1)}{p_{X_{sc}/\Theta_0}(X_{sc}/\Theta_0)} = \frac{\frac{b_1/A}{\Gamma(M_1)} \left(\frac{b_1 A}{2}\right)^{M_1} K_{(M_1-1)}(b_1 A)}{\frac{b_0/A}{\Gamma(M_0)} \left(\frac{b_0 A}{2}\right)^{M_0} K_{(M_0-1)}(b_0 A)} \underset{H_0}{\underset{H_1}{\geq}} \eta, \quad (4.17)$$

by replacing the possibility density function  $p_{X_{sc}/E(\sigma_T), \text{VAR}(\sigma_T)}(X_{sc}/E(\sigma_T), \text{VAR}(\sigma_T))$  and  $p_{X_{sc}/H_0}(X_{sc}/H_0)$  with K-distribution given in Equation 3.21 and its expression for amplitude  $A = \sqrt{\sigma}$ ,

$$P_N(A; r) = \frac{b/A}{\Gamma(M)} \left(\frac{bA}{2}\right)^M K_{(M-1)}(bA), \quad (4.18)$$

where the slope parameter  $\frac{2*\sqrt{M}}{b} = E(A)$  and the shape parameter  $M = N(\nu + 1)$ , with  $N$

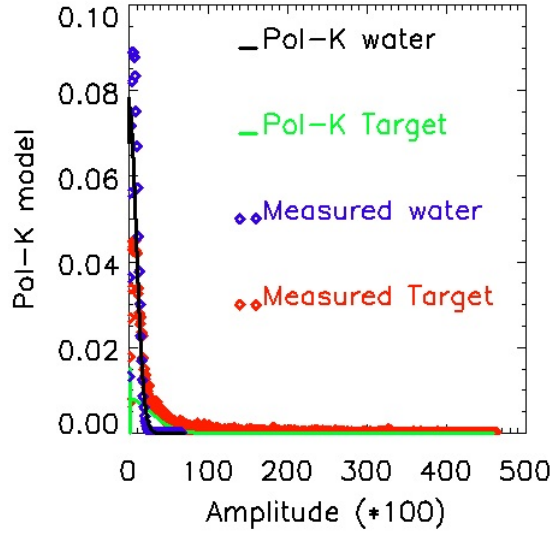


Figure 4.6 — Pol-K-modelled target ( $H_1$ ) and water ( $H_0$ )

the total scatterer number and  $\nu$  is a real number larger than  $-1$  which relates to the order of freedom of radar reflectivity's  $\chi^2$  distribution.

Above mentioned methods were implemented on Radarsat-2 (R2) C-band data with preliminary results leading to improvements in this chapter. The data set consists of 20 scenes of full polarization and 4 scenes of dual polarization wide swath (2 with ScanSAR beam and 2 with Single Beam), shown in Table 4.2.2. The first two scenes which are acquired in the ScanSAR Wide beam have their ground range product type, i.e., SGF, for which the pixel spacing does not meet the Nyquist criterion in all areas of these two scenes [99], meaning that this type of product are appropriate for applications where the full precision is not needed, e.g., oil pollution detection, illegal ship monitoring. The rest scenes in the data set are all belonging to slant range product with a complex data type, i.e., SLC, for which the pixel spacing is determined by the radar range sampling rate and pulse repetition frequency (PRF), and the single look processing made use of full available signal bandwidth, reaching at a fine spatial resolution.

Simply setting  $\eta$  in Inequality 4.17 to be 1, the decision criterion 4.17 says  $H_1$  to be true when the amplitude  $A > 1722$ . The result shown in Figure 4.8.

### 4.3 Discussion and conclusion

The accuracy of target classification depends on the uniqueness of the solution to an invert scattering model. The main idea behind TD theorems is to express the average scattering

*Table 4.1* — Radarsat 2 C-band data set

satellite acquisition / orbit pass	beam mode	operational mode	nominal resolution (range,azimuth) (m)	product type
20090818/ a	ScanSAR	ScanSAR Wide, HH+HV	50,50	SGF
20090903/ d	ScanSAR	ScanSAR Wide	50,50	SGF
20090831/ d	Single Beam	Wide	11.83,4.97	SLC
20090903/ d	Single Beam	Wide	11.83,4.97	SLC
20101017/ d	Single Beam	Fine Quad Polarization	4.73,5.12	SLC
20110228/ a	Single Beam	Fine Quad Polarization	4.73,4.76	SLC
20110809/ d	Single Beam	Fine Quad Polarization	4.73,4.86	SLC
20110810/ d	Single Beam	Fine Quad Polarization	4.73,4.86	SLC
20111203/ a	Single Beam	Fine Quad Polarization	4.73,5.11	SLC
20111205/ d	Single Beam	Fine Quad Polarization	4.73,5.11	SLC
20110819/ d	Single Beam	Fine Quad Polarization	4.73,5.13	SLC
20110803/ d	Single Beam	Fine Quad Polarization	4.73,5.12	SLC
20110812/ d	Single Beam	Fine Quad Polarization	4.73,5.15	SLC
20110820/ d	Single Beam	Fine Quad Polarization	4.73,5.15	SLC
20120416/ a	Single Beam	Fine Quad Polarization	4.73,4.96	SLC
20120406/ d	Single Beam	Fine Quad Polarization	4.73,4.72	SLC
20120409/ d	Single Beam	Fine Quad Polarization	4.73,5.60	SLC
20120329/ a	Single Beam	Fine Quad Polarization	4.73,5.19	SLC
20120408/ a	Single Beam	Fine Quad Polarization	4.73,4.83	SLC
20120423/ d	Single Beam	Fine Quad Polarization	4.73,4.78	SLC
20120405/ a	Single Beam	Fine Quad Polarization	4.73,4.75	SLC
20120509/ a	Single Beam	Fine Quad Polarization	4.73,4.97	SLC
20110904/ a	Single Beam	Standard Quad Polarization	7.99,4.83	SLC
20110907/ d	Single Beam	Standard Quad Polarization	7.99,4.83	SLC

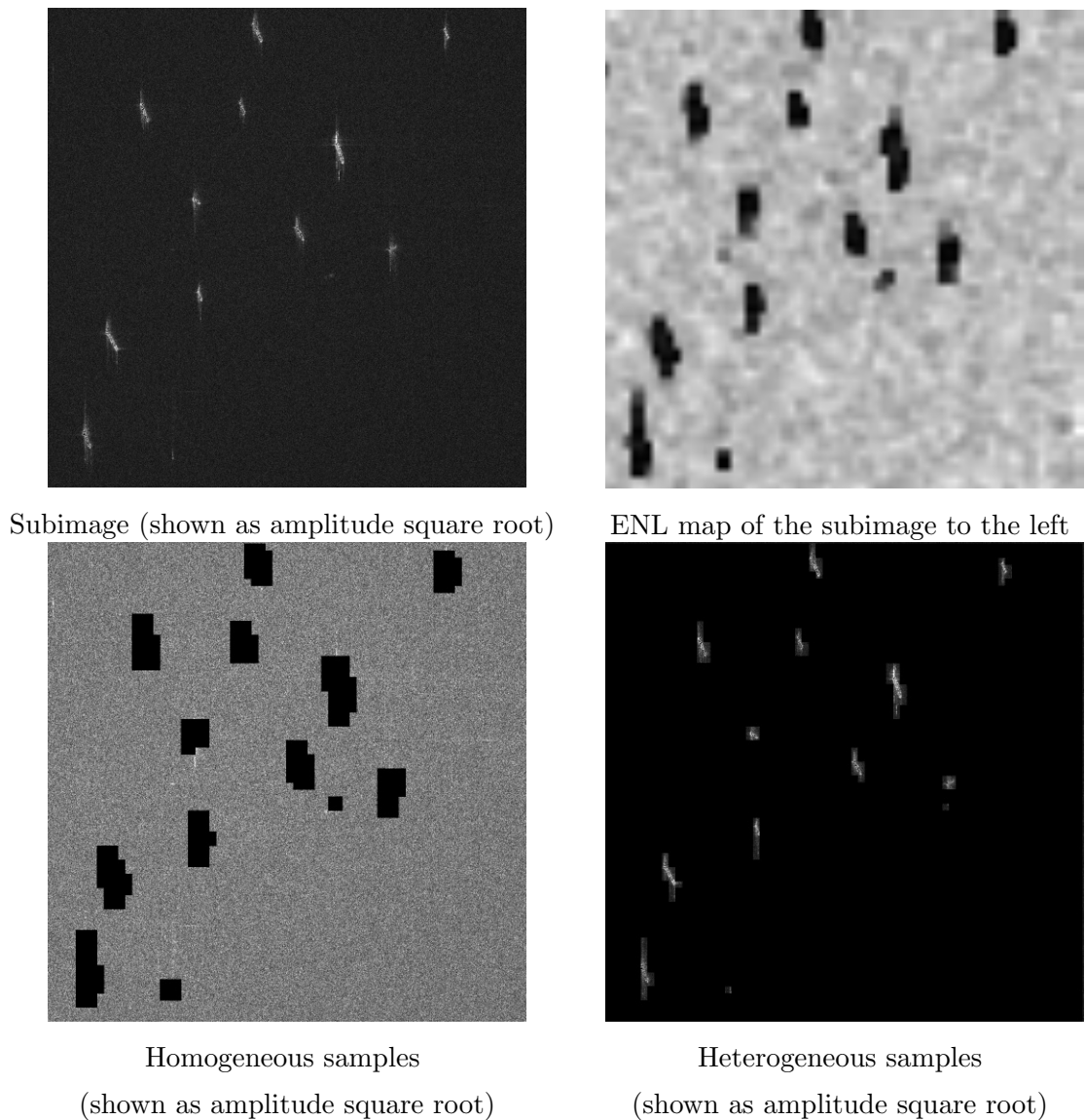
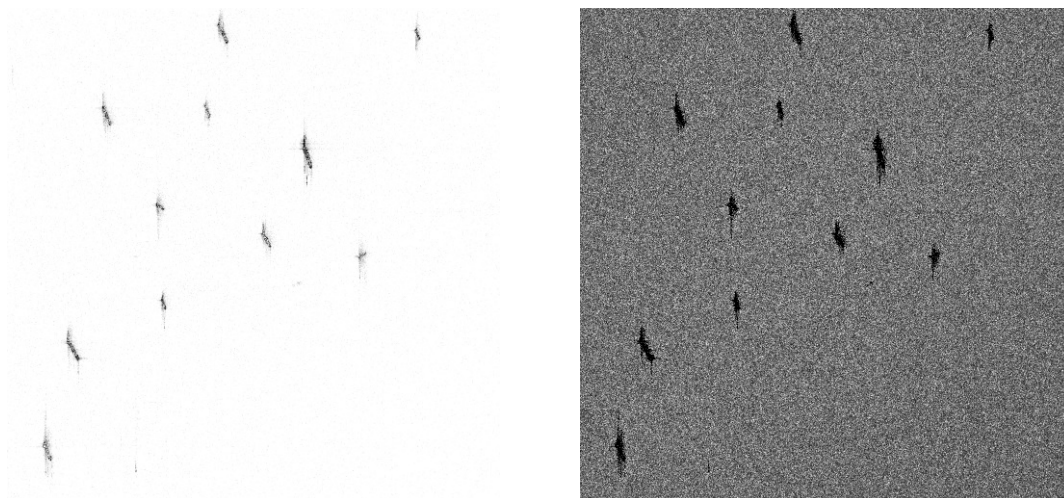


*Figure 4.7* — Homogeneity detection by ENL

matrix for a random media problem as a sum of independent elements and to associate a physical mechanism with each component. We tried for the first time the TD technique to model the sea surface into two separate part according to their scattering mechanisms. That's the main principle of our approach TD-GLRT.

The polarimetric ENL estimate is the second benefits from polarimetry for TD-GLRT. Histograms provide a means of determining whether or not an image is a good candidate for thresholding. With polarimetric ENL histogram, it is possible to estimate the parameter vectors for both the foreground pixels from background pixels.

Comparing with the conventional CFAR detection algorithms, the polarimetric method has the merit in that once a threshold has been selected to determine the polarimetric prop-



(a) TD-GLRT detection when  $H_1$  is true (shown as intensity)      (b) TD-GLRT detection when  $H_0$  is true (shown as amplitude)

*Figure 4.8* — TD-GLRT detection

erties of each pixel, there are no other user inputs required, while on the other hand, CFAR algorithms require a probability of false alarm so as to be able to generate a threshold. The polarimetric method does not link the threshold to a false alarm rate so there is no trade-off between false alarm rate and detection probability [60].

---

# Conclusion and Perspectives

For the first time, we applied target decomposition theory on the polarimetric SAR data over sea surface, which is a surface in motion everywhere at any time, making the problem more complicate than the other conditions. This study is a trial for extracting details of a fine resolution, i.e., within single pixel scale, taking the speckle as a represent of physical structure instead of noise to be smoothed out. Characteristics retrieval and target classification has been established, using polarimetry and Bayesian detection theories, both at pixel scale and imagery scale.

## 1. Decomposition

A decomposition of different scattering mechanisms have been performed for ocean satellite SAR imagery to better understand the non-polarized (Scalar) contribution to the total radar cross section (RCS) and Doppler measurements.

There are generally three types of surface scattering mechanisms occurring when the sea surface is probed by microwave radar, i.e., Bragg, specular, and Rayleigh, which correspond respectively to sea surface capillary wave, the crest of the longer wave before it breaks, and the bubbles and foams formed by wave breaking. Different scattering mechanisms induce different polarimetric scattering coefficients and Doppler spectrum. It had been impossible to split those scattering mechanisms with single polarization radar imageries. At pixel scale, we split radar scattering matrices into Bragg and Scalar

contributions. The splitting is an iteration initiated with the radar incidence angle and then controlled by a local incidence angle which is function of co-polarization and cross-polarization.

Based on these developments and testing, a strategy has been refined to analyze the signature of different features, to retrieve wind seas and sea swell parameters, as well as slick areas, ships, oil rigs, such non-polarized targets that may be buried in the Scalar contributions.

## 2. Statistical model

With polarimetric scattering coefficients estimated both for Bragg and Scalar contributions, a sea clutter model describing almost the real sea surface has been improved, for the first time, according to scattering contributions statistically.

This model is a generalization of K distribution to multivariate, i.e., multi-polarization, representations, hence we named it as *Pol – K* distribution. Not to estimate the average, trials focus on the weighting of Bragg or Scalar contributions within single pixel, by the prior knowledge regards the sea surface as a superposition of waves of various wavelength as well as the common Rayleigh scatterers due to wave breaking.

## 3. Detection

Motivated by the improved statistical model, which could be combined with Bayesian detectors, man-made metallic targets, such as ships, oil rigs, etc., which had been buried in the Scalar contribution could be detected and classified. The Bayesian detector TD-GLRT has been proposed following the target decomposition process. The ML estimation of the parameter vectors, utilizing the polarimetric ENL estimator, have been designed nested in the TD-GLRT detection algorithm. Weighting for each single pixel helps the target detection, need not a region of interest (ROI) to be select by human intelligence priorly.

The principle of TD-GLRT detection lies in the decomposition of scattering mechanism into Scalar and Bragg. Being different from Bragg or direct polarimetric measurements which always denote a long 'tail' characteristic, the Scalar contribution has this characteristic only when there are strong non-polarized scatterers, i.e. those come from man-made targets, appear in the resolution area. Because the Scalar contribution on normal sea surface comes from specular and Rayleigh scatterers happening at the wave crest

before it breaks and the foams occurring by the wave breaking, and the backscattered energy from these scatterers are relatively smaller than those from Bragg resonant. To our interest, the 'tail' effect on Scalar is not spiky, but by the real generic target.



# A

---

## Analytical solution of the radar equation

A radar system has a transmitter that emits in a predetermined direction the e.m. wave, called radar signals. When these come into contact with an object, they intrigue a current distribution inside of the object which generate the reflected and/or scattered fields. Thus the radar signals are reflected especially well by materials of considerable electrical conductivity, i.e. metals, seawater, and wet land. Among those radar signals reflected and/or scattered in directions, the one direction which towards the transmitter make the radar work.

### A.1 Definitions

#### A.1.1 Target Characteristics

The concepts of the idea of target determines the way in which they will be characterized [?].

#### **Radar cross section**

Given a radar configuration in which the target of interest is smaller than the footprint of the radar system, the target is considered as an isolated scatterer. From the point of view of power exchange, this target is characterized by the radar cross section.

The scattering cross-section is the effective area scattering in a given direction:

$$\sigma_{is}(\hat{n}_i, \hat{n}_s; Q) = \frac{4\pi R^2 |E_s|^2}{|E_i|^2} \quad (\text{A.1})$$

The variables in A.1 are the sphere radius  $R$  of the target surface and the receiving antenna,  $E_i$  and  $E_s$  is the incident electromagnetic wave and the scattered wave. RCS of a target is a function of a large number of parameters which are difficult to consider individually. The first set of these parameters are conneted with the imaging system:

- wave frequency.
- wave polarization.
- imaging configuration, i.e., incident and scattering directions .

The second set of parameters are related with the target itself:

- object geometrical structure
- object dielectric properties

### Scattering coefficient

Given the situation in which the target of interest is significantly larger than the footprint of the radar system, the target is more convenient to be characterized independently of its extent, hence to be described by scattering coefficient. In order to describe the behavior of a larger surface, we just sum the power incoherently from a collection of sub-surfaces of a size similar to  $A$ . The scattering crossection coefficient is defined by:

$$\sigma_{is}^0(\hat{n}_i, \hat{n}_s; Q) = \frac{4\pi R^2 \langle |E_s|^2 \rangle}{A |E_i|^2} \quad (\text{A.2})$$

Sigma-naught represents the ratio of the statistically averaged scattered power density to the average incident power density over the surface of the sphere of radius  $R$ . According to conservation of energy,  $\sigma^0$  should equal to one for isotropic re-radiation with no losses, but can be much grater than one for the directional re-radiation.

#### A.1.2 Radar equation

With the definition above, the radar equation for the bistatic case can be present as

$$P_r(\theta_s, \phi_s) = \frac{\lambda^2}{(4\pi)^3} \frac{P_t(\theta, \phi) G_t G_r}{R_1^2 R_2^2} \sigma_{rt}(\theta_s, \phi_s; \theta, \phi) \quad (\text{A.3})$$

for the 'smaller' target and

$$P_r(\theta_s, \phi_s) = \frac{\lambda^2}{(4\pi)^3} \int \frac{P_t(\theta, \phi) G_t G_r}{R_1^2 R_2^2} \sigma_{rt}^0(\theta_s, \phi_s; \theta, \phi) dA \quad (\text{A.4})$$

for the 'extent' target, where  $(\theta, \phi)$  defines the incident direction of the transmitted power  $P_t(\theta, \phi)$  at polarization  $t$  and  $(\theta_s, \phi_s)$  defines the scattered direction of the received power  $P_s(\theta_s, \phi_s)$  at polarization  $r$ .

## A.2 Stratton-Chu integral formulation

Solving Maxwell's equations for an e.m. wave striking a boundary allows the derivation of the Fresnel equations, which can be used to predict how much of the wave is reflected, and how much is refracted in a given situation. That's the case of specular reflection. For modelling oblique backscatter from rough surfaces, Stratton-Chu formulation is used to derive the Bragg scattering model. Providing that a volume does not contain any sources, then based on the physical-mathematical principle that fields at a point within a volume can be described in terms of the field distributions on the surface of the volume, Stratton-Chu integral approach can be used. Plant (1990) explains how this can be applied to specify the far-field radiated by an antenna and then to model the pattern of illumination by that antenna at the air-water interface, as long as the surface perturbations are of small amplitude.[?]

Stratton-Chu integral formular is as

$$\vec{B}(\vec{x}) = \vec{B}_i(\vec{x}) + \oint_S [ik(\vec{n}' \times \vec{E})G - (\vec{n}' \times \vec{B}) \times \nabla' G - (\vec{n}' \cdot \vec{B})\nabla' G] da' \quad (\text{A.5})$$

$$\vec{E}(\vec{x}) = \vec{E}_i(\vec{x}) - \oint_S [ik(\vec{n}' \times \vec{B})G + (\vec{n}' \times \vec{E}) \times \nabla' G + (\vec{n}' \cdot \vec{E})\nabla' G] da' \quad (\text{A.6})$$

Under the perfect conductivity assumption, it becomes

$$\vec{B}(\vec{x}) = \vec{B}_i(\vec{x}) + \oint_S (\vec{n}' \times \vec{B}) \times \nabla' G da' \quad (\text{A.7})$$

and more succinctly, as

$$\vec{B}(\vec{x}) = \vec{B}_i(\vec{x}) + \oint_S \vec{J}' \times \nabla' G da' \quad (\text{A.8})$$

where  $G = \exp(ikR)/4\pi R$  is the retarded Green function,  $\vec{B}(\vec{x})$  is the induced currents and  $\vec{B}_i(\vec{x})$  is the incident field at the point  $\vec{x}$ , and in the radiation gauge, when the vector potential due to a sinusoidal current, the current density which was excited by the incident wave on the surface,  $\vec{J}(\vec{x}, t) = \vec{J}(\vec{x})e^{i\omega t}$ , is given by

$$\vec{A}(\vec{x}) = \frac{1}{c} \int_S \vec{J}(\vec{x}') G da' \quad (\text{A.9})$$



---

# B

## Scatterometer operation

Oblique-viewing radars measuring the average backscatter from a wide field of view (FOV) are called scatterometers, and are used primarily to measure the wind which creates the surface roughness elements. Scatterometers illuminate the same portion of the ocean from different directions to make use of this dependence to extract wind speed and direction. When the data came back to the ground, the entire returned power will be initially used to generate one cross section measurement, which will then go into wind retrieval.

The magnitude and polarisation of the returned pulse is primarily a measure of the surface roughness, which depends on the microwave reflecting properties of the sea surface, also depends on the incidence angle [46]. Although theoretical models exist to relate backscattered power to wind (as we have seen, Bragg scattering is the main contributing mechanism in backscattering), the dispersions of these models (a few dB) fail to match the accuracy of modern instruments (ERS has 0.2 dB). Hence, empirical models are used.

### B.1 Wind definition

It is important to realize that the radar backscatter measurement  $\sigma_0$  is related to the wind at 10 meters height above the ocean surface, simply because such measurements are widely available for validation. This means that any effect that relates to the mean wind vector at 10 meters height is incorporated in the backscatter-to-wind relationship, by a geophysical

model function (GMF). GMF function enables the calculation of equivalent neutral winds, which is defined as the wind in case of a fully stratified (or stable) atmosphere.

## B.2 ASCAT

ASCAT is a real aperture radar using vertically polarised antennas. Two sets of three antenna are used to generate radar beams looking 45 degrees forward, sideways and 45 degrees backwards with respect to the satellite's flight direction, on both sides of the satellite ground track. As the backscatter depends on the sea surface roughness as a function of the wind speed and direction at the ocean surface, it is possible to calculate the surface wind speed and direction by using these 'triplets' within a mathematical model [172].

## B.3 CMOD2

CMOD2 has the form

$$\sigma^0 = B_0[1 + B_1 \cos(\phi) + B_2 \cos(2\phi)]$$

$B_0 = 10^\alpha V^\gamma$ ,  $B_1$  and  $B_2$  are parabolic functions of the incidence angle  $\theta$  and linear functions of wind speed  $V$ .  $B_1$  term represents the smaller difference between backscatters of a wind blowing up versus one blowing down the beam, and  $B_2$  term represents the large difference between that of a wind blowing up or down compared to one blowing across the beam. Wind direction  $\phi$  is measured relative to the pointing direction of a beam (projected onto the horizontal plane), with  $\phi = 0$  corresponding to a wind blowing directly towards the beam. Wind direction can also be defined with respect to the subsatellite track. To distinguish which frame is being used,  $\varphi$  is used to indicate directions measured relative to the satellite pointing direction and  $\phi$  for directions relative to a beam.

For ERS SCAT, the fore, mid and aft beams has the relationship between of

$$\varphi = 45 + \phi$$

$$\varphi = 90 + \phi$$

$$\varphi = 135 + \phi$$

So a  $\sigma^0$  triplet  $(\sigma_1^0, \sigma_2^0, \sigma_3^0)$  can be written as

$$\sigma_1^0 = B_0[1 + B_1(\sin\varphi + \cos\varphi)/\sqrt{2} + B_2 \sin\varphi]$$

$$\sigma_2^0 = B_0^*[1 + B_1^* \sin\varphi - B_2^* \cos 2\varphi]$$

$$\sigma_3^0 = B_0[1 + B_1(\sin\varphi - \cos\varphi)/\sqrt{2} - B_2 \sin\varphi]$$

From the experimental assumption that  $B_1$  is small relative to  $B_2$ , to neglect  $B_1$  and  $B_1^*$  when

$$\sigma_1^0 + \sigma_3^0 \approx 2B_0 = 2 \times 10^\alpha V^\gamma$$

showing that a cross section where  $\sigma_1^0 + \sigma_3^0 = \text{constant} = 2\sigma_{ref}^0$  corresponds to a section of constant speed  $V$ . Also achieve an upwind circle for  $\phi \in (0, \pi)$  and downwind circle for  $\phi \in (\pi, 2\pi)$  as

$$\left(\frac{\sigma_3^0 - \sigma_1^0}{2B_0B_2}\right)^2 + \left(\frac{\sigma_2^0 - B_0^*}{B_0^*B_2^*}\right)^2 = \cos^2 2\phi + \sin^2 2\phi = 1$$



# C Glossary

---

## C.1 Abbreviation

ACF	Auto Covariance Function p.43	NB	Negative Binomial p.67
ATR	Automatic Target Recognition p.78	NRCS	Normalized Radar Cross Section p.9,28
BSA	Backward Scattering Alignment p.6	OPD	Optimal Polarimetric Detector p.79
CFAR	Constant False Alarm Rate p.78	OSMC	Observing System Monitoring Center p.33
CTD	Coherent Target Decomposition p.20	PDF	Probability Density Function p.87
CV	Coefficient of Variation p.60	PGLRT	Polarimetric GLRT p.78
EGR	Elementary Geometric Reflector p.19	POA	Polarization Orientation Angle p.14
EM	Electromagnetic p.1,2	PR	Polarization Ratio p.9,28
ENL	Equivalent Number of Look p.14,60	PR	Power Ratio p.78
FFT	Fast Fourier Transform p.45	PRF	Pulse Repetition Frequency p.33,69,90
FSA	Forward Scattering Alignment p.6	PRI	Pulse Repetition Interval p.21
GLRT	Generalized Likelihood Ratio Test p.79	PSD	Power Spectrum Density p.41
ICTD	Incoherent Target Decomposition p.21	PWF	Polarization Whitening Filter p.79
IRF	Impulse Response Function p.69	RAR	Real Aperture Radar p.23
GK	Generalized K p.58	RCA	Resonant Curvature Approximation p.9
KA	Kirchhoff Approximation p.9	RCS	Radar Cross Section p.iii
LCA	Local Curvature Approximation p.9	ROI	Region of Interests p.65,87
LOS	Line of Sight p.18,27	R/V	Range-to-Velocity ratio p.26
LRT	Likelihood Ratio Test p.78	SAR	Synthetic Aperture Radar p.iii
LUT	Look-Up Table p.59	SCW	ScanSAR Wide p.59
MTF	Modulation Transfer Function p.25		

SGF	SAR Georeferenced Fine p.41	TD	Target Detection p.27,78
SLC	Single Look Complex p.8	TSM	Two Scale Model p.9
SSA	Small Slope Approximation p.9	UCA	Upwind-Crosswind Anisotropy p.9
SSA	Sea Surface Approximation p.9	UDA	Upwind-Downwind Asymmetry p.9
SPM	Small Perturbation Model p.9,27	WAM	WAVE prediction Model p.25
T/C	Target-to-Clutter ratio p.79		

## C.2 Notation

$\alpha$	polarization transformation ratio angle p.3
$\alpha$	one of the polarimetric parameters in H/A/ $\bar{\alpha}$ decomposition p.27
$\alpha$	Ratio of tilt Bragg scattering by VV polarization over HH polarization P.29
$\beta$	one of the polarimetric parameters in H/A/ $\bar{\alpha}$ decomposition p.27
$\beta$	Ratio of Bragg scattering by SPM p.30
$\epsilon$	electric field scattered by irregular surface p.12
$\eta_{HV}$	phase difference between the orthogonal components of an electric field p.3
$\theta$	radar incidence angle P.10
$\lambda$	eigenvalue of coherency $T$ matrix p.27
$\rho$	complex polarization transformation ratio p.3
$\tau$	polarization elliptical angle P.5
$\phi$	polarization orientation angle P.5
$\varphi_i$	a phase factor from the $i$ th scatterer p.12
$\varphi$	Phase p.51
$a_i$	a real form factor from the $i$ th scatterer p.12
$\vec{E}$	electric field of electromagnetic wave p.3
$h$	antenna effective length p.6
$\hat{h}$	unit vector of the orthogonal basis p.3
$S$	Sinclair scattering matrix p.6

## C.3 Terminology

### C.3.1 Oceanography

#### capillary wave

A ripple along the interface of two fluids is called capillary wave. A capillary wave is a surface-tension wave travelling along the phase boundary of a fluid, whose dynamics are dominated by the effects of surface tension. The wavelength of capillary waves in water is typically less

than a few centimeters (2.5cm). In [28], the term capillary wave was used for convenience to describe both the short gravity waves and the surface-tension waves, which are the two resonant components of the ocean surface to the radar wavelength.

### **gravity wave**

Gravity wave is a wave whose dynamics are dominated by the effects of gravity. The wavelength of gravity waves is typically greater than 5 centimetres.

### **swell**

A swell is a series surface gravity wave that is not generated by the local wind. The wavelength of swell is usually long but varies with the size of the water body and also from event to event, e.g. rarely more than 150m in the Mediterranean and may longer than 700m away from the most severe storms.

### **wind wave**

Wind wave occurs on the free surface of ocean is called ocean surface waves. Wind waves range in size from small ripples to huge waves over 30 meters high. When directly being generated and affected by the local winds, a wind wave system is called a wind sea. After the wind ceases to blow, wind waves are called swell.

### **fetch**

The fetch describes how far the wave has travelled, i.e., the distance for which the wind blows over the surface of the water. M. I. Skolnik defined in "*Radar Handbook*" as the area of the sea surface over which the wind seas are generated by a wind having a constant direction and speed, or the length of the fetch area measured in the direction of the wind in which the wind seas are generated. Fetch length along with the wind speed determines the size of wave produced. The longer the fetch length and the faster the wind speed, the larger and stronger the wave will be. Fetch length determines the power and energy of the wave. If the winds are blowing in the same direction during the wave's lifetime, the wave will in turn be stronger. The longer the wind drags along the sea the more energy the wave will have which will make the wave a destructive wave.

**friction velocity**

The growth of waves under the influence of the wind has an equilibrium range, for that the wave interactions are usually incapable of transferring energy from a given wave-number band as rapidly as it is supplied by the wind. As a result the size of waves must be limited by the requirement of the water surface stability. If the surface becomes locally unstable, the wave breaks and energy lost from the wave motion, leaving a restored stability. The probability of breaking at a given point is some function of the local fluid acceleration at the surface as a fraction of the gravitational acceleration  $g$  [173].

**destructive wave**

Destructive wave is created in storm conditions. It has a short wave length but high frequency, and is high and steep. It has a stronger backwash than swash and erode the coast, hitting the shore 10-15 times a minute.

**constructive wave**

Constructive wave is created in calm weather. It has a long wave length but low height and low frequency, hitting the shore 6-9 times a minute. It has a stronger swash than the backwash and it breaks on the shore and deposit material, building up the beach.

**fully developed sea**

The maximum height to which ocean waves can be generated by a given wind force blowing over sufficient fetch, regardless of duration, as a result of all possible wave components in the spectrum being present with their maximum amount of spectral energy.

**sea state**

The numerical or written description of ocean-surface roughness. Ocean sea state may be defined more precisely as the average height of the highest one-third of the waves (the significant wave height) observed in a wave train.

**wind streak**

It is usually assumed that the wind direction aligns with boundary layer atmospheric roll vortices, which often appear as streaks at kilometre-scales in SAR images of the ocean. The orientation of wind streaks is assumed to lie essentially parallel to ocean surface wind direction [174].

**significant wave height**

Significant wave height (SWH), is defined as the average of the heights of the one-third highest waves in a wave train observed at a point. It is approximately equal to four times the standard deviation of the wave train.

**Rayleigh scattering**

When waves break, water droplets of varying size are thrown into the air, and air is trapped creating bubbles within the water body. The bubble sphere has a dielectric constant much more different from the surrounding medium, and the microwave energy scattered from these Rayleigh scatterers is stronger. Rayleigh scattering is significant for  $(d/\lambda_0) \lesssim 0.01$  where  $d$  is the diameter of the sphere and  $\lambda_0$  is the radar wavelength. Rayleigh scatters are isotropic particles.

**C.3.2 RADAR****looks**

Individual looks are groups of single samples in a SAR processor that split the full synthetic aperture into several sub-apertures, each representing an independent look of the identical scene. In signal processing, the location of signal energy in the azimuth frequency domain depends on the antenna pointing angle, and looks are different azimuth spectral bands. Since the Doppler frequency varies with azimuth time, the azimuth frequency is often referred to as Doppler frequency.

**number of range looks**

The number of distinct or overlapping coherently processed looks extracted from the pulse bandwidth which are combined after detection to form the image.

**number of azimuth looks**

The number of distinct or overlapping coherently processed looks extracted from the Doppler spectrum which are combined after detection to form the image.

**azimuth look bandwidth**

The processed Doppler bandwidth for each individual azimuth look. In Spotlight mode, it is taken to mean the Doppler bandwidth of each target in the scene.

**ScanSAR azimuth look bandwidth**

The Doppler bandwidth of the signal from any given target within the set of samples used for each ScanSAR look. For any ScanSAR mode, this bandwidth varies from beam to beam, and decreases from near edge to far edge within any one beam.

**range-azimuth coordinate**

The azimuth direction on the imaged surface is taken to be parallel to the motion of the radar, and the range direction is perpendicular to azimuth direction clockwise.

**distributed target**

There is a fact that not all radar targets are stationary or fixed, but instead change with time. Aside from the natural movements of the target, the radar itself may be airborne or spaceborn, moving with respect to the target and illuminating in time the different parts of an extended volume or surface. In these cases, the radar will receive time-averaged samples of scattering from a set of different single targets. The set of single targets from which samples are obtained is called a distributed radar target.

**SAR velocity bunching relationships**

The azimuthal resolution of a side-looking SAR relies on the phase history of the returns from a scatterer,  $S$ , the position of the scatterer in the image plane can be related to the Doppler shift [175]. For stationary scatterer, it has a reduced Doppler frequency when it locates behind the satellite while an increased Doppler frequency when it locates ahead of the satellite.

**Doppler centroid frequency**

The Doppler centroid frequency of the SAR signal is location of the azimuth beam centre.

**aperture**

Consider an opaque screen in the  $x,y$  plane at  $z=0$ . The aperture,  $\Lambda$ , can be described as a closed set of points such that the screen at  $(x,y)$  is removed if  $(x,y) \in \Lambda$  [176]. EM wave passing through the aperture can be described as multiplying a two-dimensional signal by a two-dimensional function,

**co-polarisation nulls**

The antenna polarisation state for which zero backscattered power is received from a particular target. For co-polarisation, the transmit and receive antennas are the same. Co-polarisation nulls may not correspond to the maximum cross polarisation received power.

**cross polarisation maxima**

The antenna polarisation state for which maximum cross-polarised backscattered power is received from a particular target.

**cross polarisation nulls**

The antenna polarisation state for which zero cross-polarised backscattered power is received from a particular target. For co-polarisation, the transmit and receive antennas are the same. Note that for cross polarisation nulls the co-polarisation power is maximum.

**cross polarisation signature**

The received signature when the transmit and receive antennas have orthogonal polarisations.

**cross-polarised waves**

Or orthogonal waves. Each wave in a pair of cross-polarised waves are completely polarised. However, an antenna optimised to receive the co-polarisation maximum of one wave will receive no power from the other wave. Note that, in general, an arbitrary wave may be treated as the sum of two cross-polarised waves.

**VV**

Vertical transmit - vertical receive polarisation. A mode of radar polarisation where the microwave of the electric field are oriented in the vertical plane for both signal transmission and reception by means of a radar antenna. In this case, the plane of the electric field of the microwave energy is designated by the letter V for both transmit and receive event, i.e. VV; this transmit-receive polarity is also called like-polarised as opposed to cross-polarised. The amount of radar backscatter received at a particular linear polarisation state from a particular ground surface or object depends, in part, on the scattering mechanism and depolarisation effects involved. The transmit-receive acronym is often used in conjunction with the frequency band (wavelength) designation of a particular radar system.

### C.3.3 Statistics

#### central limit theorem

The central limit theorem (CLT) briefly states that the sum of a large number of i.i.d. (independently and identically distributed) random variables will be normally distributed, and the approximation steadily improves as the number of observations increases. This theorem is considered the heart of probability theory, although a better name would be normal convergence theorem.

#### Rayleigh distribution

For 2-D vectors, if the two orthogonal components are i.i.d. (independently and identically distributed) normally distributed, the module of vectors is Rayleigh distributed. One important related distribution is the exponential distribution. If the module is Rayleigh distributed then the power of vectors follows the exponential distribution.

#### modified Bessel functions

In the Bessel differential equation,

$$x^2 \frac{d^2 y}{dx^2} + x \frac{dy}{dx} + (x^2 - \alpha^2)y = 0$$

if the argument is complex and purely imaginary, the solutions of this Bessel equation is called the modified Bessel functions of the first ( $I_\alpha$ ) and second ( $K_\alpha$ ) kind,  $\alpha$  is the order of the Bessel functions and could be arbitrary real or complex number. ( $I_\alpha$ ) is exponentially growing and ( $K_\alpha$ ) is exponentially decaying function.

#### Nyquist criterium

As for all sampled band-limited signals, digital SAR raw data must be sampled at a rate greater than that dictated by the Nyquist criterion. For example, the ERS-1 raw SAR signal is sampled in complex form at 18.96 MHz, corresponding to a range sample spacing of 7.91 m. Since the ERS-1 chirp bandwidth is 15.55 MHz, this range signal is in principle oversampled by 22%. [177] According to the Nyquist criterion, it is the signal bandwidth which determines the minimum sampling rate. SAR image is the result of coherently processing returned echo signals, thus the pixel values are complex quantities.

**square-law detectors**

In radio frequency (RF) band detection, the electromagnetic field drives oscillatory motion of electrons in an antenna. In optical detection, the desired non-linearity is embedded in the photon absorption process itself. Conventional light detectors-so called "Square-law detectors"-respond to the photon energy to free bound electrons[178].

**arcsine law**

If the real part and the imaginary part of a complex digital signal are nearly Gaussian processes, the autocorrelation function can be calculated only by examining their signs. Arcsine law is fulfilled for SAR SLC signals.

**cross-spectral analysis**

The DFT of the cross-correlation may be called the cross-spectral density, or 'cross-power spectrum', or even simply 'cross-spectrum'.

**relative variance**

relative variance is the square of the coefficient of variation. In probability theory and statistics, the coefficient of variation (CV) is a normalized measure of dispersion of a probability distribution.



**Article de revue avec comité de lecture**

Wang B., Chapron B., Garello R., "Polarimetric sea surface scattering", IEEE Journal of Oceanic Engineering, in press.

**Communication dans une conférence à comité de lecture**

Wang B., Chapron B., Mouche A., Mercier G., Garello R., He M.X., "Interpreting C-band sea surface depolarization observations", IGARSS 2012, 22-27 July 2012, Munich, Germany

Wang B., Chapron B., Mercier G., Garello R., He M.X., "Sea surface radar backscatter simulation based on eigenvector decomposition", OCEANS 2012, 21-24 May 2012, Yeosu, Korea

Wang B., Chapron B., Mouche A., Mercier G., Garello R., He M.X., "De-polarization model - a polarimetry approach", CFOSAT 2011, 14-16 November 2011, Brest, France

Wang B., Chapron B., Mercier G., Garello R., He M.X., "Polarimetric characteristics of ships on RADARSAT-2 data", OCEANS 2011, 6-9 June 2011, Santander, Spain

Wang B., Chapron B., Mercier G., Garello R., "Microwave backscatter of ship signatures on SAR imagery", OCEANS 2010, 20-23 Sept. 2010, Seattle, USA

Wang B., Chapron B., Garello R., "SAR Speckle Characteristics Observed on RADARSAT-2 Dual Polarization Product", OCOSS2010, 21-23 June 2010, Brest, France



---

# Bibliography

- [1] Lee J. S. and E. Pottier. *Polarimetric radar imaging*. CRC Press, Taylor & Francis Group, 2009.
- [2] Stoffelen Ad. *Scatterometry - De scatterometer*. Thesis of doctor, University Utrecht, Netherland, 1998.
- [3] Chapron B. F. Collard and V. Kerbaol. Satellite synthetic aperture radar sea surface doppler measurements. *Proceedings of the Second Workshop on Coastal and Marine Applications of SAR*, ESA Publications Division SP-565, Spet. 2003.
- [4] Cloude S. R. *Polarization applications in remote sensing*. Oxford University Press, 2010.
- [5] Kennaugh E. M. *Polarization properties of radar reflections*. master thesis, The Ohio State University, 1952.
- [6] Raney R. K. Dual-polarized sar and stokes parameters. *IEEE Geoscience and Remote Sensing Letters*, Vol. 3, No.3, July 2006.
- [7] Boerner W. M. *Inverse scattering problems in optics*, chapter 7, Polarization utilization in electromagnetic inverse scattering. Springer-Verlag Berlin Heidelberg, 1980.
- [8] Boerner W. M. C. L. Liu and X. Zhang. Comparison of optimization procedures for 2x2 sinclair, 2x2 graves, 3x3 covariance and 4x4 mueller (symmetric) matrices in coherent radar polarimetry and its application to target versus background discrimination in microwave remote sensing and imaging. *International Journal of Advances in Remote Sensing (IJARS)*, Vol. 2, No.1-1(pp. 55-82), January 1993.
- [9] Mishchenko M. I. and L. D. Travis. *Lecture Notes in Physics*, chapter 9, Polarization and depolarization of light. Sringer-Verlag Berlin Heidelberg, 2000.
- [10] Cloude S. R. and E. Pottier. A review of target decomposition theorems in radar polarimetry. *IEEE Transacctions on Geoscience and Remote Sensing*, VOL.34, NO. 2, MARCH 1996.

- [11] Lee J.S. W.M.Boerner D.L.Schuler T.L.Ainsworth I.Hajnsek K.P.Papathanassiou and E.Luneburg. A review of polarimetric sar algorithms and their applications. *Journal of Photogrammetry and Remote Sensing*, Volume 9, No. 3(PP. 31-80), September 2004.
- [12] Mott H. *Remote Sensing with Polarimetric Radar*. John Wiley & Sons, Inc, 2007.
- [13] Huynen J.R. *Phenomenological theory of radar targets*. PhD thesis, ELEKTROTECHNISCH INGENIEUR, GEBOREN TE BATAVIA, 1970.
- [14] Cloude S. R. *Polarimetric principles and techniques*. Controller HMSO London, October 1983.
- [15] Valenzuela G. R. Theory for the interaction of electromagnetic waves and oceanic waves - a review. *Boundary-Layer Meteorology*, 13(61-85), 1978.
- [16] Valenzuela G. R. Depolarization of em waves by slightly rough surfaces, antennas and propagation. *IEEE Transactions on*, vol. AP-15, No. 4(.552-557), July. 1967.
- [17] S. Guignard R. Awadallah Elfouhaily T. M and D. R. Thompson. Local and non-local curvature approximation: a new asymptotic theory for wave scattering. *Waves in Random Media*, 13:4(321-337), 2003.
- [18] Mouche A.A. B.Chapron N.Reul. A simplified asymptotic theory for ocean surface electromagnetic wave scattering. *Waves in Random and Complex Media*, Vol. 17 (3)(pp.321-341), 2007.
- [19] Moore R.K. and A. K. Fung. Radar determination of winds at sea. *Proceedings of the IEEE*, VOL.67, NO.11, 1979.
- [20] Unal C. M. H. and P. J. F. Swart. The polarization-dependent relation between radar backscatter from the ocean surface and surface wind vector at frequencies between 1 and 18 ghz. *IEEE Geoscience and Remote Sensing*, VOL. 29, NO. 4, July 1991.
- [21] Quilfen Y. B.Chapron A.Bentamy J.Gourrion T.Elfouhaily and D.Vandemark. Global ers 1 and 2 and nscat observations: Upwind/crosswind and upwind/downwind measurements. *J. Geophys. Res.*, 104, C5(11,459-11,469), May 15, 1999.
- [22] Mouche A.A. D.Hauser J.F.Daloze and C.Guerin. Dual-polarization measurements at c-band over the ocean: results from airborne radar observations and comparison with envisat asar data. *Geoscience and Remote Sensing, IEEE Transactions on*, vol.43, No.4(pp. 753-769), April. 2005.
- [23] Kudryavtsev V. D.Hauser G.Caudal and B.Chapron. A semiempirical model of the normalized radar cross-section of the sea surface, 1, background model. *J Geophys. Res.*, 108(C3)(8054), 2003.

- [24] Thompson D.R. J.Horstmann A.Mouche N.S.Winstead R.Sterner and F.M.Monaldo. Comparison of high-resolution wind fields extracted from terrasar-x sar imagery with predictions from the wrf mesoscale model. *J. Geophys. Res.*, 117, C02035, February, 2012.
- [25] Rice S. O. Reflection of electromagnetic waves from slightly rough surfaces. *Comm. Pure Appl. Math*, 4, 351, 1950.
- [26] Wright J. W. A new model for sea clutter. *Antennas and Propagation, IEEE Transactions on*, .AP-16, No. 2(217-223), March 1968.
- [27] Plant W.J. A two-scale model of short wind-generated waves and scatterometry. *J. Geophys. Res.*, Vol 91, No C9(10,735-10,749), September 15, 1986.
- [28] Ulaby F.T R.K.Moore and A.K.Fung. *Microwave Remote Sensing: Radar Remote Sensing and Surface Scattering and Emission Theory, Volume II*. Artech House, INC., 1986.
- [29] Elfouhaily T. D. R. Thompson B. Chapron and D. Vandemark. A new bistatic model for electromagnetic scattering from perfect conducting random surfaces. *Waves Random Media*, 9(281-94), 1999.
- [30] Gambardella A. F. Nunziata and M. Migliaccio. A polarimetric sea surface backscattering model. *Proceeding of IGARSS2009*, 2009.
- [31] Ward K.D. C.J.Baker and S.Watts. Maritime surveillance radar part 1: Radar scattering from the ocean surface. *IEE Proceedings*, Vol.137, Pt. F. No.2(51-62), April 1990.
- [32] Goodman J. W. Some fundamental properties of speckle. *J. Opt. Soc. Am.*, Vol. 66, No. 11, November 1976.
- [33] Schmitt J.M. S.H.Xiang and K.M.Yung. Speckle in optical coherence tomography. *J. Biomed Opt*, 4(1)(95-105), 1999.
- [34] Wang L. V. Tutorial on photoacoustic microscopy and computed tomography. *IEEE Journal of Selected Topics in Quantum Electronics*, Vol. 14, NO. 1, January/February 2008.
- [35] Lopes A. R.Garello and S.L.Hegarar-Masclé. *Processing of synthetic aperture radar images*, chapter 5, Speckle models. ISTE Ltd, 2008.
- [36] Oliver C. and S. Quegan. *Understanding synthetic aperture radar images*. SciTech Publishing, Inc. USA, 2004.

- [37] Melief H.W. H.Greidanus P.V.Genderen and P.Hoogeboom. Analysis of sea spikes in radar sea clutter data. *IEEE trans. on Geos. and Remote sensing*, Vol. 44, No. 4, April 200.
- [38] Ward K.D. R.J.A.Tough and P.W.Shepherd. Sea spikes and radar false alarm rates. *3<sup>rd</sup> EMRS DTC Technical Conference, Edinburgh, 2006*.
- [39] Richards M.A. J.A.Scheer and W.A.Holm. *Principles of modern radar*. SciTech Publishing, Inc., 2010.
- [40] Jessup A. T. Measurements of sea spikes in microwave backscatter at moderate incidence. *Journal of Geophysical Res.*, Vol. 95, No. C6(P9679-9688), 15 June 1990.
- [41] Alpers W. D. B. Ross and C. L. Rufenach. On the detectability of ocean surface waves by real and synthetic aperture radar. *J. Geophys. Res.*, Vol. 86, NO. C7(p.6481-6498), July 20, 1981.
- [42] Ward K.D. R.J.A.Tough and S.Watts. *Sea clutter: scattering, the K distribution and radar performance*. The Institution of Engineering and Technology, London, UK, 2006.
- [43] Yueh S.H. and J.A.Kong. K-distribution and terrain radar clutter. *J.Electro. Waves and Appl.*, 3no.8(747-768), 1989.
- [44] Novak L. M. and S. R. Hesse. Optimal polarizations for radar detection and recognition of targets in clutter. *Radar Conference, 1993., Record of the 1993 IEEE National, Lynnfield, MA, USA , USA*, 1993.
- [45] Hasselmann K. and S. Hasselmann. On the nonlinear mapping of an ocean wave spectrum into a synthetic aperture radar image spectrum and its inversion. *J. Geophysical Research*, VOL. 96, No. C6(P.10713-10729), June 15,1991.
- [46] Robinson I. S. *Measuring the oceans from space*. Praxis Publishing Ltd, Chichester, UK, 2004.
- [47] Ericson E. A. D. R. Lyzenga and D. T. Walker. Radar backscatter from stationary breaking waves. *J Geophys. Res.*, Vol.104(C12)(P.29,679-29,695), December 15, 1999.
- [48] Zyl J.J. H.A.Zebker and C.Elachi. Imaging radar polarization signatures: Theory and observation. *Radio Science*, Vol 22 (4)(529-543), July-August 1987.
- [49] Zebker H.A. J.J.Zyl and D.N.Held. Imaging radar polarimetry from wave synthesis. *Journal of Geophysical Research*, Vol. 92, No. B1(683-701), January, 10, 1987.

- [50] Nasr J. M. Application of a sar image simulator to the study of the polarization signature of man-made targets. *Quantitative remote sensing: An economic tool for the Nineties; Proceedings of IGARSS '89 and Canadian Symposium on Remote Sensing, 12th, Vancouver, Canada, July 10-14, 1989.*, Volume 1 (A91-15476 04-43)(p. 25-28.), 1989.
- [51] Hajnsek I. K.Papathanassiou.  $\hat{\alpha}$ , chapter 2,Rough surface scattering models.  $\hat{\alpha}$ , 2005.
- [52] Cameron W. L. and L. K. Leung. Feature motivated polarization scattering matrix decomposition. *IEEE International Radar Conference*, (PP.549-558), 1990.
- [53] Jeremy M. J.W.M.Campbell K.Matter and T.Potter. Ocean surveillance with polarimetric sar. *Canadian Journal of Remote Sensing*, Vol. 27, No. 4, August 2001.
- [54] Crisp D. J. The state-of-art in ship detection in synthetic aperture radar imagery. *DSTO Information Sciences Laboratory*, DSTO-RR-0272, 2004.
- [55] Touzi R. and F. Charbonneau. The sscm: An adaptation of cameron's target decomposition to actual calibration sar requirements. *Proc. of CEOS Working Group on Calibration/Validation SAR Workshop, London, United Kindom,24-26 September 2002*, ESA SP-536, March 2003.
- [56] Garelo R. S. Proust and B. Chapron. 2d ocean surface sar images simulation: a statistical approach. *Proc. OCEANS'93*, vol. 3(p.7-12), 1993.
- [57] Choong P. L. Modelling airborne l-band radar sea and coastal land clutter. Technical report, DSTO, 2000.
- [58] Chen H. M. Zhang Y. W. Zhao and W. Luo. An efficient slope-deterministic facet model for sar imagery simulation of marine scene. *IEEE Trans. on Antennas and Propagation.*, 2010.
- [59] Clarizia M. P. C. Gommenginger M. D. Bisceglie C. Galdi and M. A. Srokosz. Simulation of l-band bistatic returns from the ocean surface: A facet approach with application to ocean gnss reflectometry. *IEEE Trans. on Geos. and Remote Sens.*, 2012.
- [60] Ringrose R. and N. Harris. Ship detection using polarimetric sar data. *Proceedings of the CEOS SAR workshop, Toulouse, 26-29 October 1999*, ESA SP-450, March 2000.
- [61] Touzi R. F.Charbonneau R.K.Hawkins and P.W.Vachon. Ship detection and characterization using polarimetric sar. *Canadian Journal of Remote Sensing*, Vol. 3, No. 3(552-559), 2004.
- [62] J. J. van Zyl. *On the importance of polarization in radar scattering problems*. PhD thesis, California Institute of Technology, Pasadena, California, 1985.

- [63] D. S. W. Kwoh and B. M. Lake. A deterministic, coherent, and dual-polarized laboratory study of microwave backscattering from water waves, part i: short gravity waves without wind. *Journal of Oceanic Engineering*, OE-9(5):291–308, 1984.
- [64] Frost V.S. Probability of error and radiometric resolution for target discrimination in radar images. *IEEE Transactions on Geoscience and Remote Sensing*, VOL. GE-22, NO. 2, March 1984.
- [65] Curlander J. C. and R. N. McDonough. *Synthetic aperture radar - system and signal processing*. ISBN 0-471-85770-X, Wiley series in remote sensing, 1991.
- [66] Franceschetti G. and R. Lanari. *Synthetic aperture RADAR processing*. CRC Press, Boca Raton, Fla. ISBN 0-8493-7899-0.
- [67] Chapron B. H. Johnsen and R. Garello. Wave and wind retrieval from sar images of the ocean. *ANNALS OF TELECOMMUNICATIONS*, Volume 56, Numbers 11-12(682-699), 2001.
- [68] He Y.J. H. Shen and W. Perrie. Remote sensing of ocean waves by polarimetric sar. *J. Atmospheric and Oceanic Technology*, Vol.23(P.1768-1773), December 2006.
- [69] Jeffreys H. On the formation of water waves by wind. *Proc. R. Soc. Lond. A*, 107(189-206), February 2, 1925.
- [70] Jeffreys H. On the formation of water waves by wind (second paper). *Proc. R. Soc. Lond. A*, 110(241-247), 1926.
- [71] Hasselmann K. Barnett T.P. Bouws E. Carlson H. Cartwright D.E. Enke K. Ewing J.A. Gienapp H. Hasselmann D.E. Kruseman P. Meerburg A. Müller P. Olbers D.J. Richter K. Sell W. Walden H. *Measurements of wind-wave growth and swell decay during the Joint North Sea Wave Project (JONSWAP)*. Deutsches Hydrographisches Institut, 1973-01-01.
- [72] The WAMDI group. The wam model - a third generation ocean wave prediction model. *Journal of Physical Oceanography*, December 1988.
- [73] Elfouhaily T. B. Chapron K. Katsaros and D. Vandemark. A unified directional spectrum for long and short wind-driven waves. *J Geophys. Res.*, Vol.102(C7)(P.15781-15796), July 15, 1997.
- [74] Chen G. and S. E. Belcher. Effects of long waves on wind-generated waves. *Journal of Physical Oceanography*, Vol.30, September 2000.
- [75] Plant W.J. Bound waves and sea-surface slope. *Proceedings of OCEANS2003.San Diego, CA, USA*, Vol.4(1825-1828), 22-26 Sept. 2003.

- [76] Ardhuin F. T. H. C. Herbers G. P. Vledder K. P. Watts R. Jensen and H. C. Graber. Swell and slanting-fetch effects on wind wave growth. *Journal of Physical Oceanography*, Vol.37(pp.908-931), April 2007.
- [77] Cox C. Measurements of slopes of high frequency waves. *J. Mar. Res.*, 16(199-225), 1958.
- [78] Schuler D. L. and J. S. Lee. A microwave technique to improve the measurement of directional ocean wave spectra. *Int. J. Remote Sensing*, Vol. 16, No. 2(199-215), 1995.
- [79] Schuler D.L. J.S.Lee D.Kasilingam E.Pottier. Measurement of ocean surface slopes and wave spectra using polarimetric sar image data. *Remote Sensing of Environment*, 91(198 - 211), 2004.
- [80] Lee J.S. D.L.Schuler T.L.Ainsworth E.Krogager D.Kasilingam W.M.Boerner. On the estimation of radar polarization orientation shift induced by terrain slopes. *Geoscience and Remote Sensing, IEEE Transactions on*, vol.40, No. 1(pp. 30-41), January 2002.
- [81] Lee J.S. D.L.Schuler and T.L.Ainsworth. Polarimetric sar data compensation for terrain azimuth slope variation. *Geoscience and Remote Sensing, IEEE Transactions on*, vol.38, No. 5(pp. 2153-2163), September 2000.
- [82] He Y.J. B.Zhang and W. Perrie. Validation of radarsat-2 polarimetric sar measurements of ocean waves. *Proceedings of IGARSS 2009*, (pp. III-168-171), 2009.
- [83] Pottier E. Unsupervised classification scheme and topography derivation of polsar data on the  $h/a/\alpha$  polarimetric decomposition theorem. *Proc. of the 4th International Workshop on Radar Polarimetry, Nantes, France: IRESTE. 1998*, (pp.535-548), 1998.
- [84] R. Jansen D. Schuler T. Ainsworth G. Marmorino Lee, J. S. and S. Chubb. Polarimetric analysis and modeling of multifrequency sar signatures from gulf stream fronts. *IEEE Journal of Oceanic Engineering*, 23(322-332), 1998.
- [85] Schuler D.L. J.S.Lee and G.D.Grandi. Measurement of topography using polarimetric sar images. *IEEE Trans. on geoscience and remote sensing*, VOL. 34, NO. 5(1266-1277), 1996.
- [86] Alpers W. Monte carlo simulations for studying the relationship between ocean wave and synthetic aperture radar image spectra. *J. Geophys. Res.*, Vol. 88, NO. C3(p.1745-1759), February 28, 1983.
- [87] Zhang B. W.Perrie and Y.He. Wind speed retrieval from radarsat-2 quad-polarization images using a new polarization ratio model. *J. Geophys. Res.*, 116, C08008, 2011.

- [88] Plant W.J. W.C.Keller K.Hayes and G.Chatham. Normalized radar cross section of the sea for backscatter: 1. mean levels. *J. Geophys. Res.*, 115, C09032, 2010.
- [89] Nicolas J. M. and S. L. Hegarat-Mascle. *Processing of synthetic aperture radar images*, chapter 1, The physical basis of synthetic aperture radar imagery. ISTE Ltd, 2008.
- [90] Kerbaol V. B.Chapron and P.W.Vachon. Analysis of ers-1/2 synthetic aperture radar wave mode imagettes. *J Geophys. Res.*, 103(C4)(pp.7833-7846), 1998.
- [91] Chapron B. F. Collard and F. Arduin. Direct measurements of ocean surface velocity from space: Interpretation and validation. *Journal of Geophysical Research*, Vol. 110, C07008, 2005.
- [92] Goldstein R.M. and H. A. Zebker. Interferometric radar measurement of ocean surface currents. *Nature*, Vol. 328(P707-709), 20 August 1987.
- [93] Romeiser R. and D. R. Thompson. Numerical study on the along-track interferometric radar imaging mechanism of oceanic surface currents. *IEEE Trans. on Geoscience and Remote Sensing*, Vol. 38, No.1, January 2000.
- [94] Thompson A.A. and I.H.McLeod. The radarsat-2 sar processor. *Can. J. Remote Sensing*, Vol. 30, No.3(336-344), 2004.
- [95] Hansen M.W. F.Collard K.F.Dagestad J.A.Johannessen P.Fabry and B.Chapron. Retrieval of sea surface range velocities from envisat asar doppler centroid measurements. *IEEE trans. on Geos. and Remote Sens.*, Vol. 49, No. 10, October 2011.
- [96] Mouche A.A. F.Collard B.Chapron K.F.Dagestad G.Guitton J.A.Johannessen V.Kerbaol and M.W.Hansen. On the use of doppler shift for sea surface wind retrieval from sar. *IEEE trans. on Geos. and Remote sensing*, Vol. 50, No. 7, July 2012.
- [97] Madsen S. N. Estimating the doppler centroid of sar data. *IEEE Transactions on Aerospace and Electronic Systems*, VOL.AES-25, NO. 2, MARCH 1989.
- [98] Cafforio C. P. Guccione and A. M. Guarnieri. Doppler centroid estimation for scansar data. *IEEE Trans. on geoscience and remote sensing*, VOL. 42, NO. 1(pp.14-23), Jan.2004.
- [99] Slade B. *RADARSAT-2 product description*. RN-SP-52- 1238, Issue 1/6, Nov.2 2009.
- [100] Bamler R. and H. Runge. Prf-ambiguity resolving by wavelength diversity. *IEEE Trans. on geoscience and remote sensing*, VOL. 29, NO. 6(pp.997-1003), Nov.1991.

- [101] Korsbakken E. J.A.Johannessen and O.M.Johannessen. Coastal wind field retrievals from ers synthetic aperture radar images. *J. Geo. Res.*, Vol. 103, No. C4(P.7857-7874), April, 1998.
- [102] Kerbaol V. *Analyse spectrale et statistique vent-vagues des images radar à ouverture synthétique*. PhD thesis, Université de Rennes 1, Rennes, France, 1997.
- [103] Welander P. On the generation of wind streaks on the sea surface by action of surface film. *Tellus XV*, 1(67-71), 1963.
- [104] LeMone M. A. The structure and dynamics of horizontal roll vortices in the planetary boundary layer. *Journal of the Atmospheric Sciences*, Vol. 30(P.1077-1091), September 1973.
- [105] Gerling T. W. Structure of the surface wind field from the seasat sar. *J. Geo. Res.*, Vol. 91, No. C2(P.2308-2320), February 1986.
- [106] Levy G. Boundary layer roll statistics from sar. *Geo. Res. Letters*, Vol. 28, No. 10(P.1993-1995), May 2001.
- [107] Portabella M. A.Stoffelen and J.A.Johannessen. Toward an optimal inversion method for synthetic aperture radar wind retrieval. *J. Geo. Res.*, Vol. 107, No. C8, 2002.
- [108] Wackerman C.C. C.L.Rufenach R.A.Shuchman J.A.Johannessen and K.L.Davidson. Wind vector retrieval using ers-1 synthetic aperture radar imagery. *IEEE Trans. on Geos. and Remote Sensing*, Vol. 34, No. 6, November 1996.
- [109] Fetterer F. D. Gineris and C. C. Wackerman. Validating a scatterometer wind algorithm for ers-1 sar. *IEEE Transactions on Geoscience and Remote Sensing*, VOL. 36, NO. 2, March 1998.
- [110] Liu W. T. and W. Q. Tang. *Spaceborne scatterometer in studies of atemospheric and oceanic phenomena from synoptic to interannual time scales*. NASA technical reports, September 12, 1995.
- [111] Lee J.S. M.R.Grunes G.Grandi. Polarimetric sar speckle filtering and its implication for classification. *IEEE Trans. on geoscience and remote sensing*, VOL. 37, NO. 5(pp.2363-2373), 1999.
- [112] Lee J.S. K.W.Hoppel S.A.Mango and A.R.Miller. Intensity and phase statistics of multilook polarimetric and interferometric sar imagery. *IEEE Trans. on geoscience and remote sensing*, VOL. 32, NO. 5(pp.1017-1028), September 1994.

- [113] Xiao Y.X. H.L.Peng and S.W.Shu. Research on synthetic aperture radar (sar) imaging system with information theory. *ACTA Electronic Sinica*, 24, April, 1996.
- [114] Ward K. D. Compound representation of high resolution sea clutter. *Electronics Letters*, Vol.17, No. 16, August 1981.
- [115] Moser G. J.Zerubia and S.B.Serpico. Sar amplitude probability density function estimation based on a generalized gaussian model. *IEEE Trans. on Image Processing*, Vol. 15, No. 6, June 2006.
- [116] Anfinsen S. N. *Statistical analysis of multilook polarimetric radar images with the Mellin transform*. Ph.D. dissertation of University of Tromso, May 2010.
- [117] Gao G. Statistical modeling of sar images: A survey. *Sensors*, 10(775-795), 2010.
- [118] Goodman N. R. Statistical analysis based on a certain multivariate complex gaussian distribution (an introduction). *Complex multivariate analysis, The Annals of Mathematical Statistics*, (P.152-177), 1962.
- [119] Goodman J. W. *Laser speckle and related phenomena*, chapter 2, Statistical properties of laser speckle patterns. Springer-Verlag Berlin Heidelberg, 1975.
- [120] Johnson N.L. S.Kotz and N.Balakrishnan. *Continuous univariate distributions, Volume1, 2nd Edition*. John Wiley Sons, Inc., October 1994.
- [121] Trunk G. V. Radar properties of non-rayleigh sea clutter. *IEEE Trans.*, AES-8(196-204), 1972.
- [122] Skolnik M. *Radar Handbook*,, 2nd. 1990.
- [123] Antipov I. *Analysis of sea clutter data*. DSTO Electronic and Surveillance Research Laboratory, March 1998.
- [124] Valenzuela G. R. and M. B. Laing. *On the statistics of sea clutter*. Naval Research Lab., Rept. 7349, 1971.
- [125] Jakeman E. and P. N. Pusey. A model for non-rayleigh sea echo. *IEEE Transactions on Antennas and Propagation*, Vol. AP-24, No. 6, November 1976.
- [126] Barakat R. Weak-scatter generalization of the k-density function with application to laser scattering in atmospheric turbulence. *J. Opt. Soc. Am. A*, Vol. 3, No. 4(pp. 401-409), April 1986.
- [127] Jakeman E. and R. J. A. Tough. Generalized k distribution a statistical model for weak scattering. *J. Opt. Soc. Am. A*, Vol. 4, No. 9(pp.1764-1772), September 1987.

- [128] Migliaccio M. G.Ferrara A.Gambardella F.Nunziata and A.Sorrentino. A physically consistent speckle model for marine slc sar images. *IEEE J. Ocean Eng.*, Vol. 32, No. 4(pp.839-847), Oct. 2007.
- [129] Ferrara G. M. Migliaccio F. Nunziata and A. Sorrentino. Generalized-k-based observation of metallic objects at sea in full-resolution synthetic aperture radar data: A multipolarization study. *IEEE Journal of Oceanic Engineering*, Vol. 36, No. 2, April 2011.
- [130] Rice S. O. *Mathematical analysis of random noise*. Bell telephone labs INC, New York, 1952.
- [131] Tepedelenlioglu C. A.Abdi and G.B.Giannakis. The rician k factor: estimation and performance analysis. *IEEE Trans. on Wireless Communications*, Vol. 2, No. 4, July 2003.
- [132] Fried D. L. Statistics of the laser radar cross section of a randomly rough target. *J. Opt. Soc. Am.*, Vol. 66, No. 11, November 1976.
- [133] Richards M. A. *Rice distribution for RCS*. Georgia Institute of Technology, Sep. 2006, updated 2010.
- [134] Jakeman E. On the statistics of k-distributed noise. *J. Phys. A: Math. Gen.*, 13(31-48), 1980.
- [135] Eltoft T. *A new approach to modeling signal amplitude statistics by the K distributions*. NORSIG, 2006.
- [136] McDonald D. M. Speckle reduction in synthetic aperture radar images. May,1988.
- [137] Moreira A. An improved multi-look technique to produce sar imagery. *Radar Conference, 7-10 May 1990., Record of the IEEE 1990 International*, 1990.
- [138] Li F. Comparison of several techniques to obtain multiple-look sar imagery. 1983.
- [139] Fujii H. and T. Asakura. Effect of surface roughness on the statistical distribution of image speckle intensity. *Optics communications*, Vol. 11, No. 1(pp.35-38), May 1974.
- [140] Berny F. and C. Imbert. *Détermination optique des états de surface*. Bulletin du BNM, 11, 1973.
- [141] Esch T. M. Thiel A. Schenk A. Roth A. Muller and S. Dech. Delineation of urban footprints from terrasars-x data by analyzing speckle characteristics and intensity information. *Geoscience and Remote Sensing, IEEE Transactions on*, vol.48(pp. 905-916), Feb. 2010.

- [142] Pearson K. On the criterion that a given system of deviations from the probable in the case of a correlated system of variables is such that it can be reasonably supposed to have arisen from random sampling. *Philosophical Magazine Series 5*, Vol. 50, Iss. 302, 1900.
- [143] Chan H. C. Radar sea clutter at low grazing angles. *Radar and Signal Processing, IEE Proceedings F.*, vol.137(pp. 102-112), Apr.1990.
- [144] Xing X.W. Z.L.Chen H.X.Zou and S.L.Zhou. A fast algorithm based on two-stage cfar for detection ships in sar images. *Synthetic Aperture Radar 2009. APSAR 2009. 2nd Asian-Pacific Conference on, Xian, Shanxi*, (26-30), Oct. 2009.
- [145] Wang B. B.Chapron G.Mercier R.Garello and M.X.He. Polarimetric characteristics of ships on radarsat-2 data. In *OCEANS2011, 6-9 June 2011 Santander, Spain*.
- [146] Eltoft T. The rician inverse gaussian distribution: A new model for non-rayleigh signal amplitude statistics. *IEEE Trans. on Image Processing*, Vol. 14, No. 11, November 2005.
- [147] Martínez A. and J. L. Marchand. Sar image quality assessment. *Revista de Teledeteccion*, No. 2, November, 1993.
- [148] Freitas C.C. A.C.Frery A.H. Correia. The polarimetric g distribution for sar data analysis. 2003.
- [149] Tur M. K.C.Chin and J.W.Goodman. When is speckle noise multiplicative. *Applied Optics*, Vol. 21, NO. 7, 1982.
- [150] Chaabouni H. and M. Datcu. Relevant scatterers characterization in sar images. *AIP Conf. Proc. 872, Paris, France*, (pp. 375-382), 8-13 July 2006.
- [151] Meisl P. A.A.Thompson and A.P.Luscombe. Radarsat-2 mission: overview and development status. *proceedings of EUSAR 2000, Munich, Germany*, (pp.23-25), May 2000.
- [152] Anfinson S.N. A.P.Doulgeris T. Eltoft. Estimation of the equivalent number of looks in polarimetric synthetic aperture radar imagery. *IEEE Trans. on geoscience and remote sensing*, VOL. 47, NO. 11(pp.3795-3809), 2009.
- [153] DeVore M. D. *Recognition performance from synthetic aperture radar imagery subject to system resource constraints*. dissertation, Washington university, 2001.
- [154] Munk W.H. P.Scully-Power and F.Zachariassen. The bakerian lecture, 1986, ships from space. *Proceedings of the Royal Society of London. Series A, Mathematical and Physical Sciences*, Vol. 412, No. 1843(pp.231-254), Aug. 8, 1987.
- [155] Dudgeon D. E. and R. T. Lacoss. An overview of automatic target recognition. *The Lincoln Laboratory Journal*, Vol. 6, NO. 1(pp.3-10), 1993.

- [156] Cloude S. R. Eigenvalue parameters for surface roughness studies. *Proc. SPIE Conference on Polarization: Measurements, Analysis, and Remote Sensing II*, vol 37(pp.243-254), Denver, CO.,1999.
- [157] Xu F. and Y. Q. Jin. Deorientation theory of polarimetric scattering targets and application to terrain surface classification. *Geoscience and Remote Sensing, IEEE Transactions on*, 43(2351-2364), 2005.
- [158] Dilsavor R. L. and R. L. Moses. Fully-polarimetric glrts for detecting scattering centers with unknown amplitude, phase, and tilt angle in terrain clutter. *presented at SPIE's International Symposium on Optical Engineering in Aerospace Sensing, Orlando, FL*, April 4-8, 1994.
- [159] Freeman A. and S. L. Durden. A three-component scattering model for polarimetric sar data. *IEEE Trans. Geosi. Remote Sensing*, Vol.36, No.3(pp.963-973), May 1998.
- [160] Han Z.Y. and J.S.Chong. A review of ship detection algorithms in polarimetric sar images. *Signal Processing, 2004. Proceedings. ICSP '04. 2004 7th International Conference on*, Vol. 3(pp2155-2158), 2004.
- [161] Daniel E. K. S. D. Halversen and G. J. Owirka. Discriminating targets from clutter. *The Lincoln Laboratory Journal*, Vol. 6, NO. 1(pp.25-52), 1993.
- [162] Touzi R. F.Charbonneau R.K.Hawkins K.Murnaghan and X.Kavoun. Ship-sea contrast optimization when using polarimetric sars. *Geoscience and Remote Sensing Symposium, 2001. IGARSS '01. IEEE 2001 International*, 2001.
- [163] Sciotti M. D.Pastina and P.Lombardo. Polarimetric detectors of extended targets for ship detection in sar images. *IEEE IGARSS'01*, 7(3132-3134), 2001.
- [164] Sciotti M. D.Pastina and P.Lombardo. Exploiting the polarimetric information for the detection of ship targets in non-homogeneous sar images. *IEEE IGARSS'02*, Vol. 3(.1911-1913), 2002.
- [165] Novak L.M. M.B.Seciitin and M.J.Cardullo. Studies of target detection algorithms that use polarimetric radar data. *IEEE Trans. Aerospace and Electronic systems*, Vol. AES-25, No. 2, March 1989.
- [166] Novak L. M. and M. C. Burl. Optimal speckle reduction in polarimetric sar imagery. *IEEE Trans. Aerospace and Electronic systems*, Vol. 26, No. 2, March 1990.
- [167] VanTrees H. L. *Detection, estimation, and modulation theory, Part 1: Detection, estimation, and linear modulation theory*. John Wiley Sons, Inc., 2001.

- [168] Potter L. C. and R. L. Moses. Attributed scattering centers for sar atr. *IEEE trans. on Image Processing*, Vol. 6, No. 1, January 1997.
- [169] Xu L. Z. and J. Li. Iterative generalized-likelihood ratio test for mimo radar. *IEEE Trans. on Signal processing*, Vol. 55, No. 6, June 2007.
- [170] Bandiera F. and G. Ricci. Slicks detection on the sea surface based upon polarimetric sar data. *IEEE Geos. and Remote sensing Letters*, Vol. 2, No. 3, July 2005.
- [171] De Maio A. S. De Nicola and A. Farina. Glrt versus mflrt for adaptive cfar radar detection with conic uncertainty. *IEEE Signal Processing Letters*, Vol. 16, No. 8, August 2009.
- [172] Ocean and Sea Ice SAF. *ASCAT wind product user manual*. SAF/OSI/CDOP/KNMI/TEC/MA/126, V1.10, August 2011.
- [173] Phillips O. M. *The dynamics of the upper ocean*. Cambridge at the university press, 1966.
- [174] Du Y. P. W. Vachon and J. Wolfe. Wind direction estimation from sar images of the ocean using wavelet analysis. *Canadian Journal of Remote Sensing*, 2002, 28:(3)(498-509), 10.5589/m02-029.
- [175] Tunaley J.K.E. Sar velocity bunching relationships.
- [176] Blahut R. E. *Theory of remote image formation*. University Press, Cambridge, 2004.
- [177] Solaas G. and H. Laur. *An assessment of ERS SAR low resolution imagery*. ES-TN-DPE-OM-GS01, version 1., 1 July 1993.
- [178] <http://www.tscm.com/reference.html>.